Cover Page of Final Report

Project Information

Project Title: Laser 3D printing of highly compacted protonic ceramic electrolyzer stack

Project Period of Performance: October 1st, 2018 – April 30, 2022

Date of Report Submission: 11/05/2022

Recipient: Clemson University

Technical Contact: Joshua Tong, jianhut@clemson.edu

Business Contact: Melanie Trotter, mtrott@clemson.edu

DOE Managers: Brian Hunter, 240-562-1347, brian.hunter@ee.doe.gov

Acknowledgment

This material is based upon work supported by the U.S. Department of Energy's Office of Energy Efficiency and Renewable Energy (EERE) under the Hydrogen and Fuel Cell Technologies Office, Award Number DE-EE0008428.

Disclaimer

Table of Contents

Project Background

Solid oxide electrolysis cells (SOECs) for H_2 production is a core technology for H2@scale. However, its conventional manufacturing methods adapted from the manufacture of solid oxide fuel cells (SOFC) need high cost, especially for small-volume production. The emerging laser 3D printing (L3DP) technology with computer-aided 3D printing and computer-controlled laser processing can fulfill layer-by-layer digital shaping and rapid in-situ consolidating feedstock into complicated geometries. L3DP, a promising additive manufacturing (AM) technology, has achieved significant success in manufacturing plastic and metal parts, which is currently attracting considerable attention for the cost-effective, rapid, and flexible manufacturing of heterogeneous multilayered ceramic devices (e.g., SOECs, SOFCs, and solid-state batteries). It is believed that the L3DP can integrate the advantages of selective consolidation of heterogeneous layers, accurate control of layer microstructures, high processing heat efficiency, high processing speed, high stack compactness, high stack design flexibility, and low stack sealing area for cost-effective, rapid, and flexible manufacturing of SOECs to meet DOE's electrolyzer target.

Project Objective

The project has four main objectives: **1)** Develop high-performance intermediate temperature protonic ceramic electrolyzer stack (IT-PCES) component materials, printable component pastes, and rapid laser reactive sintering (RLRS) technology. **2)** Manufacture large-area, high-performance, and stable IT-PCESs with L3DP technology. **3)** Do initial TEA for H_2 production in IT-PCES and show a significant cost decrease compared to state-of-the-art electrolyzers at the same production scale. **4)** Demonstrate the commercial viability of IT-PCES manufactured by L3DP technology by boosting the TRL to >4.

We propose the following **5** tasks. **Task 1:** The PCES component materials of electrolyte, H_2, and O_2 electrodes and interconnect with high performance and excellent compatibility will be discovered. **Task 2:** The precursor pastes compositions, 3D printing parameters, and RLRS conditions will be achieved for manufacturing crack-free component layers with controlled thickness, configuration, and microstructure. **Task 3:** The challenges of bonding between component layers and infiltration in porous electrode scaffolds will be solved. The PCES single cells will be manufactured by L3DP and tested. **Task 4:** Laser machining technology will be optimized for in-situ machining microchannels in interconnects. The PCES with multiple cells will be manufactured by L3DP technology and tested. **Task 5:** The H_2 production cost will be analytically estimated based on the main manufacturing cost, including materials, L3DP, infiltration and the performance of the PCES.

1. Recipient's Achievements Towards Meeting the Objectives

1.1 Significant Findings, Conclusions, and Developments

1) The new protonic ceramic electrolyte of $BaCe_{0.7}Zr_{0.1}Y_{0.07}Sm_{0.13}O_{3-\delta}$ (BCZYSm13) showed a proton conductivity as high as 9×10^{-3} Ω/cm at 600 °C. The calculation according to the electrolyte membrane thickness of ~9 μm, which could be easily achieved by either solid-state reactive sintering (SSRS) or RLRS, indicated that the area-specific resistance (ASR) for this electrolyte reached 0.1 $\Omega\cdot cm^2$ at 600 °C.

2) The total polarization for the hydrogen electrode of 40wt% BCZYSm13 + 60wt%NiO and the oxygen electrode $BaCe_{0.6}Zr_{0.3}Y_{0.1}O_{3-\delta}$ (BCZY63) + $BaCo_{0.4}Fe_{0.4}Zr_{0.1}Y_{0.1}O_{3-\delta}$ (BCFZY0.1) showed a value of 0.2 $\Omega\cdot cm^2$ at 600 °C.

3) The thin-film BCFZY0.1 oxygen electrode prepared through a new intermediate precursor showed an ASR of 0.053 $\Omega\cdot cm^2$ at 600 °C, which was much better than the state-of-the-art oxygen electrode performance.

4) The interconnect material of $La_{0.7}Sr_{0.3}CrO_{3-\delta}$ (LSCr) was discovered to be compatible with the model PCES component material of $BaCe_{0.7}Zr_{0.1}Y_{0.1}Yb_{0.1}O_{3-\delta}$ (BCZYYb) electrolyte, 40wt%BCZYYb+60wt%NiO hydrogen electrode, BCFZY0.1 oxygen electrode, and BCZY63 oxygen electrode scaffold at 700°C. The electronic conductivity of 16.2 S/cm was obtained at 600 °C, which allowed much lower ASR to work as a thin-film type interconnect.

5) A single cell of 40wt% BCZYSm13 +60wt% NiO | BCZYSm13 | BCZY63 + BCFZY0.1 with an active area ~0.5cm^2 was successfully prepared by the SSRS method, which showed the current densities of 1375 mA/cm^2 and 785 mA/cm^2 at 650 °C and 600 °C when operating in the electrolysis mode with an applied voltage of 1.3V.

6) A single cell of 40wt% BCZYSm13 + 60wt% NiO | BCZYSm13 | BCZY63 + BCFZY0.1 with different layer thicknesses was also successfully prepared by SSRS method, which showed a current density of 1050 mA/cm^2 at 600 °C when operating in the electrolysis mode with an applied voltage of 1.3V.

7) A single cell of 40wt% BCZYYb +60wt% NiO | BCZYSm13 | BCFZY0.1 with an active area ~0.5 cm^2 prepared by the SSRS method showed a current density of 640 mA/cm^2 at 620 °C when operating in the electrolysis mode with an applied voltage of 1.3V. The stability test showed that, instead of degradation, the cell showed a steadily increased current density with the tested time of ~110 hrs.

8) A single cell of 40wt% BCZYYb + 60wt% NiO | anode functional layer (AFL) | BCZYYb + 1wt%NiO | BCZYYb + BCFZY0.1 was fabricated by tape casting method, demonstrating stable electrolysis at 600 °C for more than 1000 h with a constant current density of 1.05 A/cm^2 while applying a voltage of 1.3 V.

9) The recipe for achieving printable pastes for versatile protonic ceramic-based materials systems was developed, which allowed us to 3D print crack-free green films of BCZYYb+1wt%NiO electrolyte, 40wt% BCZYYb+60wt%NiO hydrogen electrode, BCFZY0.1 oxygen electrode, and LSrCr interconnect precursor layers with an area larger than 10cm×10cm and thickness 150-1000 μm. The new technique of microextrusion followed by Dr. Blade paving allowed to decrease green film's thickness to around 50 μm. The new spray coating-based technique allowed to decrease the film thickness further to less than 30μm.

10) Clemson invented the rapid laser reactive sintering (RLRS) method, and the patent has been filed, which could fabricate electrolyte, electrode, and membranes with the desired crystal structure and microstructures. Another patent focusing the direct L3DP of PCFCs was disclosed and the filing of patent is under reviewing by Clemson University Research Foundation.

11) The fully densified BCZYYb+1wt%NiO electrolyte films with controllable thickness were prepared by the RLRS method either in the half cell and single-cell configurations. The defect-free electrolyte films can be as thin as 9 μm. The crack-free electrolyte film on the porous hydrogen electrode with a unit area greater than 6cm^2 can be prepared by RLRS with high reproductivity. A summary of ~120 cm^2 crack free and full density obtained. The ASR of the electrolyte membrane measured in the single-cell configuration under open-circuit conditions can reach a value of ~0.08 $\Omega \cdot cm^2$.

12) The porous hydrogen electrodes with a unit active area of >6 cm^2 (summary area >120 cm^2) and desired crystal structure and microstructure were obtained RLRS. The hydrogen electrodes prepared by RLRS in several single cells showed ASR values around 0.0744 $\Omega \cdot cm^2$ at 600 ^oC.

13) The porous oxygen electrode scaffold of BCZY63 with a unit area around 6 cm^2 was successfully prepared by RLRS in the single-cell configuration by sintering the three layers (electrolyte, hydrogen electrode, and oxygen electrode cathode) through one laser scan. The oxygen electrode scaffold of BCZY63 after infiltrating with BCFZY0.1 showed excellent polarization resistance performance. The ASR of 0.1 $\Omega \cdot cm^2$ was achieved at 600 ^oC.

14) The fully densified phase-pure LSCr interconnect film with thickness as thin as 10 μm and active area as large as 7 cm^2 was successfully prepared by RLRS on fused silica or MgO substrate. The ASR measurement showed a value of around 0.001 $\Omega \cdot cm^2$ at 600 °C.

15) The spiral laser scanning using the Galvo scanner could do RLRS of the curling-free homogenous large-area layers. The SEM results indicated that the desirable microstructures could be achieved for hydrogen electrode-supported half-cells, which could break the width limitation of laser scanning through the cylindrical lens. Furthermore, the Galvo scanner allowed much faster RLRS than that using the moving of the 3D printing stage.

16) The rapid laser sintering of the patterned 40wt%BCZYYb + 60wt%NiO/BCZYYb half cells resulted in a crack-free laser-sintered film due to the pre-machined micro troughs, which would provide another way to make crack-free PCES component films or cells followed by welding the small pattern units.

17) A single cell (0.3cm^2) with a half cell fabricated by L3DP showed an improved peak power density of 1046 mW/cm^2 at 600 ^oC under the Air/H_2 gradient in fuel cell operation mode, which was among the highest power density for the PCFCs fabricated by time-consuming and the complex conventional furnace-firing method.

18) A single cell (0.2 cm^2) with a half cell fabricated by L3DP showed current densities as high as 1.36 A/cm^2 and 2.26 A/cm^2 at 600 ^oC and 650 ^oC while operating in an electrolysis mode at 1.3V. During the long-term operation of 163 h, the current density increased from 1.161 A/cm^2 to 1.794 A/cm^2 instead of degradation.

19) The larger area single cells (active cell area is about 1.35 cm^2) with half cells fabricated by L3DP showed the current density of 530 mA/cm^2 was obtained at 600 ^oC.

20) The single cells were manufactured by one-step RLRS successfully, which showed an active area ~6 cm^2.

21) The larger-area single cells (the active area is ~0.9 cm^2) manufactured by one-step RLRS showed a current of ~623 mA/cm^2 at 600^oC under 1.3V was obtained while operating in the electrolysis mode, which is higher than our milestone of 500mA/cm^2 at 600^oC. The long-term test is undergoing, which showed the improvement of current density from 403 mA/cm^2 to 623 mA/cm^2 within 19 hrs instead of degradation.

22) The half cells with the active area ~6 cm^2 manufactured by RLRS can survive the second laser scan at the same power density, which provides a strong baseline for making PCEC stack with multiple one laser scanning.

23) The quick back-of-the-envelope showed that L3DP technology has a potential to offer lower price for manufacturing solid oxide electrolyzer stack than the conventional technologies. Comparing with conventional electrolyte-electrode assembly method, the L3DP can allow the materials to decrease 31.3%, the process decrease 31.2%, the energy and power decreases 62.2%.

24) The co-ionic (proton and oxygen ion) conducting composite electrolyte comprised of proton conducting perovskite BCZY ($BaCe_{0.5}Zr_{0.4}Y_{0.1}O_{3-\delta}$) and oxygen ion-conducting fluorite YDC ($Y_{0.5}Ce_{0.5}O_{2-\delta}$) showed a promising total ionic conductivity (>10^{-3} $\Omega^{-1}\cdot cm^{-1}$) at 600 ^oC. The variation of the composite composition and the operating temperature and atmospheres can adjust the transference numbers of protons and oxygen ions.

25) The composite O_2 electrode comprised of the state-of-the-art phase-pure perovskite O_2 electrode material $BaCo_{0.4}Fe_{0.4}Zr_{0.1}Y_{0.1}O_{3-\delta}$ (BCFZY0.1) and the state-of-the-art proton conducting electrolyte material $BaCe_{0.7}Zr_{0.1}Y_{0.1}Yb_{0.1}O_{3-\delta}$ (BCZYYb) was prepared by directly mixing the pre-synthesized phase-pure powders. The performance of this composite electrode is still under further optimization.

26) We found that the water in the printable pastes can degrade the perovskite-type proton-conducting electrolytes and other oxide precursors by leaching the specific elements (e.g., barium) to the solution. The formation of hydroxides in green films might be one reason the RLRS sintered films showed cracks.

27) We discovered a new non-aqueous $C_{16}H_{34}$-based paste recipe based on the preparation of BCZYSm13, which allowed the RLRS of crack-free BCZYSm13 free-standing thin film. A similar $C_{16}H_{34}$-based paste recipe can provide the potential to increase the crack-free area for BCZYYb-based PCESs.

28) We further optimized the one-step RLRS of PCES single cells for improving cell performance. A single cell with an active area of 1.51 cm^2 showed a current density of ~755 mA/cm^2 at 600 ^oC under the applied voltage of 1.3 V.

29) We manufactured a combined single cell by integrating seven small cells derived from a large piece manufactured by one-step RLRS. The combined cell has an active area of ~6.6 cm^2. We achieved a stable current density of ~350 mA/cm^2 at 600 ^oC and 1.3 V in the electrolysis cell mode. There was no degradation within 200 h.

30) The use of $C_{16}H_{34}$ as ball-milling solvent to prepare electrolyte precursor powders improved the conductivity of both BCZYSm and BCZYYb electrolytes in the single cell mode compared to the use of ethanol as ball-milling solvent. The high conducitivity of 0.018 S/cm^2 was obtained for BCZYYb electrolyte at 600 ^{o}C.

31) The picosecond laser with power of 100W could successfully cut microchannel in green soft surface and hard glass surface. The channels could be easily controlled with width of 50-150μm and depth 50-300 μm, which can be used to introduce gas distribution channels in electrodes.

32) The multilayer PCEC stack was successfully densigned with microchannels in both hydrogen and oxygen electroodes. The pressure drop through the five-cell stack is around 1% and 6% when the gas flow rates are 100ml/min and 1000 ml/min. When the electrode porosity is around 30-40%, the hydrogen diffusion thorugh the electrode layers only need 0.01S.

33) The single cells consisting of a more sinterable electrolyte (BCZYSm13) and a less sinterable H_2 electrode (40wt% BCZYYb +60wt% NiO) can demonstrate an improved fuel cell performance, which can help the design of PCES structure

34) The BCZYYb strips manufactured by the RLRS method can achieve a proton conductivity as high as 1.5x10^{-2} S·cm^{-1} at 600 ^{o}C, consistent with the proton conductivity for an epitaxial BCZYYb electrolyte.

35) The Ps-laser could machine microchannels with the desired dimension on a sintered electrolyte surface.

36) The on-demand program for controlling the Galvo scanner laser sintering provided the significant potential to achieve large-area crack-free film and cells than the point laser and cylindrical laser scanning. It also made the control of proton ceramic microstructure much easier.

37) The modified paste recipe and 3D printing parameters allowed printing smooth and defect-free green H_2 electrode layers and half-cells on porous nickel substrate and alumina fiber substrate.

38) The new program could control the Galvo scanner to the move CO_2 laser fast enough to form line laser and circular laser, allowing sinter protonic ceramic film, half cells in a rectangle with a width greater than 10mm and in a circular area.

39) A small amount of CeO_2 and YSZ fibers in the H_2 electrode paste did not affect the paste preparation process and 3D printing process, enhancing the electrode toughness and decreasing cracks in sintered half cells.

40) Both the porous nickel foam substrate and the alumina fiber substrate could improve the half cells' integrity and decrease the cracks. The half-cells could successfully bond to nickel foam, making it easier for the following fabrication process of single-cell and stack.

41) The 3D printing on nickel foam substrate allowed assembling single-piece large-area single cells for performance evaluation. The first cell showed a peak power density of ~82 mW·cm^{-2} at 650 ^{o}C.

42) The Galvo laser successfully sintered half-cells with a width larger than 14 mm and an area larger than 5cm, which showed the potential to fabricate one-piece cells with an area larger than 20 cm^2.

43) We have started to reach out to the industrial partner to perform the market transformation plan.

44) The long-term test for small area single cells (~0.5cm^2) at 600^oC has not been 100% finished yet because we cannot regularly access the Clemson campus to do hydrogen-related experiments, especially long-term experiment.

45) We discovered that the protonic ceramic fuel cell (PCFC) single cells with BCZYYb ($BaCe_{0.7}Zr_{0.1}Y_{0.1}Yb_{0.1}O_{3-\delta}$) and BCZYSm13 ($BaCe_{0.7}Zr_{0.1}Y_{0.07}Sm_{0.13}O_{3-\delta}$) as electrolytes showed barium loss after co-firing even at 1400 ^oC, resulting in low proton conducting compared to respective thick pellets.

46) The picosecond laser cutting could decrease the electrolyte layer thickness and modify the interface property by introducing different surface morphologies. Both electrolyte ohmic resistance and the cathode polarization resistance (interfacial charge transfer) decreased significantly after removing the whole surface layer of co-fired electrolyte.

47) The proton ceramic electrolysis cell (PCEC) single-cell of 40wt% BCZYYb + 60wt% NiO | laser-polished BCZYYb electrolyte | BCFZY0.1 ($BaCo_{0.4}Fe_{0.4}Zr_{0.1}Y_{0.1}O_{3-\delta}$) showed initial current density as high as 1.47 A/cm_2 at 600 ^oC under the electrolysis, which is much higher than our milestone value (1.0 A/cm^2). However, the performance degraded quickly because of gas leakage.

48) The picosecond laser cutting could prepare microchannels with open width as narrow as 50 μm and an aspect ratio higher than 6 (based on green H_2 electrode cutting). The achievement solved all the challenges for making microchannels in this research.

49) The rapid Galvano laser scanning (RGLS) technique could prepare anode layers and half cells with desired microstructures. The crack-free rectangular cells reached a width of 20mm and a functional area large than 7 cm^2.

50) The BCZYYb electrolyte thin film prepared by optimized RLRS conditions achieved a proton conductivity as high as 1.45×10^{-2} $\Omega^{-1}cm^{-1}$ at 600 ^oC, which was much higher than the samples prepared by conventional furnace sintering methods.

51) The BCFZY0.1 O_2 electrode with desired microstructure and crystal structure was fabricated by RLRS, allowing the direct L3DP of O_2 electrodes on pre-sintered electrolytes.

52) We fabricated new PCFC single cells with the state-of-the-art $BaZr_{0.8}Zr_{0.2}O_{3-\delta}$ (BZY20) and the new $BaCe_{0.5}Zr_{0.4}Y_{0.1}O_{3-\delta}$-$Y_{0.5}Ce_{0.5}O_{2-\delta}$ (BCZY-YDC) electrolytes and 40wt% BCZYYb +60wt% NiO anode, followed by screen-printing BCFZY0.1 cathode. The single cells based on BZY20 and BCZY-YDC electrolytes showed peak power densities of 202 and 261 mW/cm^2 at 600 ^oC under Air/H_2 gradient.

53) We identified a new segmented-in-series PCES design, allowing manufacture PCES much easier using our current mature techniques since the new design involves long rectangular single cells with a narrow width (e.g., 3mm), which is the exact geometry that our RLRS technique has demonstrated.

54) The PCFC single cells prepared based on the rapid Galvano laser scanning showed the peak power density around 255 mW/cm^2 at 600^{o}C, an excellent value considering the initial manufacturing and testing.

55) The tri-layer cells fabricated by two-time RLRS scanning showed a peak power density of around 320 mW/cm^2 at 600^{o}C, a promising result and much higher than the previous one (~230 mW/cm^2).

56) We fabricated and tested five single cells to achieve high and stable electrolysis current density. The 40wt% BCZYYb + 60wt%NiO | BCZYYb+1wt% | BCZYYb + BCFZY0.1 with anode functional layer fabricated by tape-casting followed by solid state reactive sintering method showed steady electrolysis operation at 600 ^{o}C and 1.3V. The current density of around 1.05A did not show any degradation for more than 280 h.

57) The new CO_2 laser (250 W) can sinter half cells with effective area and microstructure similar to those half-cells sintered using previous CO_2 laser (100W). Although some cracks still existed, the uneven periodical sintering did not occur along the laser scanning direction anymore. The width of rectangular half cells could be larger than the previous cells.

58) The single cells made from the half-cells sintered by the new CO_2 laser showed even better fuel cell/electrolysis performance than those prepared by the previous laser. The peak power densities at 700 ^{o}C, 650 ^{o}C and 600 ^{o}C is 852 mW/cm^2, 646 mW/cm^2 and 498 mW/cm^2.

59) The picosecond laser cutting could decrease the electrolyte layer thickness and modify the interface property by introducing different surface morphologies. Both electrolyte ohmic resistance and the cathode polarization resistance (interfacial charge transfer) decreased significantly after removing the whole surface layer of co-fired electrolyte.

60) The symmetrical cells of BCFZY0.1 | BCZYYb+1wt% | BCFZY0.1 with laser-cut electrolyte showed significantly improved cathode ASR stability. After operating for around 200h, the electrode ASR increased to 1.16 Ω·cm^2 from 0.97 Ω·cm^2. The degradation is 19.6%. The corresponding ASR degradations of the sandpaper-polished and original cells are 414% and 90%. Ps-laser-cut cells demonstrated excellent durability.

61) The single cells made from laser-cut electrolytes show promising performance. The peak power density is 825, 770, 605, and 440 mW/cm^2 at 700, 650, 600 and 550 ^{o}C, respectively.

62) We fabricated single cells of 40wt% BCZYYb + 60wt% NiO | anode functional layer (AFL) | BCZYYb+1wt%NiO | BCZYYb +BCFZY0.1 by tape casting-solid state reactive sintering method and tested their electrolysis stability performance. The cells showed a steady water electrolysis operation at 600 ^{o}C and 1.3V. The current density of ~1.06A did not show any degradation for ~1000 h.

63) We improved the reproductivity of the rapid laser reactive sintering (RLRS) technique based on 250 W CO_2 laser for preparing 40wt% BCZYYb + 60wt% NiO | BCZYYb + 1wt% NiO half cells. Multiple half-cells showed a width between 5 mm to 10mm and a length of ~90 mm. The half-cell achieved the desired thickness of ~300 μm. The half-cells are ready to be further fabricated into single cells with an area larger than 1 cm^2 for performance testing. The large-area cells are also ready to be integrated into segmented-in-series stacks.

64) The large-area single cells (1.43 cm^2) comprised of RLRS-manufactured half cells (40wt% BCZYYb + 60wt% NiO | BCZYYb +1wt% NiO) and brushed cathode (BCFZY0.1)

demonstrated an excellent fuel cell performance under air/H_2 gradient. The peak power densities were 705 mW/cm^2 and 635 mW/cm^2 at 700^{o}C and 650^{o}C under air/H_2 gradient.

65) The complete laser processed small-area single cells demonstrated excellent initial stability. One cell showed a current density around 0.65 A/cm^2 at 600 ^{o}C while applying 1.5 V for more than 100 h without observed degradation.

66) The large-area single cells (1.54 cm^2) comprised of RLRS-manufactured half cells (40wt% BCZYYb + 60wt% NiO | BCZYYb +1wt% NiO) and brushed cathode (BCFZY0.1) demonstrated an excellent fuel cell performance under air/H_2 gradient. The peak power densities were 796 mW/cm^2 and 460 mW/cm^2 at 700 ^{o}C and 550 ^{o}C under air/H_2 gradient, which is even higher than the performance of the state-of-the-art button cells (~0.5 cm^2) fabricated by SSRS method.

67) The reproductivity of single cells by two-step laser sintering (also complete laser processing) was further improved. These complete laser-processed single cells demonstrated extremely high fuel cell performance. The small-area single cells demonstrated the peak power densities of 1014 mW/cm^2, 825 mW/cm^2, and 709 mW/cm^2 at 700 ^{o}C, 650 ^{o}C, and 600 ^{o}C under air/H_2 gradient. This performance is much higher than the single cells we prepared using conventional methods.

68) The reproductivity of single cells by two-step laser sintering (with post-infiltration of active cathode phase) was further improved. These two-step laser-processed single cells demonstrated extremely high fuel cell performance. The small-area single cells demonstrated the peak power densities of 1111 mW/cm^2, 975 mW/cm^2, 797 mW/cm^2, 613 mW/cm^2, and 410 mW/cm^2 at 700^{o}C, 650^{o}C, 600^{o}C, 550^{o}C and 500^{o}C under air/H_2 gradient. This performance is much higher than the single cells we prepared using conventional methods.

69) The long-term stability for two-step laser sintered single cells (with infiltrated active cathode phase) showed very good stability within 100 h. The performance degradation is less than 5% per 100 h.

70) The porous cathode of BCFZY was successfully deposited on laser-sintered half cells by spray coating followed by second-laser sintering. The sandwiched single cells were completely fabricated by laser 3D printing without any high-temperature post-processing.

71) The two-step laser sintering (lower energy and higher energy) based on Galvanometer-scanner could also achieve perfect homogenous half cells with a width of around 10 mm, which showed the potential to manufacture cells with around 20 mm.

72) A segmented in series (SIS) stack with 3 cm^2 demonstrates excellent performance. The peak power density of the stack is 888 mW/cm^2 at 650 ^{o}C, and the corresponding OCV is 3.203 V, which is comparable to the single cell. Furthermore, this stack was stable ope 550 ^{o}C over 250 h.

73) We obtained desired morphology of the cathode and robust electrolyte/cathode interface. It means the full cells sintering process enables 100% laser sintering without any furnace.The all-component laser-sintering cell demonstrated excellent performance. A 1.11 cm^2 ce ll showed 949 mW/cm^2 peak power density at 700 ^{o}C.

74) We achieved significant progress on SIS stacks. A 7-cell stack with a total effective area of 9.23 cm^2. The other one was a 3-cell stack with a total effective area of 8.7 cm^2. Both stacks

demonstrated excellent performance. The stacks' maximum powers reached 7157 mW and 6931Mw at 650 ^{o}C. Corresponding peak power densities are 810 mW/cm^2 and 825 mW/cm^2, respectively, comparable to the small-area single cells. Stack 2 operated stably with 500 mA/cm^2 at 600 ^{o}C over 200 h, indicating that L3DP is one of the promising fabrication methods.

75) The repeatable PCES single cells with an effective area greater than 10 cm^2 were successfully manufactured using the L3DP technique. We demonstrated the capability of manufacturing PCFC cells with an area larger than 14 cm^2. The electrolyte can be as thin as 10 μm.

76) We designed the rapid laser 3D printer for manufacturing ceramic-based energy devices, which is 150 times more than the conventional tape-casting and furnace-firing technique.

77) We have convinced private companies and national labs to jointly apply funds with us for next-level R&D research based on the current technology.

1.2 Summary of Milestone Completion

The summary of the projection milestone completion was summarized in **Table 1**, from which we can see we have almost finished all the milestone requestion.

Table 1. The summary of the project milestone completion

Project milestone (MS) metrics	Achieved MS Metrics	MS completion
1.1 The promising electrolyte, O_2 electrode, and H_2 electrode with individual ASR <0.1Ω·cm^2 and proper interconnect with ASR <0.01Ω·cm^2 should be obtained at 600^{o}C	Total hydrogen electrode 0.2 Ω·cm^2, oxygen electrode 0.053 Ω·cm^2, electrolyte 0.1 Ω·cm^2 assuming thickness of 9 μm, interconnect 0.01 Ω·cm^2 assuming large thickness of 1 mm.	**100%**
1.2 PCES single cells with area >0.5cm^2 fabricated by SSRS should achieve a current density >1.0A/cm^2 at 1.3V and a performance degradation rate <1.0% per 1000 h at 600^{o}C	A single cell of 40wt% BCZYYb + 60wt% NiO | anode functional layer (AFL) | BCZYYb+1wt%NiO | BCZYYb + BCFZY0.1 was fabricated by tape casting method, demonstrating stable electrolysis at 600 ^{o}C for more than 1000 h with a constant current density of 1.05 A/cm^2 while applying a voltage of 1.3 V.	**100%**
2.1 The crack-free green films of each PCES component with an area of 10x10cm^2 and thickness 20-1000μm will be manufactured by 3D printing using the developed pastes.	Complent film area >10x10 cm^2, thickness 30-1000 μm (no need to to <30μm).	**100%**
2.2 The crack-free PCES component films with an area >6cm^2 and thickness of 5-200μm will be manufactured by L3DP. The electrolyte (pinhole-free), O_2 electrode (highly porous), and H_2 electrode (highly porous) films with ASRs	All the component area is >6 cm^2, summary area is ~120 cm^2. Thikcnes 5-200 μm. Electrolyte ASR, 0.08 Ω·cm^2, hydrogen electrode 0.0744	**100%**

<0.1Ω·cm^2 and interconnect with ASR <0.01Ω·cm^2 should be obtained at 600^{o}C.	Ω·cm^2, oxygen electrode 0.1 Ω·cm^2, interconnect 0.001 Ω·cm^2	
3.1 The effective binding without obvious interfacial and component performance deterioration will be achieved.	Well binding for both green films and RLRS films. Not effect on ASRs was found.	**100%**
3.2 The effective infiltration in the L3DP electrodes showing OER and HER ASRs <0.1Ω·cm^2 at 600^{o}C should be achieved.	The infiltrated oxygen electrode has ASR of 0.1 Ω·cm^2	**100%**
3.3 The PCES single cells with area >5cm^2, current density >500 mA/cm^2 at 1.3V and stable operation with degradation rate <1% for >200 h at 600^{o}C will be successfully manufactured by L3DP.	RLRS single cell >10cm^2. Measured single cells ~1.35 cm^2. Stability 166 h. Current density 530 mA/cm^2. No degradation. We manufactured a combined single cell by integrating seven small cells derived from a large piece manufactured by one-step RLRS. The combined cell has an active area of ~6.6 cm^2. We achieved a stable current density of ~350 mA/cm^2 at 600 ^{o}C and 1.3 V in the electrolysis cell mode. There was no degradation within 200 h.	**100%**
3.4 The quick back-of-the-envelope will show that L3DP technology has the potential to offer the lower price for manufacturing solid oxide electrolyzer stack than conventional technologies.	Comparing with electrolyte-electrode assembly. Materials decrease 31.3%, process decreases 31.2%, the energy and power decreases 62.2%	**100%**
Go-Not-Go Point for BP1. PCES single cells with area >5cm^2, current density >500mA/cm^2 at 1.3V and stable operation with degradation rate <1% for >200 h at 600^{o}C by L3DP. The back-of-the-envelope calculation will show the potential for the L3DP technology to be cost incentive comparing to conventional technologies.	RLRS single-cell >6cm^2 (summary area >120cm2) were prepared by L3DP. The measured single cells ~1.35 cm^2. The stability of 166 h was achieved without degradation. Current density 530 mA/cm^2. The combined cell has an active area of ~6.6 cm^2. We achieved a stable current density of ~350 mA/cm^2 at 600 ^{o}C and 1.3 V in the electrolysis cell mode. There was no degradation within 200 h. Comparing with the conventional electrolyte-electrode assembly method, the L3DP can allow the materials to decrease 31.3%; the cell processing cost decrease by 31.2%, the energy, and power decrease by 62.2%.	**100%**
4.1 The interconnects with designed microchannels should be obtained, which should	The picosecond laser with power of 100W could successfully cut microchannel in green soft surface	**100%**

show negligible mass transport resistance and no deterioration to current collecting performance.	and hard glass surface. The channels could be easily controlled with width of 50-150μm and depth 50-300 μm, which can be used to introduce gas distribution channels in electrodes.	
4.2 The program to control L3DP to manufacture designed PCES should be achieved.	The multilayer PCEC stack was successfully densigned with microchannels in both hydrogen and oxygen electroodes. The pressure drop through the five-cell stack is around 1% and 6% when the gas flow rates are 100ml/min and 1000ml/min. When the electrode porosity is around 30-40%, the hydrogen diffusion thorugh the electrode layers only need 0.01S.	**95%**
4.3 PCES with cells >5 and area >100 cm^2 will be manufactured by the proposed L3DP technology. The current density >1 A/cm^2 at 1.3 V and degradation rate <1% per 1000 h at 600 ^oC	We achieved significant progress on SIS stacks. A 7-cell stack with a total effective area of 9.23 cm^2. The other one was a 3-cell stack with a total effective area of 8.7 cm^2. Both stacks demonstrated excellent performance. The stacks' maximum powers reached 7157 mW and 6931Mw at 650 ^oC. Corresponding peak power densities are 810 mW/cm^2 and 825 mW/cm^2, respectively, comparable to the small-area single cells. Stack 2 operated stably with 500 mA/cm^2 at 600 ^oC over 200 h, indicating that L3DP is one of the promising fabrication methods.	**95%**
5.1 The models for estimating the electrolyzer manufacturing cost by L3DP technology will be established for predicting H_2 cost by H2A3. The key parameters for further decreasing H_2 cost to meet DOE's target of \$2/kg H_2 will be identified.	The calculated hydrogen production cost is around 2.74~2.88 \$/kg with our L3DP electrolysis cell. The hydrogen cost is reduced by 1~6.5% compared with T. Ramsden's result. But hydrogen production cost primarily depends on the price of electricity and thermal heat, no matter our result or the result of T. Ramsden. The lower energy cost for the electrolyzer stack is another point for reducing hydrogen production. The hydrogen cost of our L3DP electrolysis cell coupled with the nuclear reactor was calculated in this quarter. It is around 2.75-2.88 \$/kg. The cost of the electrolyzer stack	**95%**

	fabricated by our L3DP method significantly reduced the capital costs	
5.2 The industrial partner, who is interested to scale up this technology to speed up the technology to market will be located. The reasonable scale-up plan should be made.	We have convinced private companies and national labs to jointly apply funds with us for next-level R&D research based on the current technology.	**95%**
End of Project Goal. A PCES composed of >5 single cells with total area >100cm^2 will be manufactured by the L3DP technology. The current density >1A/cm^2 at 1.3 V and degradation rate <1% per 1000h at 600 ^{o}C will be successfully achieved. The H_2 cost based on the initial TEA should decrease >50% compared to the state-of-the-art electrolyzers and show the trend to be close to $2/kg. The TRL will be boosted to >4 and the potential industrial partner will be found and scale up should be made.	We achieved significant progress on SIS stacks. A 7-cell stack with a total effective area of 9.23 cm^2. The other one was a 3-cell stack with a total effective area of 8.7 cm^2. Both stacks demonstrated excellent performance. The stacks' maximum powers reached 7157 mW and 6931Mw at 650 ^{o}C. Corresponding peak power densities are 810 mW/cm^2 and 825 mW/cm^2, respectively, comparable to the small-area single cells. Stack 2 operated stably with 500 mA/cm^2 at 600 ^{o}C over 200 h, indicating that L3DP is one of the promising fabrication methods. The hydrogen cost of our L3DP electrolysis cell coupled with the nuclear reactor was calculated in this quarter. It is around 2.75-2.88 $/kg. The cost of the electrolyzer stack fabricated by our L3DP method significantly reduced the capital costs.	**95%**

2 Detailed Evidence to Prove Milestone Completion

Budget Period 1: Protonic Ceramic Electrolyzer Single Cells by Laser 3D Printing

Task-1 PCES Materials Development

Milestone 1.1 Based on ST-1.1 Discovery of New PCES Materials

Milestone 1.1 is based on the ST-1.1 Discovery of New PCEC Materials. The promising electrolyte, O_2 electrode, and H_2 electrode with individual ASR <0.1Ω·cm^2 and proper interconnect with ASR <0.01Ω·cm^2 should be obtained at 600^{o}C. The following detailed results and discussion on electrolytes, O_2 electrodes, H_2 electrodes, and interconnects indicsolid-state finished ~100% of this milestone.

1) The new $BaCe_{0.7}Zr_{0.1}Y_{0.07}Sm_{0.13}O_{3-\delta}$ (BCZYSm13) electrolyte can achieve ASR less than 0.1 Ω·cm^2 at 600^{o}C to meet electrolyte ASR milestone metric.

The dense BCZYSm13 pellets were fabricated using solid state reactive sintering (SSRS) from $BaCO_3$, CeO_2, ZrO_2, Y_2O_3, Sm_2O_3, and 1wt% NiO after sintering at 1400 °C for 18 h. Compared with other protonic ceramic electrolyte materials such as $BaCe_{0.7}Zr_{0.1}Y_{0.1}Yb_{0.1}O_{3-\delta}$ (BCZYYb), $BaCe_{0.6}Zr_{0.3}Y_{0.1}O_{3-\delta}$ (BCZY63), and $BaZr_{0.8}Y_{0.2}O_{3-\delta}$ (BZY20), the sintering temperature was significantly lowered. The proton conductivity was measured using electrochemical impedance spectroscopy (EIS) based on the standard symmetrical cells comprised of a thick and dense electrolyte pellet and two thin porous silver electrodes of both surfaces. The electrical conductivities measured at 600 °C under wet air atmosphere are summarized in **Figure 1**. For comparison, the conductivity for some other electrolyte pellets was included. The highest electrical conductivity ~$9x10^{-3}$ S/cm was obtained for the compound of BCZYSm13, which was even higher than the state-of-the-art BCZYYb electrolyte measured in our laboratory. The dense electrolyte thin films with a thickness of 5-10 μm were obtained by our RLRS method for the model material of BCZYYb (**Figure 2**). Therefore, it is easy to achieve a BCZYSm13 thin film with a thickness of less than 9 μm to achieve the ohmic ASR less than 0.1 Ω·cm^2.

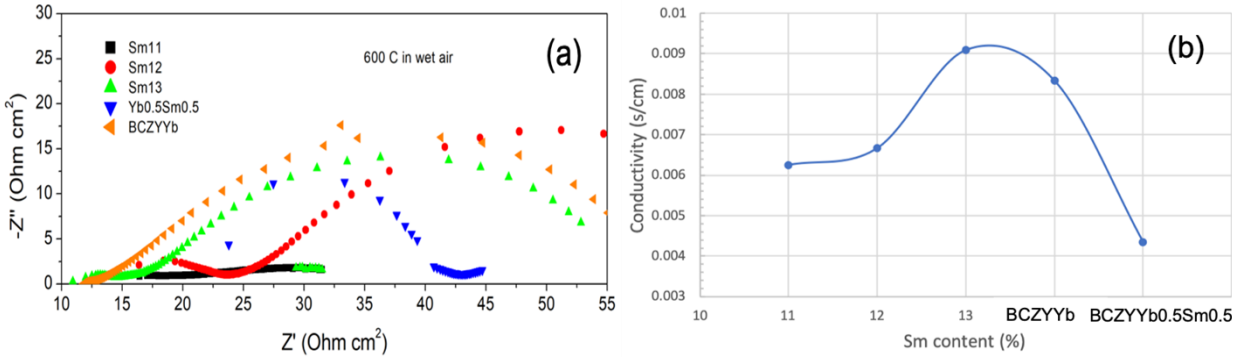

Figure 1. EIS spectra (a) and electrical conductivities (b) of $BaCe_{0.7}Zr_{0.1}Y_{0.2-x}Sm_xO_{3-\delta}$ (x=0.11, 0.12, 0.13), BCZYYb and $BaCe_{0.7}Zr_{0.1}Y_{0.1}Yb_{0.05}Sm_{0.05}O_{3-\delta}$ pellets measured at 600°C in wet air (with ~3 vol.% H_2O) using symmetrical cells.

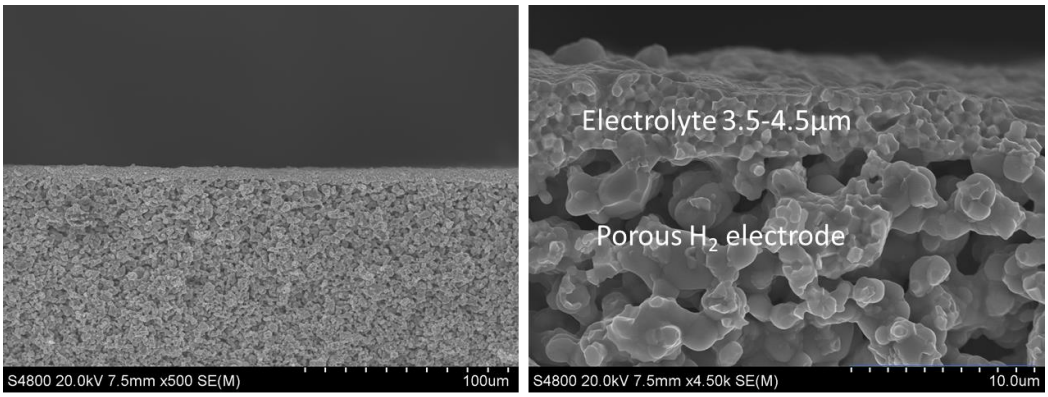

Figure 2. Fully densified BCZYYb thin was supported on 40wt% BCZYYb +60wt% NiO H_2 electrode by RLRS.

2) The new H_2 electrode of 40wt% BCZYSm13+60wt% NiO combined with our O_2 electrode of BCZY63 scaffold infiltrated with $BaCo_{0.4}Fe_{0.4}Zr_{0.1}Y_{0.1}O_{3-\delta}$ (BCFZY0.1) showed a total electrode ASR of 0.2 Ω·cm^2, which successfully met the milestone metrics of (0.1 Ω·cm^2 for the cathode and 0.1 Ω·cm^2 for the anode).

The single cells of 40wt% BCZYSm13+60wt%NiO | BCZYSm13 | BCZY63+BCFZY0.1 were fabricated by the SSRS method. The H_2 electrode precursor powder was dry-pressed under 350 MPa for 2 minutes in a circular die set with a diameter of 19 mm to produce green H_2 electrode pellets. Then a thin electrolyte precursor paste layer was deposited on both sides of the green H_2 electrode precursor pellets using screen-printing. Then the O_2 electrode scaffold precursor paste layer was subsequently coated on top of one of the electrolyte layers. The overall structure was fired at 1400 °C for 18 h. The as-obtained BCFZY0.1 solution was infiltrated into the pores of the O_2 electrode scaffold structure using a microliter to control the loading amount. After infiltrating the porous O_2 electrode scaffold with the solution, the infiltrated cells were fired at 400 °C for 1 h. This procedure was repeated until the desired weight loading of BCFZY0.1 was achieved. Finally, the single cells were heated in air to 900 °C for 5 h to produce the nanocrystalline perovskite structure of BCFZY0.1. The electrode polarization resistance was measured using EIS under open-circuit conditions while applying the Air/H_2 chemical gradient. The ASRs for ohmic resistance of the electrolyte membrane and the total polarization resistance of the oxygen and hydrogen electrode at different temperatures are summarized in **Figure 3**. It can be easily seen that the total electrode ASR is ~0.2 Ω·cm^2 at 600^{o}C.

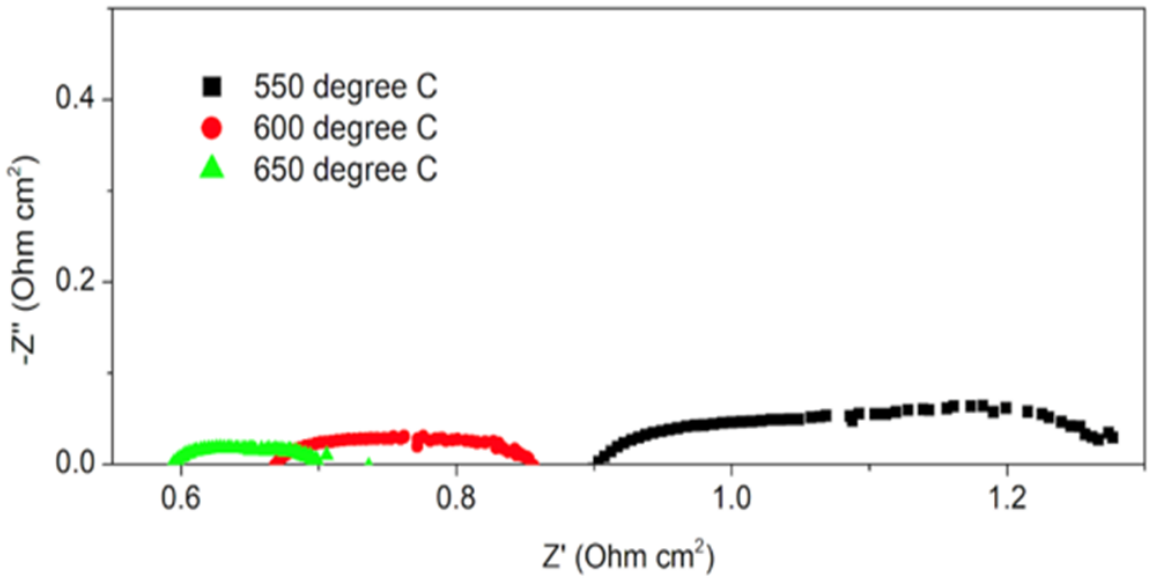

Figure 3. Electrode and electrolyte ASRs measured by EIS at different temperatures for single cells of 40wt%BCZYSm13 + 60wt%NiO | BCZYSm13 | BCZY63 + BCFZY0.1 fabricated by SSRS method followed by further BCFZY0.1 infiltration.

3) The BCFZY0.1 thin-film O_2 electrode prepared by a new ball-milling process showed an ASR of 0.053 Ω·cm^2, which is much better than the milestone metric for the cathode (0.1 Ω·cm^2).

BCFZY0.1 precursor powders were synthesized by a modified Pechini method. Stoichiometric amounts of $Ba(NO_3)_2$, $Co(NO_3)_3{\cdot}6H_2O$, $Fe(NO_3)_3{\cdot}9H_2O$, Zirconyl nitrate (solution), and $Y(NO_3)_3{\cdot}9H_2O$ were dissolved into deionized water. EDTA and citric acid were added at a mole ratio of 1.5: 1.5: 1 for EDTA: citric acid: total metal ions under magnetic stirring condition. $NH_3{\cdot}H_2O$ was then added to dissolve salts totally by adjusting pH value around 10. The clear solute was heated to 80-90 ^{o}C to evaporate the water for forming a viscous gel. The gel was dried in a box oven at 150 ^{o}C for 48 h to form a dark charcoal-like primary powder, which was

then fired at 600 ºC for 5 h followed by ball milling for 7 days in 1-butanol. The cathode precursor powders were obtained by solvent filtration followed by further drying at 500 ºC for 5 h. The cathode precursor powders were further ball-milled in isopropanol for the preparation of cathode paste. The cathode was applied to 40wt%BCZYYb + 60wt%NiO half cell prepared by RLRS and the polarization resistance for the cathode for measured at open-circuit conditions at different temperature while applying Air/H_2 gradient. **Figure 4** shows that the total electrode polarization ASR is 0.13 Ω·cm^2 at 600 ºC, which is further divided into ASR of hydrogen electrode 0.074 Ω·cm^2 and ASR of oxygen electrode 0.053 Ω·cm^2. Therefore, the individual ASRs for both electrodes achieved better metrics than the milestone request (0.1 Ω·cm^2 at 600 ºC).

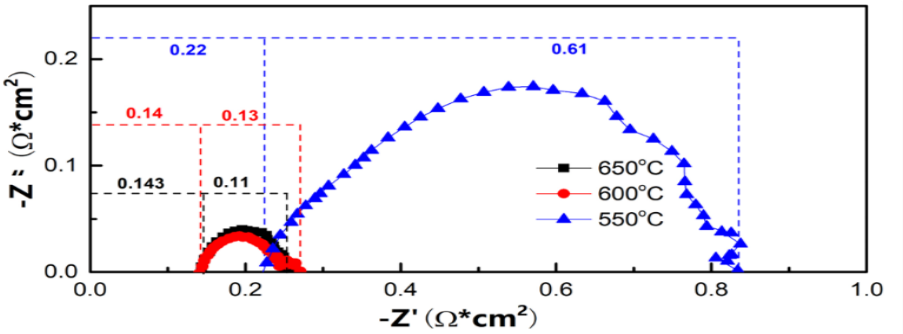

Figure 4. Electrode and electrolyte ASRs measured by EIS at different temperatures for single cells of 40wt%BCZYYb + 60wt%NiO | BCZYYb | BCFZY0.1.

4) The interconnect material $La_{0.7}Sr_{0.3}CrO_3$ (LSCr) was discovered to be compatible with the PCES component materials of BCZYYb, BCFZY0.1, and 40wt%BCZYYb + 60wt%NiO. The conductivity of 16.2 S/cm was obtained at 600°C. Achieving the ASR of 0.01 Ω·cm^2, the thickness of the LSCr can be as thick as 1.6 mm, which is much thicker than we have done (10µm by RLRS).

The LSCr powders were synthesized using the conventional solid-state reaction method. The dense LSCr pellets were obtained after sintering at 1550 °C for 10 h. The conductivity was measured by the four-probe DC method using the dense pellets. **Figure 5** shows the total conductivities change versus the operating temperature in the air. The conductivity of around 16.2 S/cm was obtained at 600 °C. To achieve the ASR of 0.01 Ω·cm^2, the thickness of the LSCr can be as thick as 1.6 mm. The thin interconnect film should have neglectable resistance comparing the electrodes and electrolytes. In order to investigate the compatibility of LSCr with protonic ceramic electrolyzer components, LSCr powder was mixed with an oxygen electrode, hydrogen electrode, and electrolyte materials and then annealed at 700 °C for 60 h in 5% H_2 balanced Ar. **Figure 6** indicates that for LSCr / BCZYYb and LSCr / BCZYYb + NiO, no new phase was found, and the original individual phases were retained. For LSCr / BCFZY0.1, a slight shift toward a small angle for the BCFZY0.1 phase can be observed. This can be ascribed to the lattice expansion of BCFZY0.1 due to the loss of oxygen in the reducing atmosphere. Therefore, the selected LSCr was compatible with other PCES components under normal operating conditions (e.g., 600 ºC).

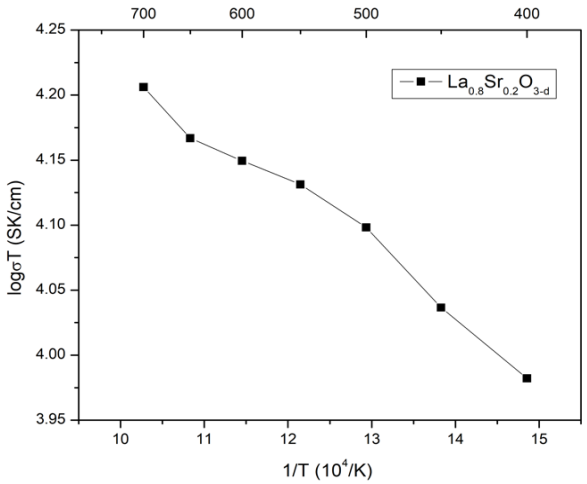

Figure 5. Conductivity of LSCr dense pellets in the air measured by the 4-probe DC method at different temperatures.

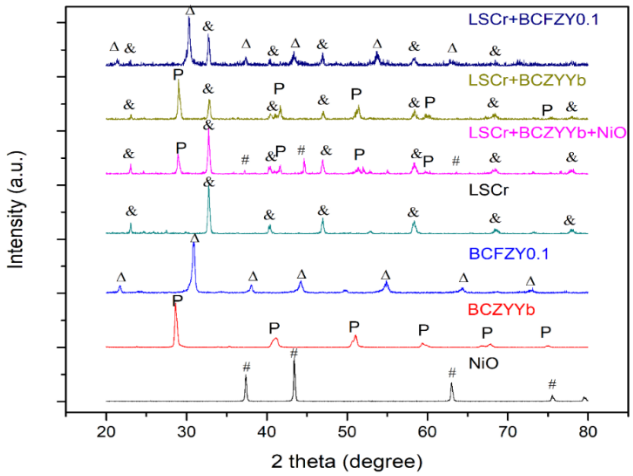

Figure 6. X-ray patterns of LSCr, BCFZY0.1, BCZYYb and the mixtures of LSCr with BCFZY0.1 or BCZYYb treated at 700 °C for 60 h.

Milestone 1.2 Based on ST-1.2 Materials Performance in PCES Single Cells

Milestone 1.2 is based on ST-1.2 Materials Performance of PCES Single Cells. PCES single cells with an area >0.5cm^2 fabricated by SSRS should achieve a current density >1.0 A/cm^2 at 1.3 V and a performance degradation rate <1.0% per 1000 h at 600 ºC. The following detailed results and discussion for protonic ceramic cells (PCC) in both fuel cell and electrolysis modes show that we have finished 100% of this Milestone.

1) Multiple single cells based on our new electrolyte of BCZYSm were fabricated by the SSRS method with an active area of around 0.5 cm^2. The current density of 1.05 A/cm^2 and 1.375 A/cm^2 were achieved at 600 ºC and 650 ºC while applying the voltage of 1.3 V. We have successfully met the milestone metrics of 1.0 A/cm^2 at 600 ºC at 1.3 V.

The single cells comprised of 40wt% BCZYSm13 + 60wt%NiO H_2 electrode, BCZYSm13 electrolyte, and BCZY63 + 0.025wt% Fe_2O_3 + BCFZY0.1 O_2 electrode were fabricated by the conventional SSRS method. The sandwiched structure of the H_2 electrode, electrolyte, and O_2 electrode scaffold were fabricated by sintering at 1400 ºC for 18 h. After the infiltration of the BCFZY0.1 nanophase, the single cells with active area ~0.5 cm^2 were obtained. **Figure 7a** shows that single cells have a fully densified BCZYSm13 electrolyte layer of ~25 μm and a highly porous BCZY63+BCFZY0.1 composite O_2 electrode of ~70 μm. **Figure 7b** further shows that the active O_2 electrode phase of the BCFZY0.1 nanoparticle was deposited on the inside wall of the BCZY63 scaffold by infiltration. This single cell was operated under an electrolysis cell at temperatures from 550 ºC to 650ºC with 15 vol% H_2O humidified air as feed gas and Ar as the sweep gas. **Figure 8a** indicates that the cell can produce a current density of 785 mA/cm^2 with an applied voltage of 1.3V at 600°C. When the operating temperature increased to 650ºC, the current density reached 1375 mA/cm^2, much higher than 1A/cm^2. The hydrogen flux generated in the H_2 chamber was analyzed by measuring the H_2 concentration using gas chromatography (GC) in the exit Ar and H_2 mixture. The H_2 concentration signals in the electrolysis exit gas mixture are shown in **Figure 8b** while operating electrolysis at temperatures of 550 ºC, 600 ºC, and 650 ºC, respectively. The corresponding Faradic efficiencies of the electrolysis at these temperatures were further calculated based on the generated H_2 amount and the theoretical amount calculated from the current density. The relatively high Faradic efficiencies of 94.0%, 83.2%, and 54.3% were

obtained at temperatures of 550 °C, 600 °C, and 650 °C, respectively. By optimizing the fabrication of single cells (e.g., reduce electrolyte thickness, increase H_2 electrode porosity), the similar single cells showed an improved current density of ~1050 mA/cm^2 at 600 °C (**Figure 9**), which is higher than our milestone metrics (1 A/cm^2 at 600 °C).

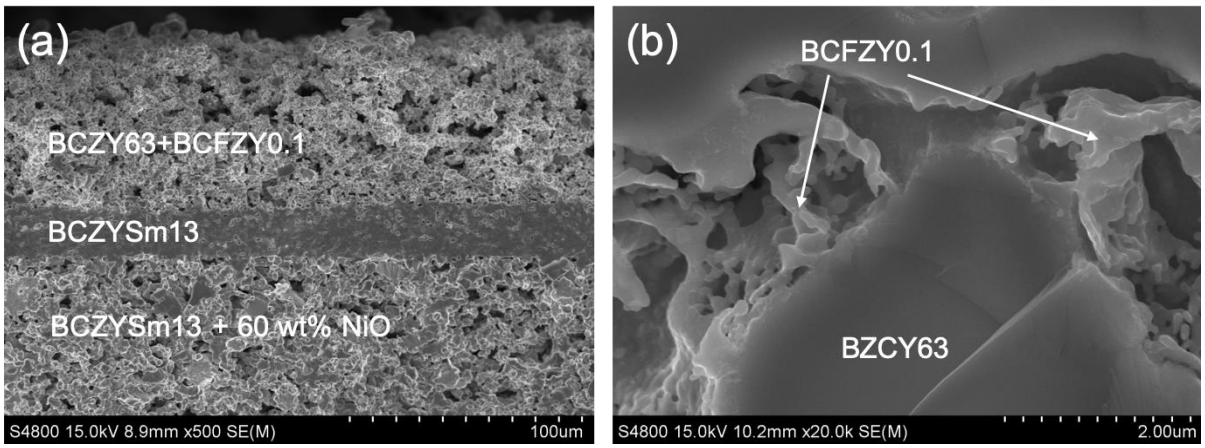

Figure 7. (a) A cross-sectional view of a cell with configuration of Ni-BCZYSm13 | BCZYSm13 | BCZY63-BCFZY0.1, (b) cross-section view of an infiltrated O_2 electrode.

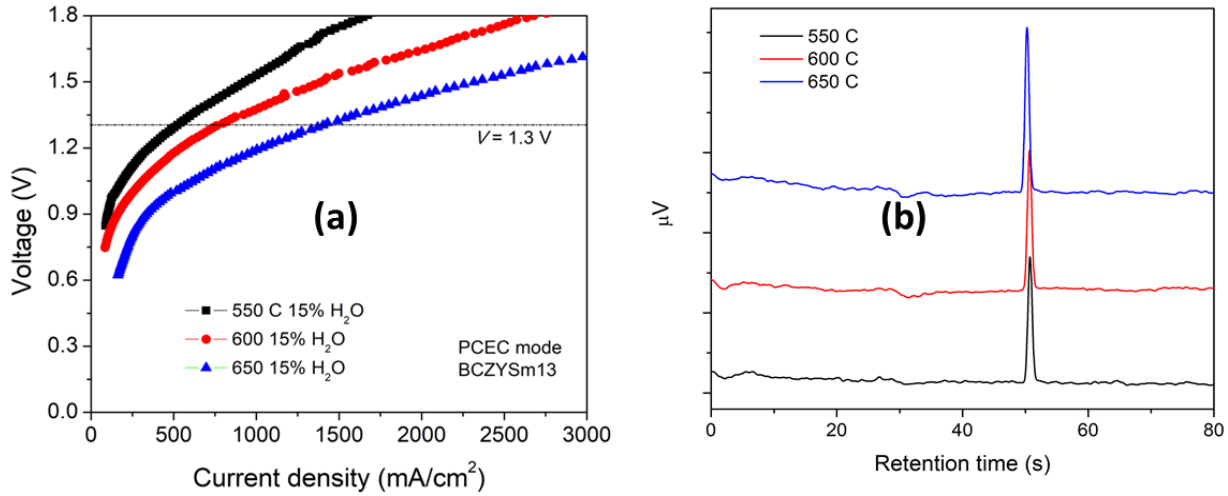

Figure 8. a) I-V curves of 40 wt.% BCZYSm13 + NiO | BCZYSm13 | BCZY63 + BCFZY0.1 single cell under electrolysis mode at temperatures from 550°C to 650°C under Ar/air+15% H_2O and (b) the H_2 concentration signals in H_2 chamber under electrolysis at different temperatures.

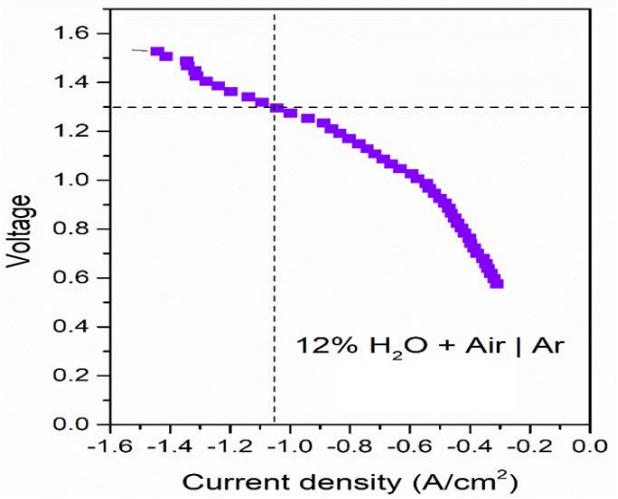

Figure 9. I-V curves of 40 wt.% BCZYYb + 60 wt.% NiO | BCZYSm13 | BCZY63 + BCFZY0.1 single cell measured at 600 °C under 12 vol.% H_2O humidified air/Ar (cathode area: 0.5 cm^2

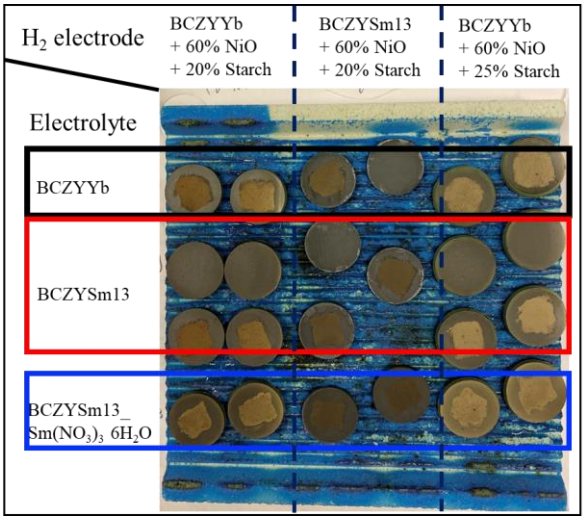

Figure 10. More than 20 single cells based on our new protonic ceramic of BCZYSm were fabricated for testing the long-term stability.

2) Single cell of 40wt% BCZYYb + 60wt% NiO | AFL | BCZYYb+1wt%NiO | BCZYYb + BCFZY0.1 was fabricated by tape casting method, demonstrating stable electrolysis at 600 ºC for more than 1000 h with a constant current density of 1.05 A/cm^2 while applying a voltage of 1.3 V. The long-term stability milesston was met.

Cell fabrication: The single cells of 40wt% BCZYYb + 60wt% NiO | AFL | BCZYYb + 1wt%NiO | BCZYYb + BCFZY0.1 were fabricated by the tape casting and SSRS method. Here, we introduced the anode functional layer (AFL) to improve cell performance. During the tape casting process, the electrolyte layer was the first cast on a Mylar sheet with a Dr. Blade height of 50 µm. The AFL layer was then cast on the top of the electrolyte layer with Dr. Blade's height of 70 µm. Subsequently, the slurry of the anode was cast on the AFL layer with a Dr. Blade height of 2 mm. The three-layer green tape was dried in the air for 48 h and cut into pellets, followed by sintering at 1450 ºC for 18 h. The composite of BCZYYb + BCFZY0.1 (ratio 1:4) was used as the oxygen electrode. The BCZYYb powder was prepared by solid state reaction at 1400 ºC for 10 h. After mixing with BCFZY0.1 by ball-milling, the cathode paste was prepared and brushed on the electrolyte top. Annealing at 900 ºC for 5 h resulted in the single cells for long-term electrolysis testing.

Table 2. Slurry composition of the tape casting method.

Composition	H_2 electrode slurry (g)	Electrolyte slurry (g)	AFL slurry (g)
BCZYYb	51.10 (40wt%)	54.52	10.69 (35wt%)
NiO	76.62 (60wt%)	0.54	19.5 (65wt%) (Sol-gel)
Starch	68.74 (35wt%)		1.5
Ethanol	36.29	16.13	8.06
2-Butanone	24.10	10.71	5.35
Triethanolamine	3.05	1.36	0.68
Polyvinyl butyral (PVB)	8.85	3.94	1.97

Polyethylene glycol	4.5	2	1
Dibutyl o-phthalate	4.5	2	1

Cell performance and characterization: Figure 11 provides the SEM image of the cross-section of a typical cell fabricated by tape casting-SSRS method. The BCZYYb + 1wt% NiO electrolyte is fully densified, and the thickness is around 35 µm. The AFL layer shows a thickness of about 6 µm, adhering to the electrolyte and formal anode seamlessly. The composite cathode shows a homogenous porous morphology and an excellent adherence to the electrolyte layer. **Figure 12** provides the electrolysis performance (current density) versus operating time at 600 ºC under a gradient of 5% H_2 / 30% H_2O with air while applying a voltage of 1.3 V. It is clear that the current density as high as 1.06 A/cm^2 was obtained, which didn't show any degradation for 1000 h. **Figure 13** further shows the ASR of the single cells after stability testing for 1000 h. The polarization ASR is still very small after long-term electrolysis operation. The relatively high electrolyte ASR is consistent with the thick electrolyte (~35 µm). A further decrease in the electrolyte thickness can improve the performance.

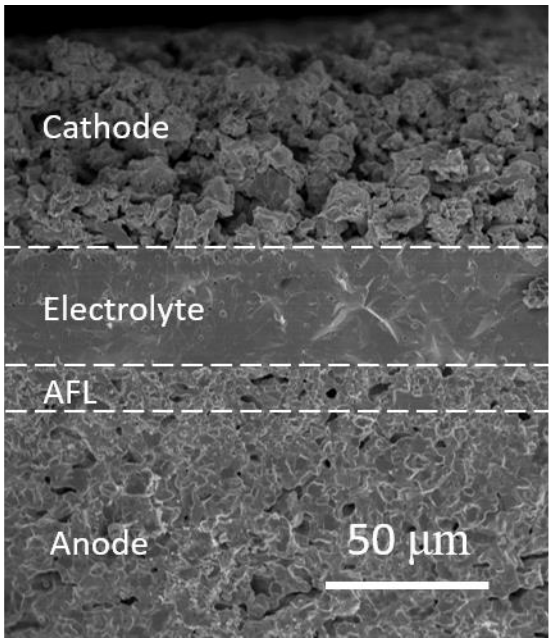

Figure 11. SEM image of single cells of 40wt% BCZYYb + 60wt% NiO | AFL | BCZYYb + 1wt% NiO | BCZYYb + BCFZY0.1 by tape casting-solid state reactive sintering.

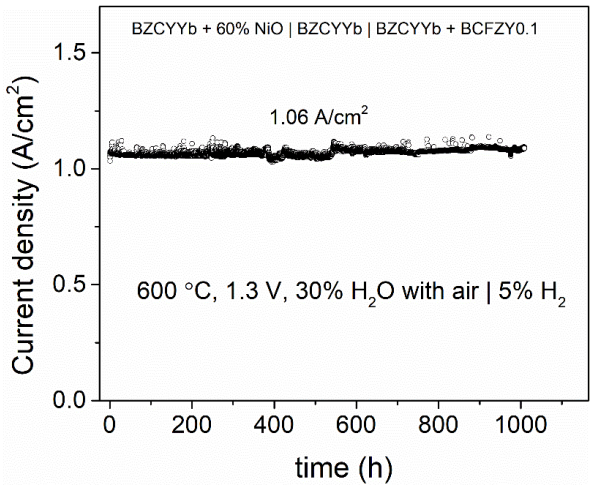

Figure 12. Long-term electrolysis performance of 40wt%BCZYYb + 60%NiO | AFL | BCZYYb + 1wt% | BCZYYb + BCFZY0.1 cell under 30% H_2O in air /5% H_2 gradient.

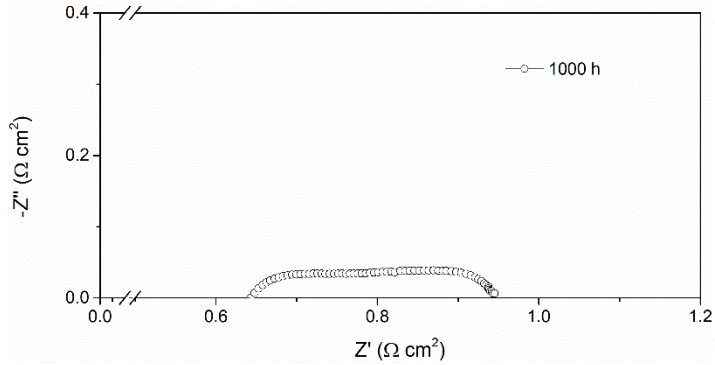

Figure 13. Electrochemical impedance spectroscopy (EIS) testing result (ASR) of 40wt% BCZYYb + 60% NiO | AFL | BCZYYb + 1wt% | BCZYYb + BCFZY0.1 cell under 30% H_2O in air /5% H_2 gradient after long-term stability testing.

Task-2 PCES Component Thin Films by L3DP

Milestone 2.1 Based on ST-2.1 3D Printing of Component Green Films

Milestone 2.1 is based on ST-2.1 Printing of Component Green Films. The crack-free green films of each PCES component with an area of 10x10 cm^2 and thickness 20-1000 μm will be manufactured by 3D printing using the developed pastes. This task includes preparing of printable pastes, printing green layers using microextrusion, and developing new printing techniques for achieving extraordinarily smooth and thin electrolyte green layer. Based on the following detailed results and discussion, we estimate that this milestone has been finished about 100%.

The recipe for achieving printable pastes for a versatile protonic ceramic-based materials systems was developed, which allowed us to 3D print crack-free green films of BCZYYb+1wt%NiO electrolyte, 40wt% BCZYYb+60wt%NiO hydrogen electrode, BCFZY0.1 oxygen electrode, and LSrCr interconnect precursor layers with an area larger than 10cm×10cm and thickness 150-1000μm. The new technique of microextrusion followed with Dr. Blade paving allowed to decrease the thickness of the green film to around 50μm.

The new spray coating based technique allowed to decrease the film thickness further less than 30μm.

Microextrusion-based 3D printing. With BCYZYYb + 1wt%NiO electrolyte precursor paste preparation as an example, the paste preparation procedure is described as follows. After weighing the stoichiometric amounts of the component precursors of $BaCO_3$, CeO_2, ZrO_2, Y_2O_3, Yb_2O_3, and NiO into a Nalgene bottle, the mixture was ball-milled for 48 h with 3 mm YSZ balls in isopropanol solvent. After drying, the well-mixed powders were gradually added to a 5wt% Darvan 821-A aqueous solution while controlling the equal volumes of precursor powder and water. After ball-milling for another 48 h, 2wt% of HPMC (Methocel^{TM} J4M S Hydroxypropyl Methylcellulose) was added to thicken the slurry into a viscous paste. After further mechanical stirring for 1 h, the BCZYYb + 1wt%NiO printable paste was obtained (**Figure 14**). All the other pastes mentioned above were prepared using a similar procedure. Using the microextrusion method, we can easily print the green layer with a thickness of 150-1000 μm. **Figure 15** shows the SEM image of a representative BCZYYb electrolyte precursor green films obtained by 3D printing in our lab.

Figure 14. Printable 40wt% BCZYYb + 60wt% NiO anode precursor paste.

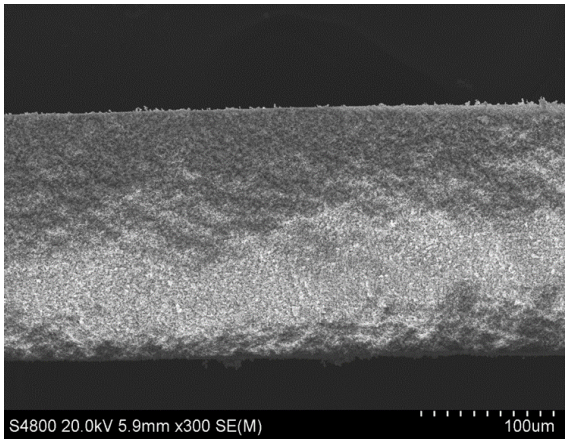

Figure 15. SEM image of the cross-section of BCZYYb electrolyte precursor green film.

Following the same procedure described above, we prepared the pastes of BCZYYb + 1wt% NiO electrolyte, 40wt% BCZYYb + 60wt% NiO H_2 electrode, BCFZY0.1 O_2 electrode, and LSCr interconnects. Using our microextrusion method, we can easily print green films with thicknesses around 150-1000 μm for all tour components. **Figure 16** provides the photos of all thecomponentt precursor green films, which indicates that the active areas are higher than 100cm^2 and the surface is very smooth, which successfully met milestone metrics (100 cm^2 for green component films). The green film is very homogenous, and the thickness is around 200μm. Furthermore, the bonding between green component layers was confirmed. **Figure 17a** further shows that the three layers of hydrogen electrode, electrolyte, and oxygen electrode were bonded together very well. **Figure 17b** shows that a representative cross-sectional image of electrolyte green film printed on H_2 electrode film. The excellent bonding between the electrolyte film and the H_2 electrode film was achieved for 3D printed green half cells.

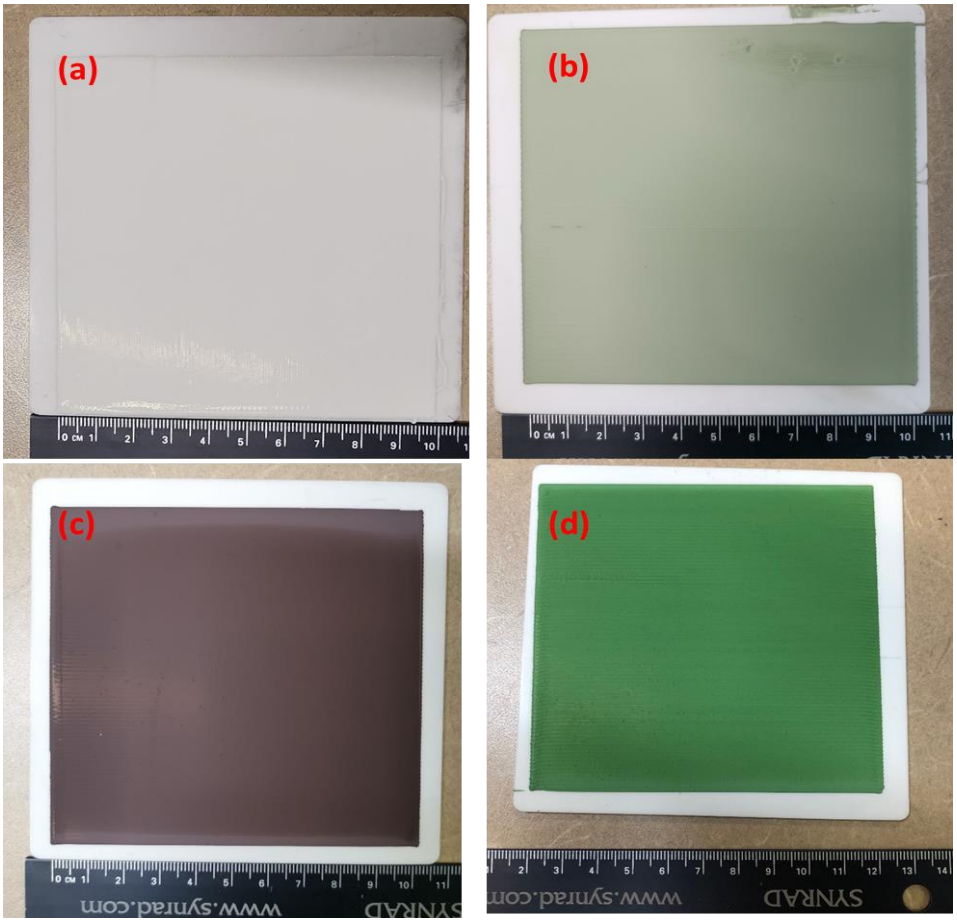

Figure 16. Photos of PCES component precursor green films printed by a microextrusion-based 3D printing technique. (a) BCZYYb+1wt%NiO electrolyte, (b) 40wt%BCZYYb+60wt%NiO H_2 electrode, (c) BCFZY0.1 O_2 electrode, and (d) LSCr interconnect.

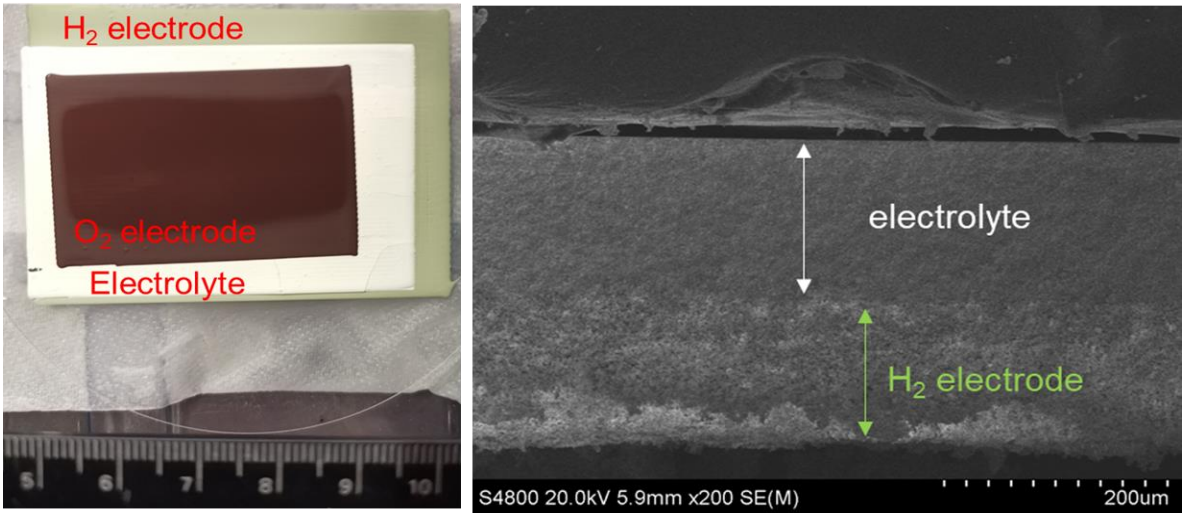

Figure 17. a) Three layers of H_2 electrode, electrolyte, and O_2 electrode printed by microextrusion-based 3D printing technique and (b) SEM image of two-layer cross-section (electrode green film on H_2 electrode green film).

3D printing based on microextrusion, followed by Dr. Blade smoothing. We introduced a Dr. Blade to decrease the thickness of the extruded green films (**Figure 18a**). The deposition of the H_2 electrode paste and BCZYYb electrolyte paste was studied in detail. A lower HPMC binder amount was added to the paste compared to the regular paste for extrusion to reduce the viscosity and enhance the uniformity of the film. When the blade-substrate distance was set at about 100 μm, the deposited film was uniform, and the thickness was < 50μm after drying, as shown in **Figure 18b** and the relatively large area of 12 cm^2 was obtained (**Figure 18c**).

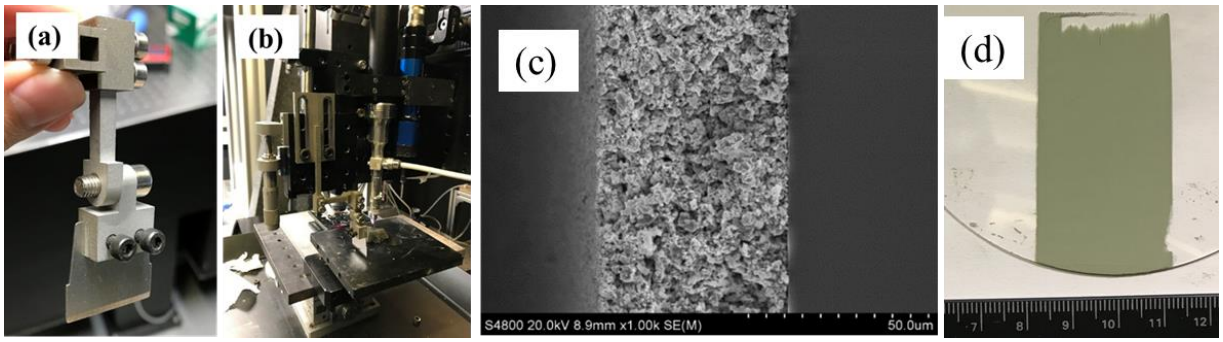

Figure 18. a) The photo of the doctor blade and (b) the photo of the doctor blade setup on our 3D printing platform, (c) SEM image of the cross-section of the green film and (d) the top view of the green film with an area of 12cm^2.

Cold spray coating. The cold spray coating of the electrolyte green films for achieving a thin electrolyte membrane in sintered half cells was developed. Four different binders (HPMC, WSR-301, WSR-750, and PVA) were applied to prepare the BCZYYb electrolyte precursor slurries for spray coating. The photos of the surface of the spray-coated electrolyte green films are presented in **Figure 19.** The electrolyte films with HPMC and WSR-301 as binders (top photos) are rough and show many cracks after drying. When the PVA and WSR-N750 were used as binders, the spray coating resulted in smooth, crack-free electrolyte green films (bottom photos). The electrolyte film surface with high roughness and cracks resulted in the imperfect co-sintering process since the inhomogeneity of the green films caused irregular shrinkage and stress during laser processing. Thus, the PVA and N750 were chosen as the binder for the preparation of spraying coating slurries. Furthermore, the N750 is a kind of POLYOX Water-Soluble Resins that has high-binding efficiency for pigments, fillers, metal powders, and ceramics. These binders easily burn off at low temperatures with little or no tendency to char. The slurry with N750 as the binder for spray coating of a thin electrolyte layer has been extensively used. **Figure 20** provides the SEM images of the green half cells comprised of a 3D printed H_2 electrode precursor layer and spray-coated electrolyte precursor green layer. The cross-section (left image in **Figure 20**) shows a homogenous thin electrolyte precursor green layer with a thickness of around 30μm, which will be thinner than 10μm after laser sintering and achieve the target area-specific resistance of the electrolyte. The surface (right image in **Figure 20**) shows that the spray coating can introduce a very homogenous and smooth electrolyte precursor green film, making the subsequent laser sintering reactively easy. In summary, cold spray coating is an effective technique to introduce thin layers for manufacturing PCES.

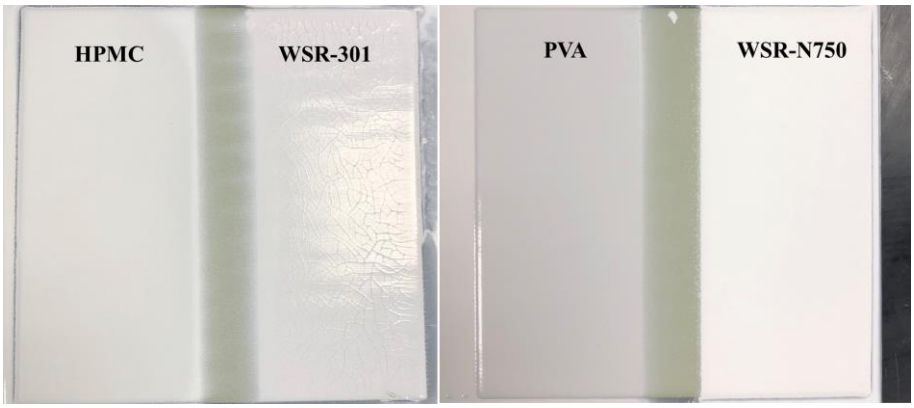

Figure 19. Photos of BCZYYb precursor green films prepared by cold spraying method with HPMC, WSR-301, WSR-750, and PVA as binders.

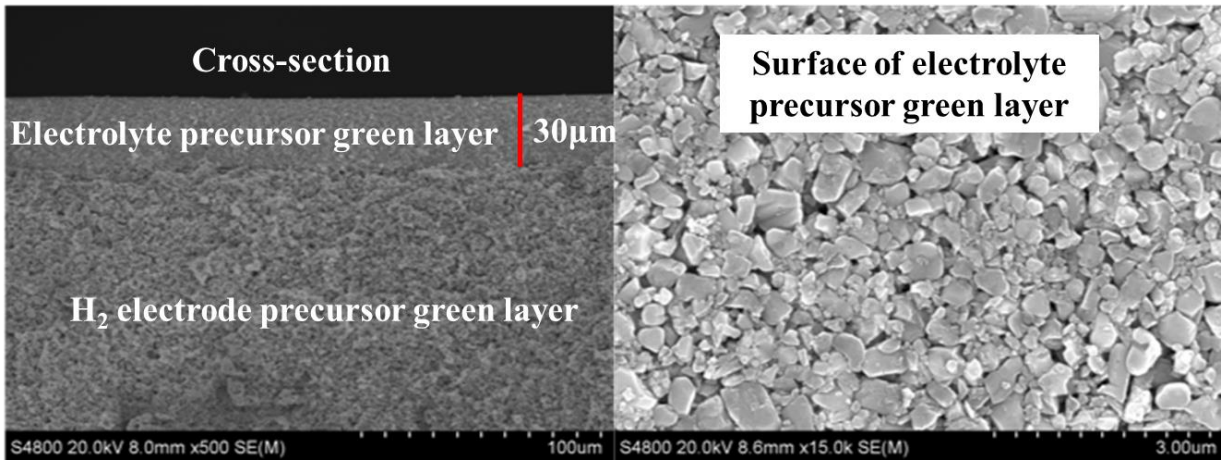

Figure 20. SEM images of the half cells comprised of 3D printed H_2 electrode precursor green layer and spray-coated electrolyte precursor green layer.

Milestone 2.2 Based on ST-2.2 RLRS of Component Thin Films

Milestone 2.2 is based on ST-2.2 RLRS of Component Thin Films. The crack-free PCES component films with an area >6 cm^2 and thickness of 5-200 μm will be manufactured by L3DP. The electrolyte (pinhole-free), O_2 electrode (highly porous), and H_2 electrode (highly porous) films with ASRs <0.1 $\Omega \cdot cm^2$, and interconnect with ASR <0.01 $\Omega \cdot cm^2$ should be obtained at 600 ^oC. Based on the following detailed results and discussion, we estimate that this milestone has been finished about 100%.

1) The RLRS was invented by Clemson, and the patent was filed, which could fabricate electrolytes, electrodes, interconnects, and membranes with the desired crystal structure and microstructures.

Green pastes were prepared by ball milling of their raw oxide and carbonate powders (i.e., $BaCO_3$, Fe_2O_3, CeO_2, ZrO_2, La_2O_3, Cr_2O_3, $SrCO_3$, NiO, Y_2O_3 and Yb_2O_3) for 48 h in the stoichiometric ratio and followed by mixing of the ball-milled powder with water, dispersant, and binder as described in previous section. The pastes were fed by compressed air from a conventional plastic syringe the substrate through the microextruder with a needle (0.5 mm diameter). To the dried green films, the carbon dioxide laser was irradiated for the reactive sintering. The laser was

scanned once across the films by placing them on an X-Y stage. RLRS could prepare dense electrolytes, porous electrodes, and dense interconnects. Dense BZY20 and BCZYYb electrolytes, porous NiO-BCZYYb and BCFZY0.1 electrodes, porous BCZY63 electrode scaffold, dense LSCr interconnect, and dense $BaCe_{0.85}Fe_{0.15}O_{3-\delta}$-$BaCe_{0.15}Fe_{0.85}O_{3-d}$ (BCF8515–BCF1585) mixed protonic and electronic conducting membranes were prepared by RLRS using a CO_2 laser. The crystal structures of the 12 protonic ceramic compounds/composite are summarized in **Figure 21**, which clearly shows that the desired crystal structures were successfully achieved for each ceramic part.

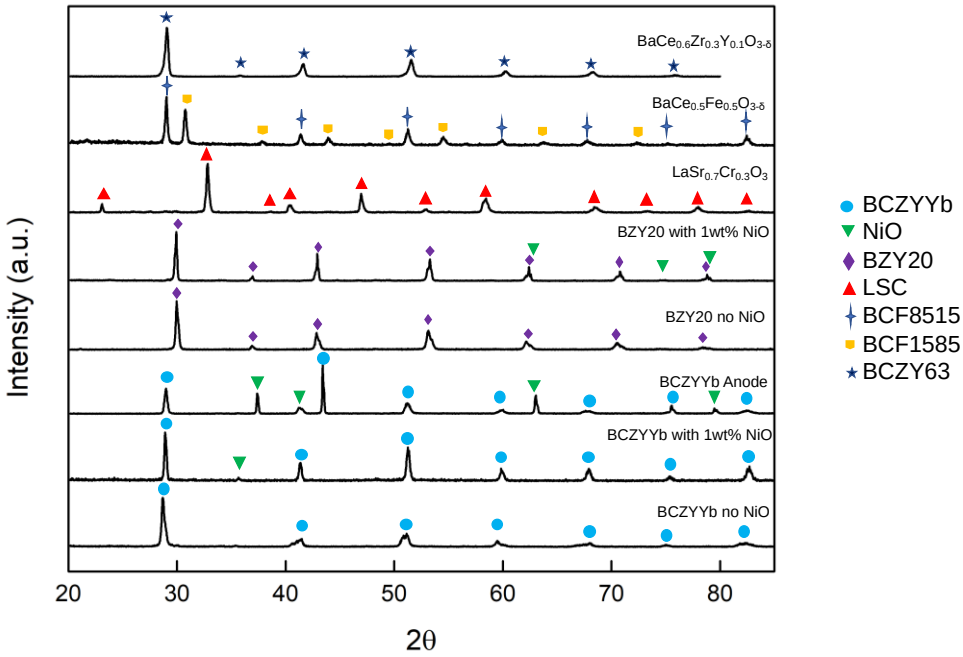

Figure 21. XRD patterns of RLRS-derived ceramics for proton-conducting energy devices.

2) The fully densified BCZYYb+1wt%NiO electrolyte films with controllable thickness were prepared by the RLRS method either in the half cell and single-cell configurations. The defect-free electrolyte films can be as thin as 9 μm. The crack-free electrolyte film on the porous hydrogen electrode with a unit area greater than 6 cm^2 can be prepared by RLRS with high reproductivity. A summarized area of ~120 cm^2 was obtained. The ASR of the electrolyte membrane measured in the single-cell configuration under open-circuit conditions can reach a value of ~0.08 $\Omega \cdot cm^2$, which is better than the milestone metric of 0.1 $\Omega \cdot cm^2$.

The 40wt%BCZYYb + 60wt%NiO hydrogen electrode precursor layers were usually prepared by the microextrusion-based 3D printing in doggy-bone geometries (**Figure 22a**). The BCZYYb+1wt%NiO electrolyte precursor layers were either deposited using the same microextrusion-based 3D printing (for thick electrolyte membrane, **Figure 22b**) or by cold spray coating-based 3D printing (for thin electrolyte membrane, **Figure 22c**).

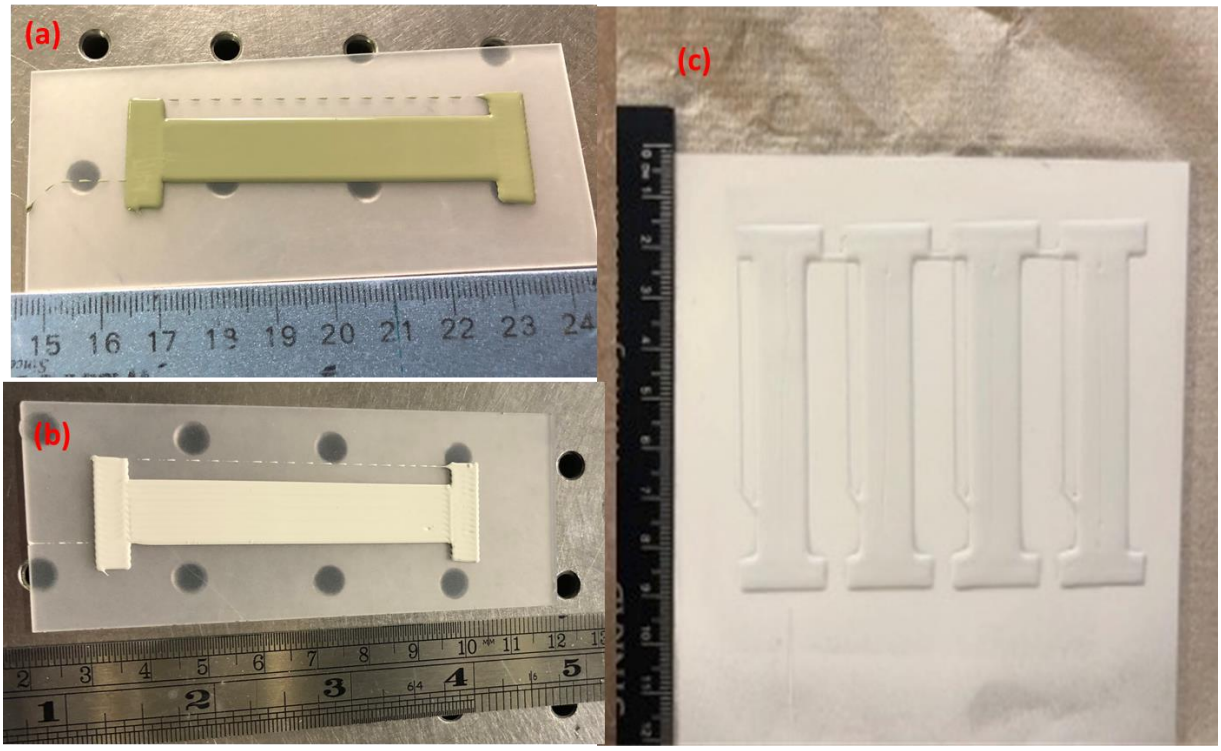

Figure 22. Photos of 3D printed green hydrogen electrode precursor layer (a), half cells with electrolyte layers deposited by microextrusion (b), and half cells with electrolyte layers deposited by cold spray coating (c).

The CO_2 laser with a maximum power of 100 W was used to scan the green hall-cells with a controlled scan feed and power. **Figure 23** provides a summarized photo of 13 half cells with a unit area around 10 cm^2, which has a total area of ~120 cm^2. It is clear there are no apparent cracks that can be found for these half cells, which successfully met the milestone metrics with electrolyte or hydrogen electrode larger than 6cm^2.

It is well-known that the laser power has a significant effect on the RLRS results. In the current study, the laser power density was optimized by adjusting the laser power percentage and lase scanning speed simultaneously. **Figure 24** shows the SEM results of the half cells obtained by RLRS of half cells with thicknesses close to 100@230 on 3mm unpolished fused silica. The increase of defocus distance has a significant effect on the microstructure. The shortest defocus distance resulted in a fully densified electrolyte film with a thickness of 16 μm. The increase of defocus distance to two times (10 mm), some pores are observable on the surface, although the power percentage increased 15% percent. The thickness of the electrolyte didn't change obviously. When the defocus distance further increased to 15 mm, many pores can be found on the electrolyte film surface, and the electrolyte thickness decreased to 9 μm. The laser power is mainly determined by defocusing distance and power input, which can be used to control the relative density and the electrolyte thickness.

Figure 23. Summary optical photo of half cells fabricated by L3DP.

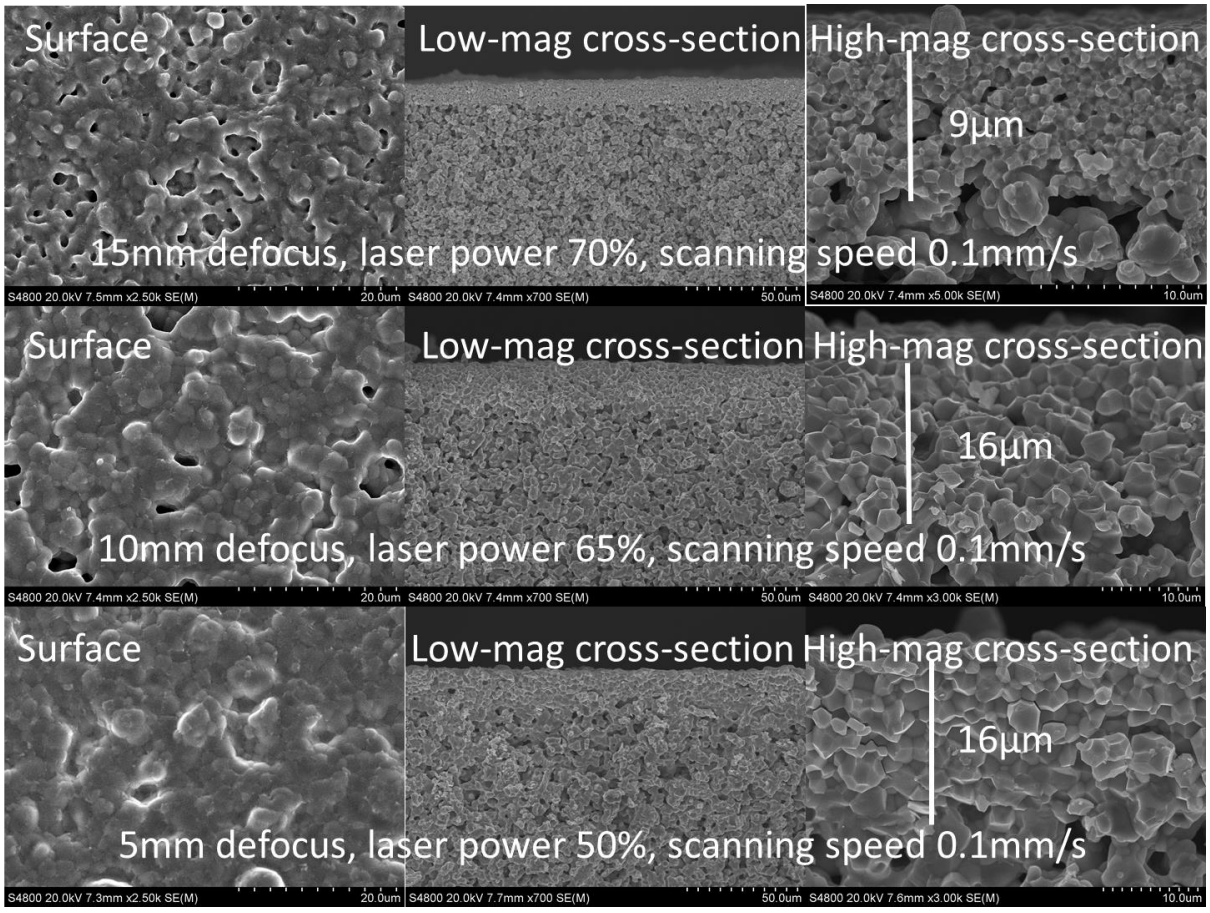

Figure 24. Laser power density effect on the microstructure the half cells obtained by RLRS.

The single cells were fabricated by further coating the half cells fabricated by RLRS with BCFZY0.1 oxygen electrode thin film followed by 900 ^{o}C treatment. The several single cells with electrolyte film thickness around 20 μm were fabricated, as shown in **Figure 25**. The electrolyte layer is fully densified and the grain boundary is not clear, which means that the grain boundary for the electrolyte prepared by RLRS should have less resistance caused by the grain boundary. The EIS measurement result under open circuit condition was measured to obtain the ASR of electrolyte thin film. **Figure 26** indicates that the ohmic ASR for the BCZZYYb thick film with a

thickness of around 18 μm is about 0.14 Ω·cm^2 at 600 °C. The proton conductivity as high as 1.29x10^{-2} Ω^{-1}·cm^{-1} was obtained at 600 °C under fuel cell operating mode. Considering the easily achievable thickness of 10μm by RLRS method, the ohmic ASR of our BCZYYb electrolyte fabricated by RLRS can reach to 0.08 Ω·cm^2 at 600 °C, which is much better the milestone metric **(0.10 Ω·cm^2)**.

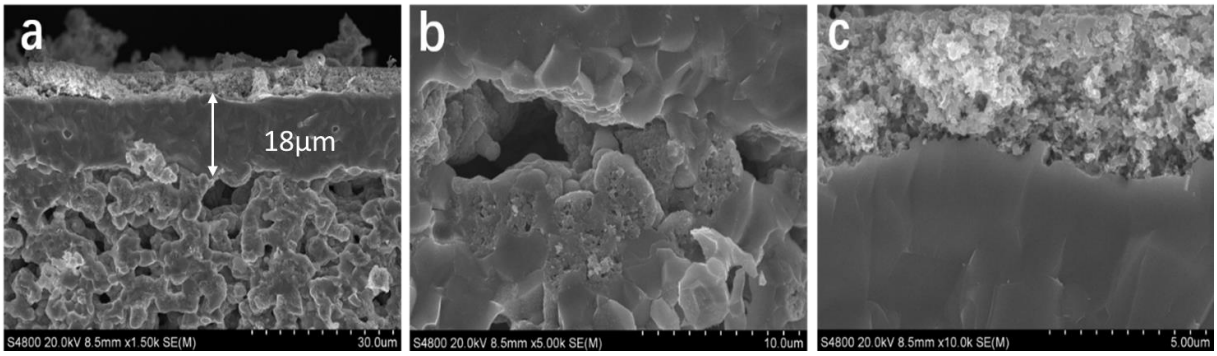

Figure 25. SEM images of single cells: the entire cross-section (a), interface of anode/electrolyte(b) and cathode layer (c).

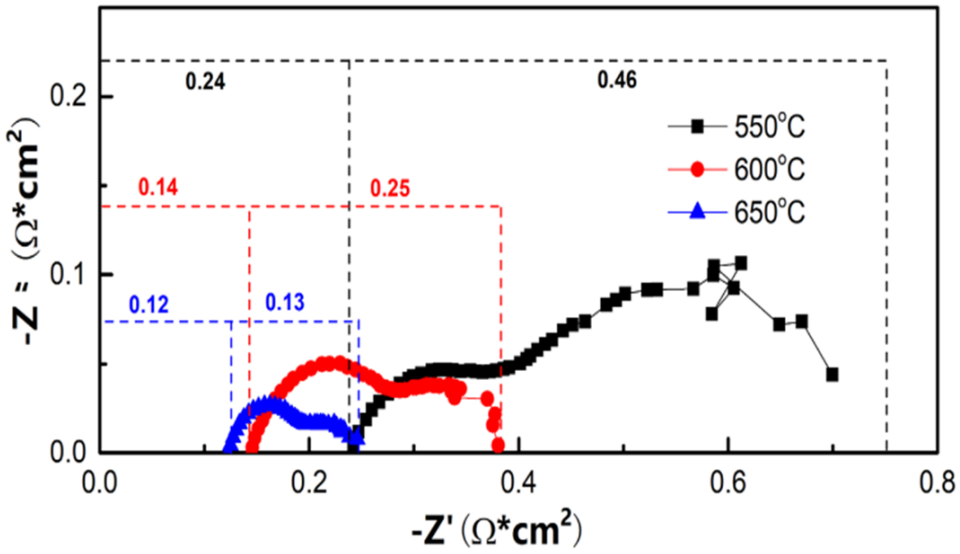

Figure 26. Electrochemical impedance measurement of single cells under open-circuit conditions while applying Air/H_2 gradient.

3) The porous hydrogen electrodes with a unit active area of >6cm^2 (summary area >120cm^2) and desired crystal structure and microstructure were obtained RLRS, which met the milestone metric of 6cm^2. The hydrogen electrodes prepared by RLRS in several single cells showed ASR values around 0.0744Ω·cm^2 at 600°C, which well met the milestone metric of 0.10Ω·cm^2.

Figure 27 provides the EIS measurement result for single cells based on a porous hydrogen electrode fabricated by the RLRS method. The total electrode polarization ARSs the for single cells are 0.25 Ω·cm^2 and 0.14 Ω·cm^2 at 600 °C. The further EIS analysis proved that the hydrogen

electrode polarization ASRs are 11 Ω·cm^2 and 0.0744 Ω·cm^2, which well met our milestone metric of 0.1 Ω·cm^2.

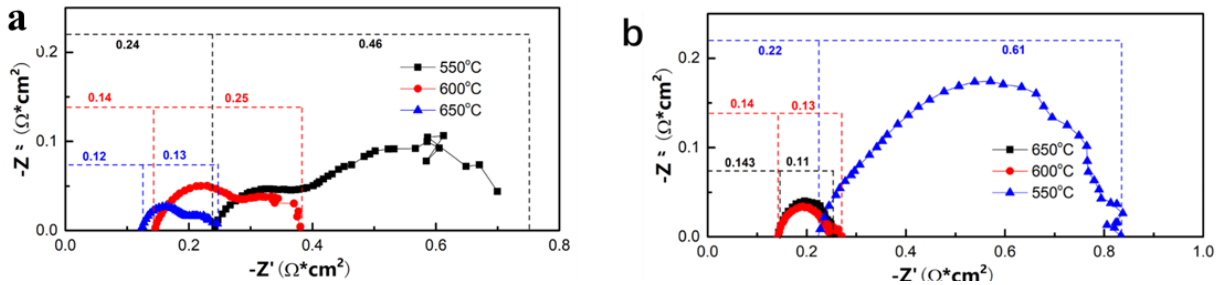

Figure 27. EIS measurement of two single cells with 40wt%BCZYYb+60wt%NiO hydrogen electrode prepared by RLRS.

4) The porous oxygen electrode scaffold of BCZY63 with a unit area around 6 cm^2 was successfully prepared by RLRS in the single-cell configuration by sintering the three layers (electrolyte, hydrogen electrode, and oxygen electrode cathode) through one laser scan. The oxygen electrode scaffold of BCZY63 after infiltrating with BCFZY0.1 showed excellent polarization resistance performance. The ASR of 0.1 Ω·cm^2 was achieved at 600^o C, which well met our milestone metric (0.1 Ω·cm^2).

The anode precursor powder paste was 3D printed onto a substrate (fusion silica) with a thickness of 300 μm. Then the electrolyte precursor powder slurry was deposited onto the green anode by spray coating with ~30μm thickness, and then the scaffold precursor powder slurry was deposited onto the electrolyte layer by spray coating with ~100 μm thickness. Then the CO_2 laser (Firestar v20, SYNRAD, Inc., WA, USA, wavelength 10.6 μm) with a cylindrical lens-forming a line shape laser spot was applied to the 3-layer cell for sintering. The laser operation scan speed was 0.1mm/s, and power density was 85W, defocus distance was15mm. The photo of the as-prepared single cells (**Figure 28a**) shows that the single cells prepared by one laser scan don't have any cracks. The total active area around 6 cm^2 was obtained. The SEM images (**Figure 28b-e**) show that one laser scan successfully obtained the dense electrolyte, porous hydrogen electrode, and porous oxygen electrode scaffold. The porous BCZY63 scaffold with an active area of ~6 cm^2 can be obtained by RLRS.

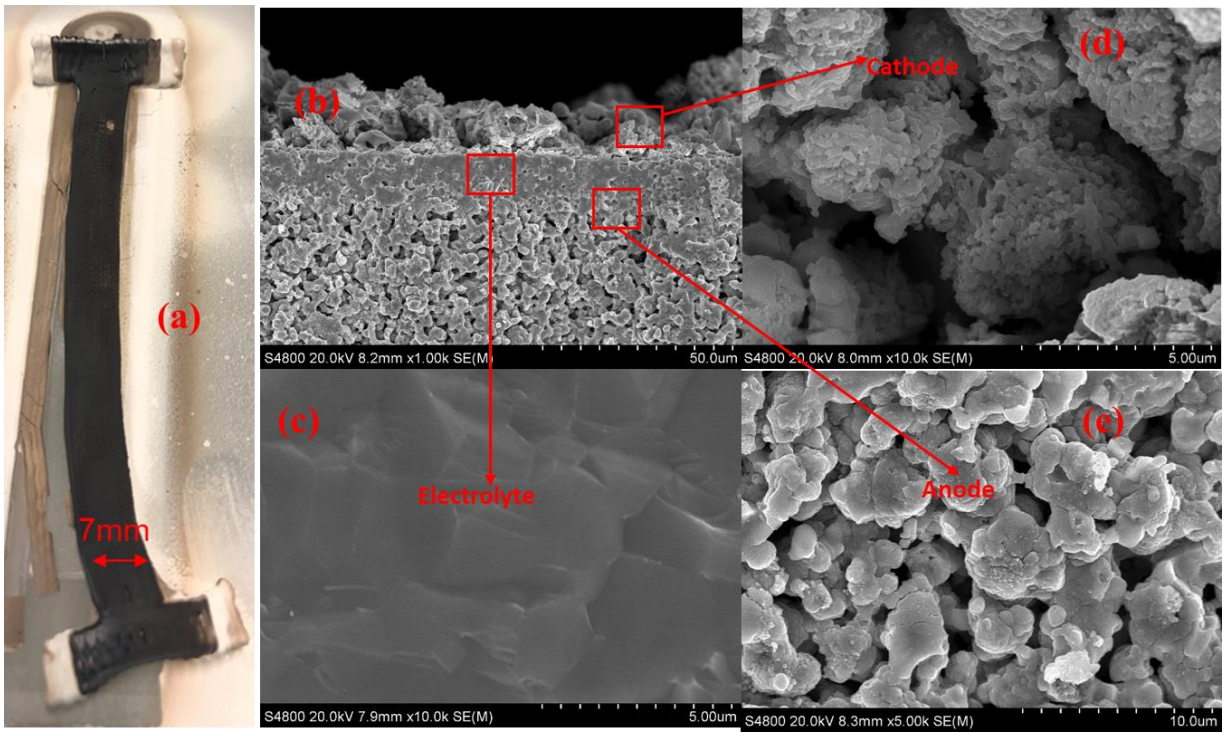

Figure 28. 40wt%BCZYYb+60wt%NiO hydrogen electrode | BCZYYb electrolyte | BCZY63 oxygen electrode scaffold prepared by one laser scan. (a) optical photo, and SEM images of (b) 3-layer cross-section, (c) electrolyte, (d) oxygen electrode scaffold, and (e) hydrogen electrode.

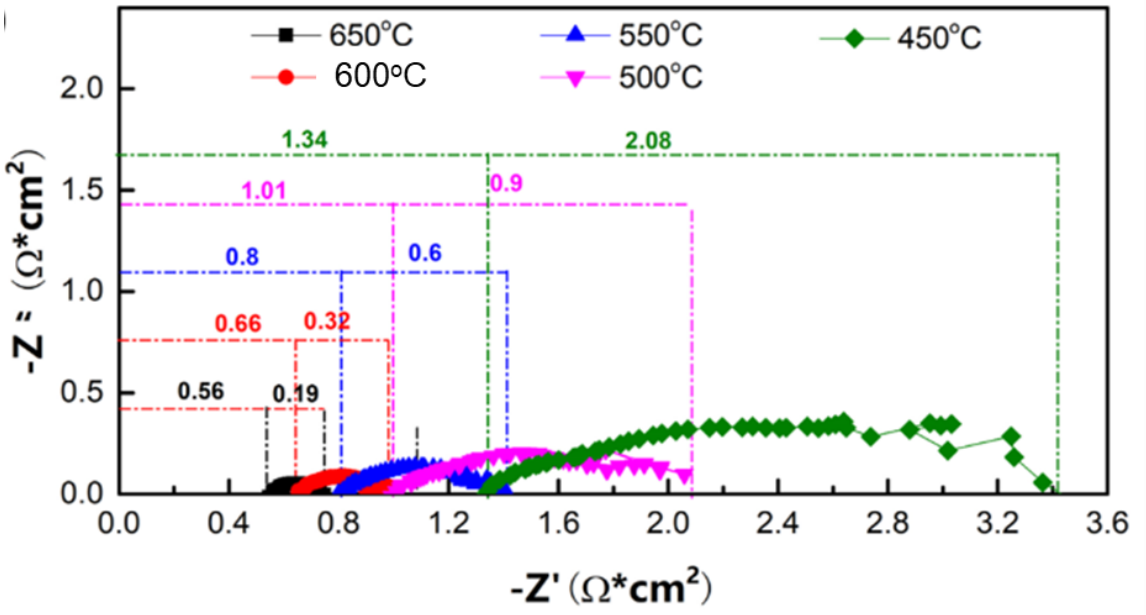

Figure 29. EIS measurement of single cells fabricated by one-step laser scanning.

After infiltrating with the BCFZY0.1 nanoparticle into the BCZY63 scaffold, the single cells were measured for estimating the polarization resistance of the composite oxygen electrode BCZY63+BCFZY0.1. The EIS measurement results (**Figure 29**) indicate that total electrode

polarization ASR is around 0.32 $\Omega \cdot cm^2$. The further EIS analysis separated the hydrogen electrode and oxygen electrode successfully, which turned out that the ASR for oxygen electrode polarization is around 0.1 $\Omega \cdot cm^2$ at 600 ^oC. Our milestone metric of 0.1 $\Omega \cdot cm^2$ was successfully reached.

5) The fully densified phase-pure LSCr interconnect film with thickness as thin as 10 μm and active area as large as 7 cm^2 were successfully prepared by RLRS on fused silica or MgO substrate. The ASR measurement showed a value of around 0.001 $\Omega \cdot cm^2$ was obtained at 600 °C, which is much better than our milestone metric (0.01 $\Omega \cdot cm^2$).

The raw materials of La_2O_3, Cr_2O_3/Cr, and $SrCO_3$ were prepared into a printable paste, printed into green films, and sintered by RLRS following the similar procedure for the preparation of electrolytes, electrodes, half-cells and single cells except for the detailed adjustment of laser paste composition and laser operating parameters. **Figure 21** showed that the phase-pure LSCr interconnect film was obtained. **Figure 30a** provides the optical photo of an LSCr interconnect film deposited on fused silica substrate by RLRL, which clearly indicates that the crack-free LSCr interconnect thin film with an active area of >7cm^2 was obtained. **Figure 30b**, the SEM image of the LSCr interconnect film fabricated by RLRS, shows that the refractory LSCr was fully densified by RLRS and the thickness as thin as 10μm was obtained. For comparison, the LSCr pellet obtained by conventional solid-state sintering at 1550^{o}C for 10h only can get a relative density of around 80% (**Figure 30c**).

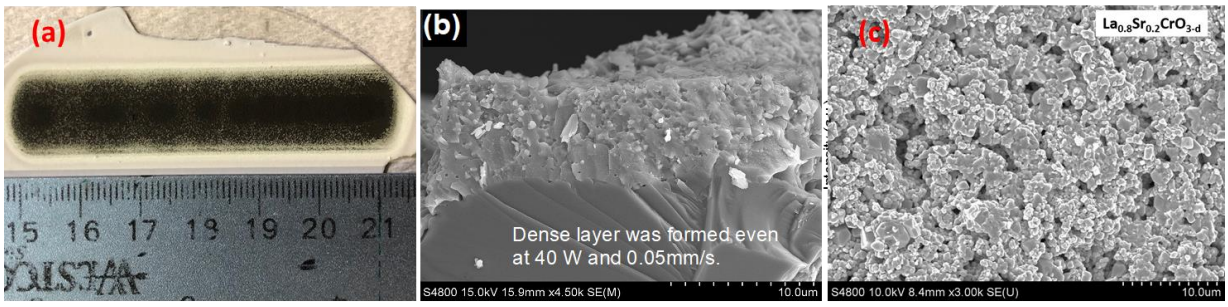

Figure 30. (a) optical photo of LSCr interconnect prepared by RLRS, **(b)** SEM image of the cross-section of LSCr thin film on MgO substrate prepared by RLRS, and (c) SEM image of the top view of LSCr pellets obtained by solid state sintering at 1550^{o}C for 10h.

Then, their electronic conductivity of LSCr thin films was examined in the stagnant air at different temperatures. **Figure 31a** shows an Arrhenius plot with the values of the reported data derived by furnace-sintered samples. They show the explicit negative linear relationship, which suggests that the conduction is owing to a thermally activated hopping mechanism. As shown in **Figure 31(b)**, the conductivity of the samples prepared at 103 W and 0.10 mm/s, and 103 W and 0.08 mm/s were relatively higher than those of the other three samples. This is reasonable because they contain no intermediate phases and show a relatively high packing density. When the conductivity of the high-packing-density-samples is compared to that of furnace-sintered $La_{0.8}Sr_{0.2}CrO_{3-d}$, it is lower than those fired more than twice (relative density of ~95%, however, comparable to those using nitrate-derived precursors (relative density >85%. This conductivity corresponds to area-specific resistance of ~0.001 $\Omega \cdot cm^2$ at 600 °C, as shown in **Figure 31c**, suggesting that the RLRS-derived $La_{0.7}Sr_{0.3}CrO_{3-\delta}$ interconnect can be used in the PCES.

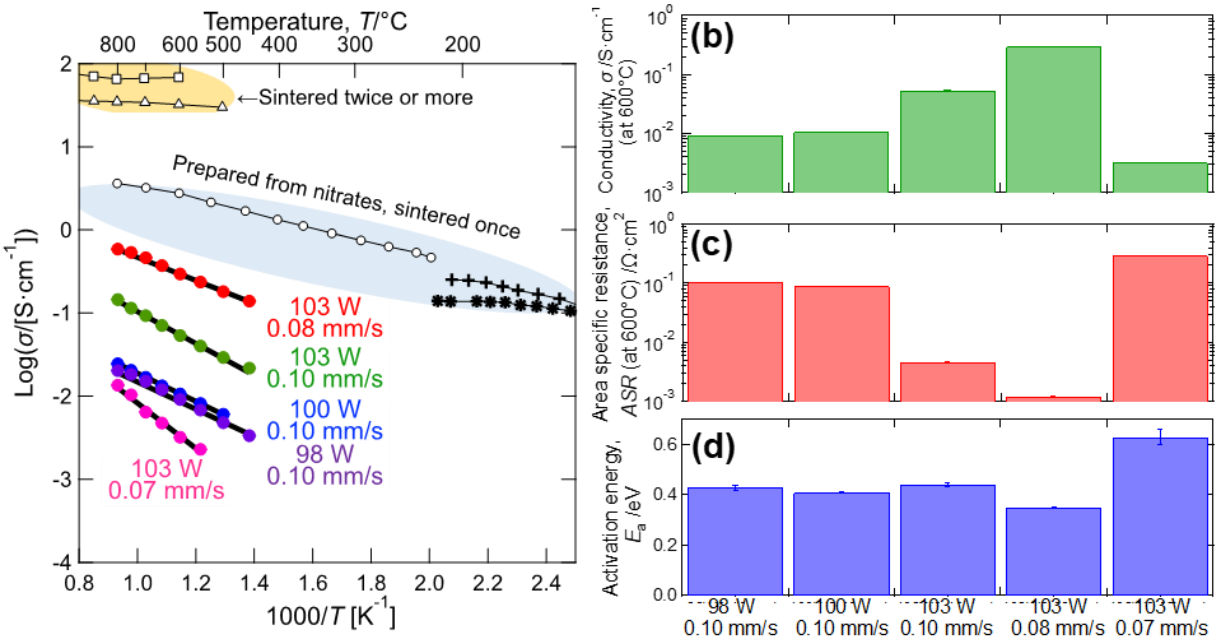

Figure 31. (a) Arrhenius plots of conductivity of $La_{0.8}Sr_{0.2}CrO_{3-\delta}$ films compared to literature, and laser-conditions dependences of (b) conductivity at 600°C (c) ASR at 600°C, and (d) activation energy.

Task-3 PCES Single Cells by L3DP

Milestone 3.1 Based on ST-3.1 Binding of PCES Component Films

Milestone 3.1 is based on ST-3.1 Binding of PCES Component Films. Efficient binding without apparent interfacial and component performance deterioration will be achieved. Based on the following detailed results and discussion, we estimate that this milestone has been finished about 100%.

1) The binding between the green films of the component layers of hydrogen electrode, electrolyte, oxygen electrode scaffold/oxygen electrode, and interconnect was achieved successfully, which allowed the successful sintering of the layers together to make half cells and single cells, etc. Figure 32 provided some representative SEM images of some interfaces prepared by microextrusion or spray coating. **Figure 32a** proved that the homogeneous green BCZYYb+1wt% electrolyte precursor layer well adhered to the green 40wt%BCZYYb + 60wt%NiO green layers by microextrusion based 3D printing. **Figure 32b** proved that the three layers of the BCFZY0.1 oxygen electrode precursor film, the BCZYYb+1wt% electrolyte precursor film, and the 40wt%BCZYYb+60wt%NiO precursor film were well bonded together after microextrusion-based 3D printing. **Figure 32c** proved that the BCZY63 oxygen electrode scaffold could directly bond to the very smooth fused silicon substrate after microextrusion-based 3D printing. **Figure 32d** proved the three years of three layers of the BCZY63 oxygen electrode precursor film, the BCZYYb+1wt% electrolyte precursor film, and the 40wt%BCZYYb + 60wt%NiO precursor film were well bonded together while both the oxygen electrode scaffold and electrolyte films were introduced by spray coating. The hydrogen electrode was introduced by microextrusion.

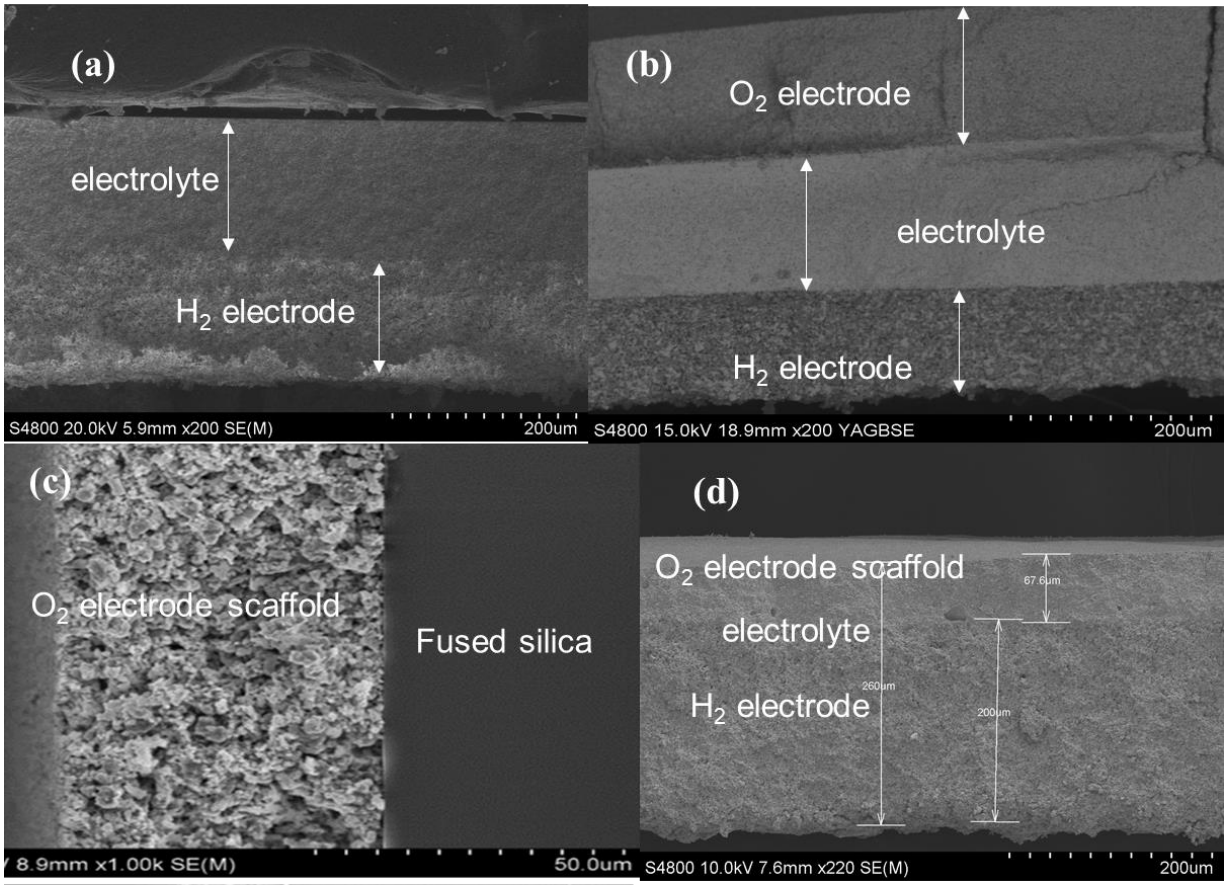

Figure 32. SEM images of 3D printed thin films, half cells, and single cells by microextrusion or coating sintering. (a) electrolyte on hydrogen electrode half cell by microextrusion, (b) oxygen electrode, electrolyte, and hydrogen electrode single cells by microextrusion method, (c) oxygen electrode scaffold thin film on a fused silica substrate, and (d) oxygen electrode scaffold, electrolyte, and H2 electrode single cells by combined spray coating and microextrusion.

2) The binding between the sintered component layers hydrogen electrode, electrolyte, oxygen electrode scaffold/oxygen electrode, and interconnect was also achieved successfully. There was no visible electrochemical performance degradation. Figure 33 provides some representative SEM images of the interfaces prepared by 3D printing after RLRS. **Figure 33a** proved that the BCFZY0.1 oxygen electrode thin film adhered to the top the electrolyte layer of the half cells prepared by RLRS by conventional screen-printing followed by annealing at 900 ^{o}C. **Figuure 33c** proved that the BCZYYb electrolyte layer adhered to the 40wt%BCZYYb + 60wt%NiO hydrogen electrode obtained by SSRS by L3DP. The BCFZY0.1 oxygen electrode could further adhere to the electrolyte membrane top. **Figure 33d** proved that the single-cells comprised of BCZY63 oxygen electrode scaffold, BCZYYb electrolyte, and 40wt%BCZYYb + 60wt%NiO hydrogen electrode prepared by one-step laser scanning were successfully fabricated, which showed excellent bonding at the interfaces of electrolyte/oxygen electrode scaffold and electrolyte and hydrogen electrode. **Figure 33e** proved that the second L3DP could introduce the BCZY63 oxygen electrode scaffold layer after the half-cells (BCZYYb electrode on 40wt%BCZYYb + 60wt%NiO hydrogen electrode) were prepared by L3DP, indicating that we can do layer-by-layer 3D printing by L3DP. **Figure 33f** proved that the BCFZY0.1 oxygen

electrode porous thin film could adhere to BCZYYb electrolyte surface prepared by SSRS after laser sintering. **Figure 33g** proved that the BCZY63 oxygen electrode scaffold porous thin film could well adhere to the BCZYYb electrolyte prepared by SSRS after laser sintering. **Figure 33h** proved that the LSCr interconnect dense film could adhere to the MgO substrate.

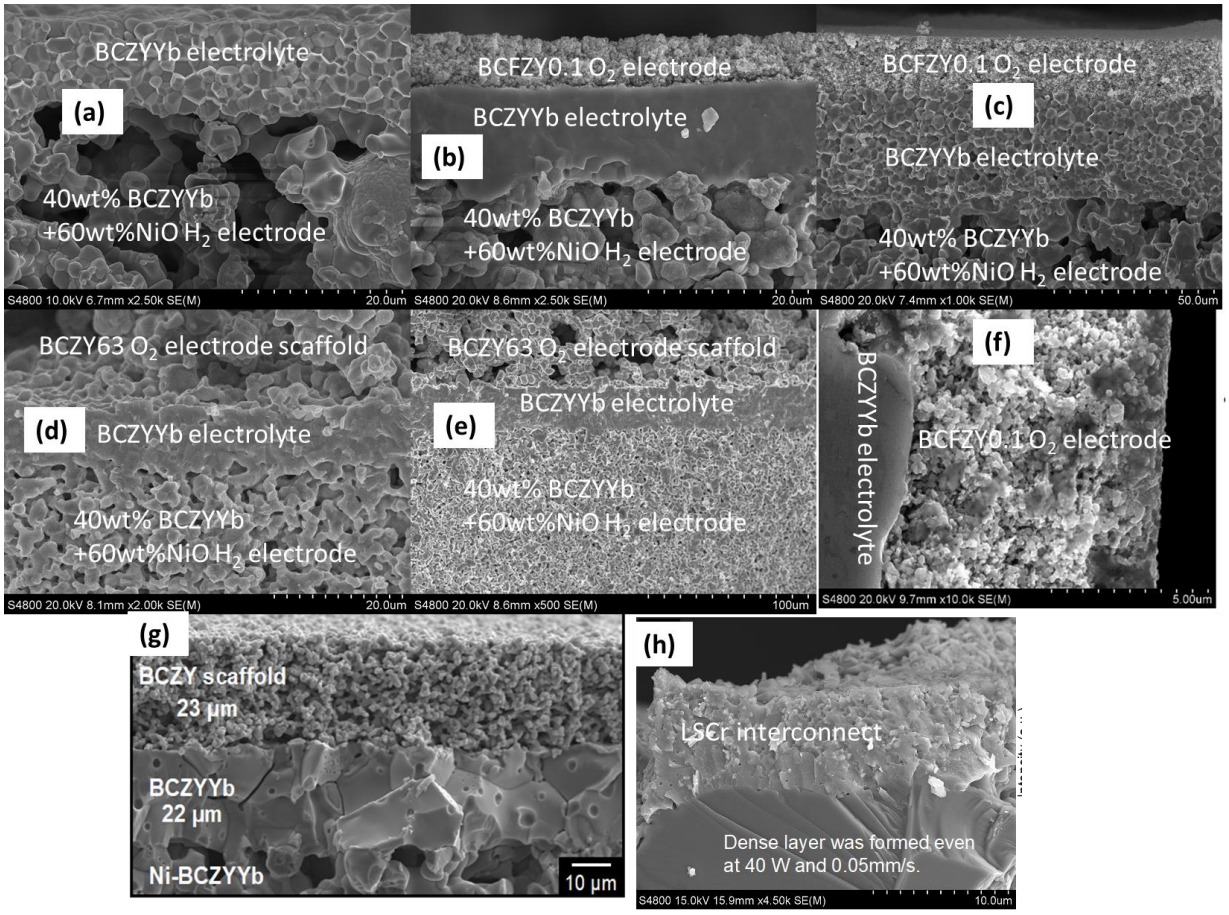

Figure 33. SEM images of the PCES component layers prepared by RLRS. For a detailed explanation, please see the text.

Milestone 3.2 Based on ST-3.2 Infiltration Electrode Nanoparticles

Milestone 3.2 is based on ST-3.2 Infiltration Electrode Nanopoaertilces. The effective infiltration in the electrodes obtained by L3DP showing OER and HER ASRs <0.1 $\Omega \cdot cm^2$ at 600 ^oC should be achieved. We studied the infiltration of BCFZY0.1 nanoparticle in the laser-sintered BCZY63 O_2 electrode scaffold. Based on the following detailed results and discussion, we estimate the progress of Milestone is 100%.

The BCFZY0.1 precursor ink was infiltrated into the BCZY63 O_2 electrode scaffold prepared by RLRS. BCFZY precursor ink was prepared by mixing 0.01 mol (in total, respected to BCFZY) of a stoichiometric amount of the respective metal nitrates, 0.015 mol of monohydrate citric acid, and 9 g DI water. 7μL of 28 wt%$NH_3 \cdot H_2O$ was added to improve their solubility. Infiltration, drying by vacuuming, and firing at 400 °C for 1h were repeated several times with individual infiltration amount less than 0.12 $\mu L/mm^2$ for each time. After the final infiltration, the samples were calcined at 900 °C for 1 h (2°C/min). The SEM images (**Figure 34a**) suggests that the calcination at 900 °C for 1 h did not result in a dense layer on the surface. Its EDS mapping result

(**Figure 34b**) indicates that the infiltration of 20μL BCFZY precursor ink each time was sufficient to form a uniform distribution of BCFZY nanocrystals. The high-magnification images (**Figure 34c** and **34d**) show that the nanocrystals (smaller than 50nm) can be extensively observed, which may be ascribed to the BCFZY nanoparticles. The polarization resistance measurement for the infiltrated BCZY63 + BCFZY0.1 composite oxygen electrode indicates that the ASR of the composite oxygen electrode reached the milestone metric of 0.1 $\Omega \cdot cm^2$ at 600 ^oC, which proved that the infiltration was successful.

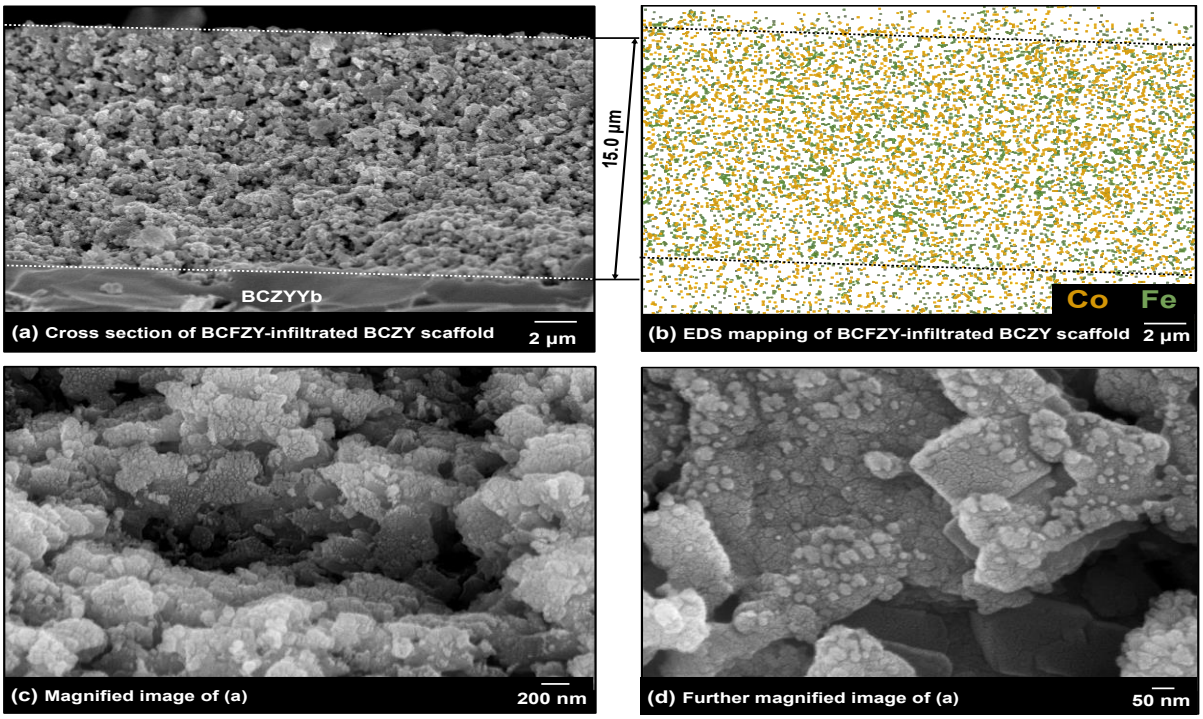

Figure 34. (a) Cross-sectional SEM image of the 7-times-BCFZY-infiltrated BCZY scaffold calcined at 900 °C for 1 h, (b) EDS mapping image, and (c) and (d) are high magnification images of (a).

Milestone 3.3 Based on ST-3.3 Single Cells Manufacturing and Performance/Stability Test

Milestone 3.3 is based on the ST-3.3 Single Cells Manufacturing and Performance/Stability Test. The PCES single cells with area >5 cm^2, current density >500 mA/cm^2 at 1.3 V, and stable operation with degradation rate < 1% for >200 h at 600 ^oC will be successfully manufactured by L3DP. Based on the following detailed results and discussion, we estimate the progress of Milestone is 100%.

1) Cell one. Half-cells comprised of 40wt% BCZYYb + 60wt% NiO hydrogen electrode and BCZYYb electrolyte were fabricated by the RLRS method. BCFZY0.1 oxygen electrode nanoparticle paste was prepared based on the improved Pechini method, which was brushed on the electrolyte surface of the half-cell as an oxygen electrode. Then the cell was post-treatment at 900 °C for 10 h in the furnace. The silver paste was employed on both hydrogen electrode and oxygen electrode to prepare current collectors. Ag wire was used as the lead for both electrodes.The single cell with an active area of ~0.2 cm^2 was measured in both fuel cells and electrolysis modes.

Figure 35a shows the discharged curves of this single cell. The open-circuit voltages (OCV) of the cell are 1.04V, 1.03V, and 1.01V at 550 °C, 600 °C, and 650 °C, respectively, and the corresponding maximum power densities are 317, 500 and 682 mW/cm^2. This cell was also

operated in the electrolysis mode. Pure Argon sweep gas was fed in the hydrogen electrode side with a flow rate of 30 ml/min and stationary air with 20% steam was feed in the air electrode side with a flow rate of 150 ml/min. The performance was demonstrated in **Figure 35b**. Current density increases with temperature increases. When voltage was 1.3V, the current density was 2.26 A/cm^2, 1.36 A/cm^2, 0.852 A/cm^2, 0.478 A/cm^2, 0.261 A/cm^2, and 0.092 A/ cm^2 at 650 ℃, 600 ℃, 550 ℃, 500 ℃, 450 ℃, and 400 ℃, respectively. It demonstrated much higher performance than the milestone requirements: current density >0.5 A/cm^2 at 1.3 V, 600 ℃.

The stability of this cell was evaluated at 600 ℃ and results are shown in **Figure 36a**. The performance was evaluated with pure Ar fed into the hydrogen electrode, humidified air (20% H_2O) steam, humidified Ar (20% H_2O), humidified 5%O_2+Ar (20% H_2O), humidified 10%O_2+Ar (20% H_2O), humidified 15%O_2+Ar (20% H_2O) and humidified 20%O_2+Ar (20% H_2O) were fed in the air electrode respectively. The flow rates of hydrogen and air electrode were set to be 30 and 150 ml/min, respectively. During 163 h operation, the current density with an applied voltage of 1.3 V was increased from 1.36 to 1.7 A/cm^2. The RLRS sintered electrolyte demonstrated excellent stability during operating time. A different amount of oxygen was fed to the O_2 electrode side, the current density of this cell with an applied voltage of 1.3 V increased from 1.161 to 1.794 A/cm^2 as the oxygen content rose from 5% to 20%. **Figure 36b** shows that the morphology of the single cells is still excellent, which further confirms the stability of this stability.

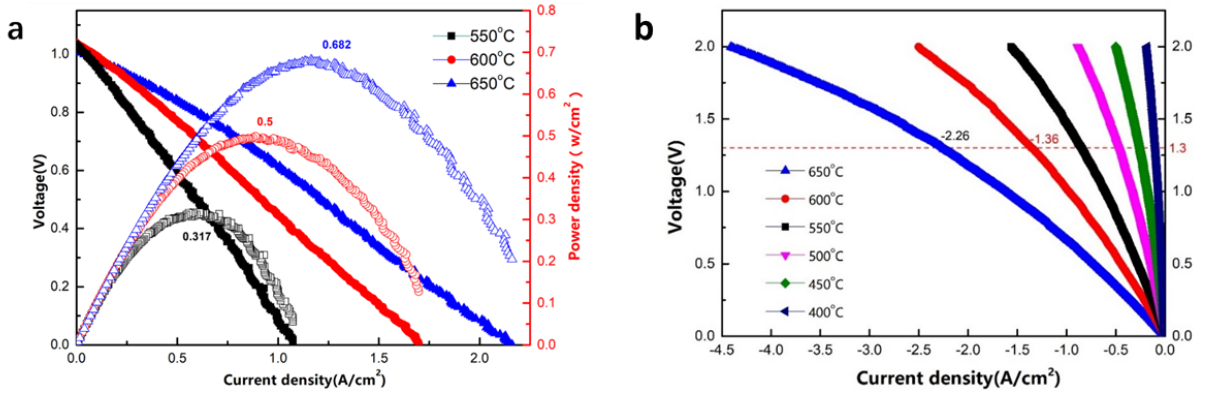

Figure 35. I-V of the single cells at different temperatures (a) fuel cell mode and (b) electrolysis mode.

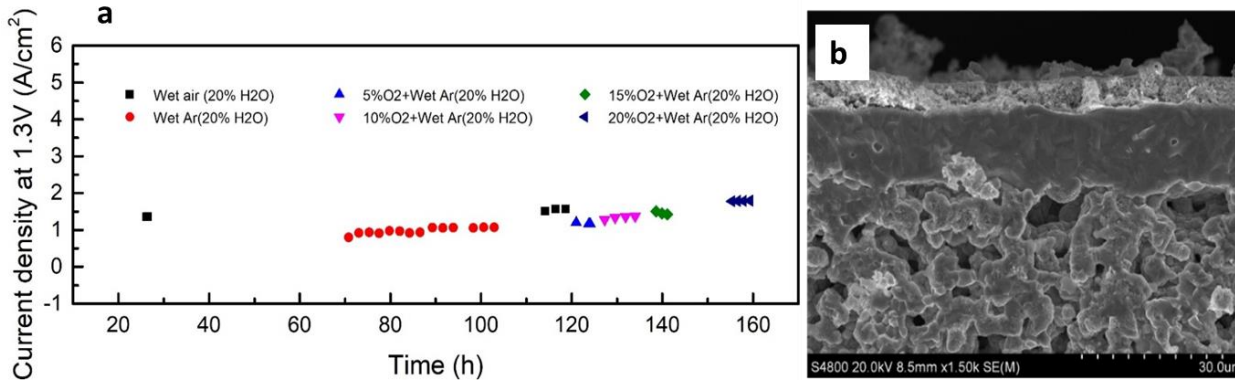

Figure 36. (a) Long-term stability of current density with an applied voltage of 1.3V at 600ºC and (b) SEM image of the single cells after the long-term test.

2) Cell Two. Cell two, with an active area of ~0.29 cm^2, was prepared using the same procedure as the cell one and was evaluated at the same experimental conditions. **Figure 37a**

shows the fuel cell performance of this single cell. The OCVs of the cell are 1.01 V, 1.02 V and 0.99 V at 550 ℃, 600 ℃ and 650 ℃, respectively. The corresponding peak power densities are 305, 605 and 652 mW/cm^2 at 550 ºC, 600 ºC, and 650 ºC, which reach the state-of-the-art PCFC fuel cell performance under Air/H_2 gradient. **Figure 37b** indicates that the morphology of the single cells after testing did not change obviously, which further confirms the stability. This single cell was stopped before the measurement of electrolysis and long-term test because of the sealing leakage.

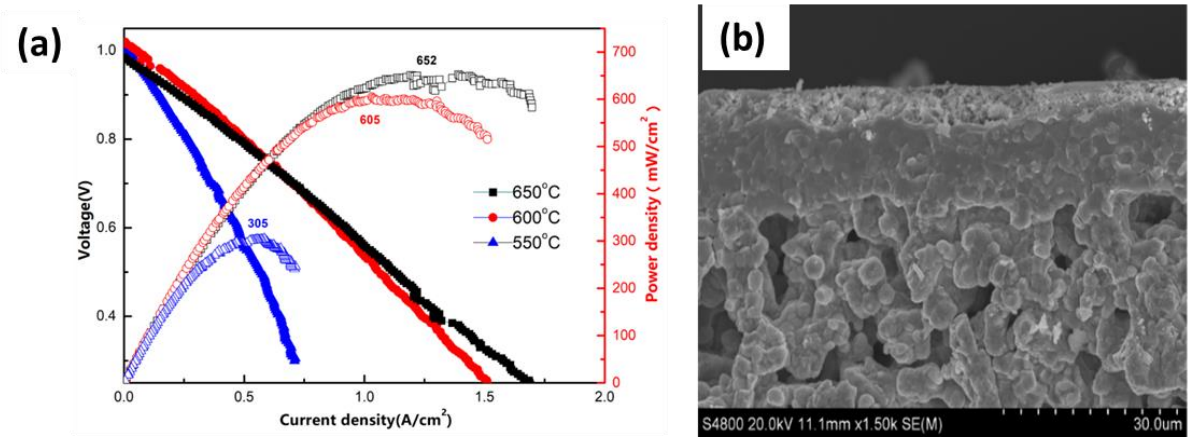

Figure 37. (a) I-V curve of cell 2 operating in fuel cell mode and (b) SEM image of the cross-section of the single cells after testing.

3) Cell Three. Cell three, with an active area of ~0.38 cm^2, was prepared using the same procedure as the previous two cells and was evaluated at the same experimental conditions. **Figure 38a** shows the fuel cell perf ormance of this single cell. The OCVs of the cell are 1.11 V, 1.1 V, 1.09 V, 1.06 V, and 1.03V at 450 ºC, 500 ºC, 550 ℃, 600 ℃ and 650 ℃, respectively. The corresponding peak power densities are 79, 181, 343, 531 and 767 mW/cm^2 at 450 ºC, 500 ºC, 550 ℃, 600 ℃, and 650 ℃, respectively. Although the area increased compared with cell two, the fuel cell performance did not change obviously, indicating that the cell performance was well reproduced since the small cells were prepared by cutting from the large homogeneous cell with a total area of ~10 cm^2. **Figure 38b** indicates that the morphology of the single cells after testing didn't change obviously, which confirmed the stability. This single cell was also stopped before the electrolysis and long-term test because of the sealing leakage.

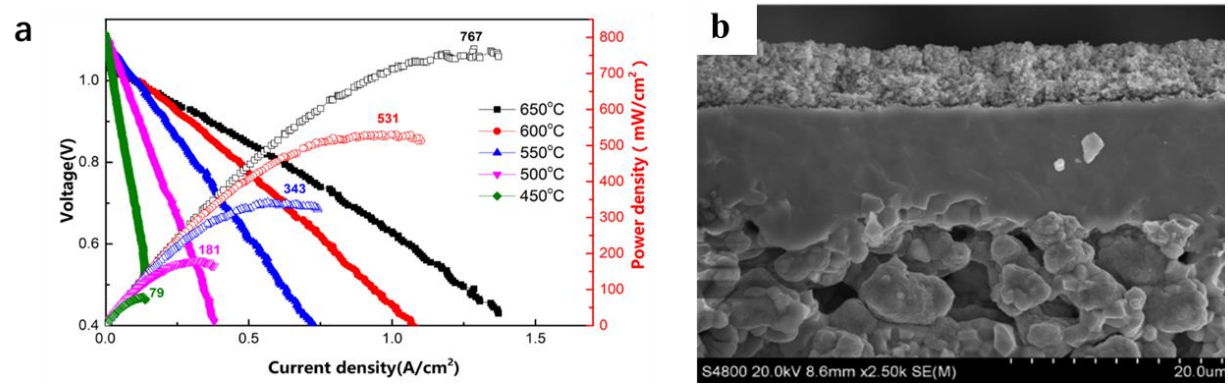

Figure 38. I-V curve of cell 3 operating in fuel cell mode and (b) SEM image of the cross-section of the single cells after testing

4) Cell Four. A single cell comprised of 40wt%BCZYYb + 60wt%NiO hydrogen electrode (microextrusion), BCZYYb electrolyte (spraying coating), and BCZY63 oxygen electrode scaffold was fabricated by the one-step RLRS method. BCFZY0.1 oxygen electrode nanoparticles were introduced by the infiltration method. Then the cell was post-treatment at 900 ℃ for 10 h in the furnace. The silver current collectors were applied on both hydrogen and oxygen electrodes. Ag wire was used as the lead for both electrodes.The single cell (Cell four) with an active area of ~0.52 cm^2 was measured in both fuel cells and electrolysis modes. **Figure 39a** shows the discharged curves of the single cell 4. The OCV of the cell was 1.05 V, 1.04 V, 1.02 V, 1.01 V, and 0.97 V at 500, 550, 600, and 650 ºC, respectively, and the corresponding maximum power densities were 64, 109, 156, 210 and 272 $mW \cdot cm^{-2}$. The performance of cell 4 in the electrolysis mode was shown in **Figure 39b**. Current density increases with temperature increases. When Voltage is 1.3 V, the current density was 0.582 A/ cm^2, 0.43 A/cm^2, 0.297 A/ cm^2, 0.175 A/ cm^2, and 0.098 A/cm^2 at 650 ℃, 600 ℃, 550 ℃, 500 ℃, and 450 ℃, respectively. The stability of cell 4 was evaluated at 600 ℃ and is shown in **Figure 40**. This cell demonstrated excellent stability during 30hrs operation, and the current density with an applied voltage of 1.3 V was increased from 0.414 to 0.446 A/cm^2 without delamination. The three layers of cell structure were kept well even after 60 h of operation.

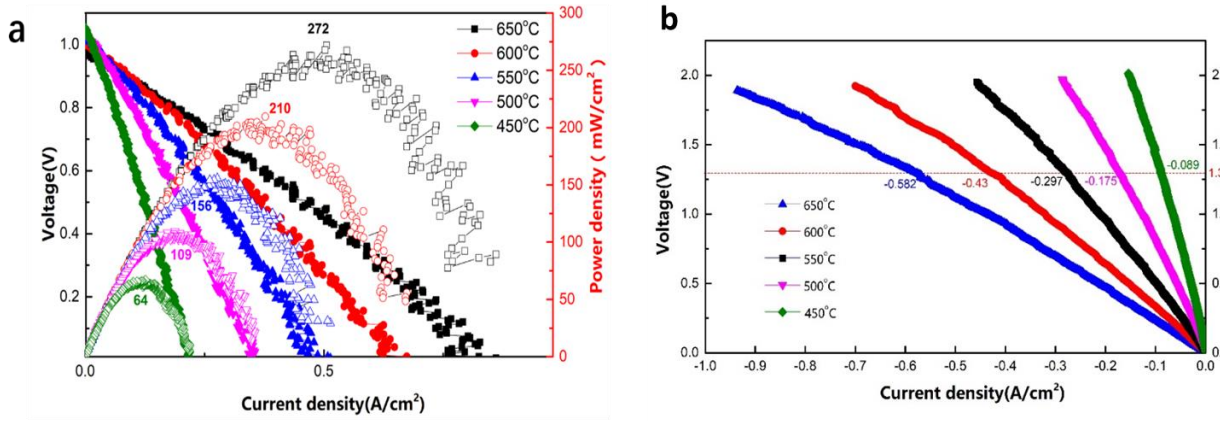

Figure 39. I-V curve of cell 4 at different temperatures (a) fuel cell mode and (b) electrolysis mode.

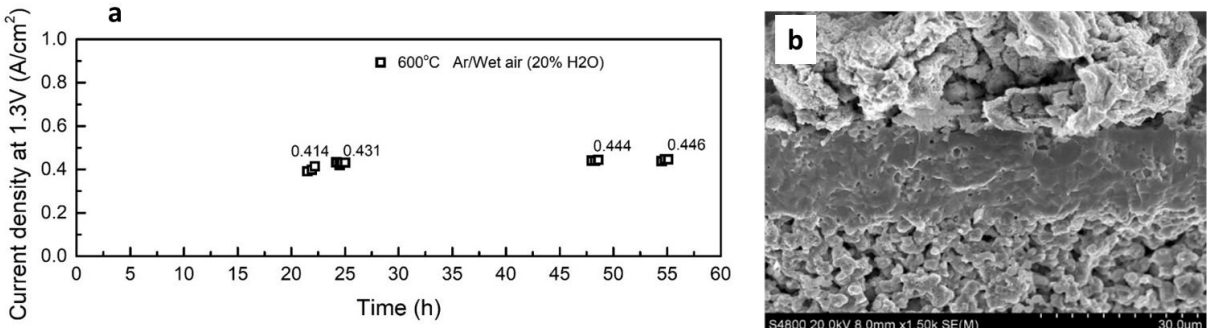

Figure 40. Stability of cell 4. a) Long-term stability of current density with an applied voltage of 1.3V at 600ºC and (b) SEM image of the single cells after the long-term test.

5) We have established a combined single cell with an area of ~6.6 cm^2 (larger than 5 cm^2) by a one-step L3DP method and tested the water electrolysis performance.

The single combined cell was fabricated as follows. The thick hydrogen electrode layer of 40wt% BCZYYb + 60wt%NiO was printed by a microextrusion based method. The thin electrolyte BCZYYb+1wt%NiO was printed by a spray coating-based method. The thin oxygen electrode scaffold of BCZY63 was printed by a spray coating-based method. The single cells comprised of the above three green layers were sintered by rapid laser reactive sintering (RLRS) method using one scan. The rectangular cells with a short side of around 10mm and long-side longer than 10cm was prepared, which was cut into seven pieces and infiltrated with the BCFZY0.1 oxygen electrode active phase. The combined single we prepared and tested is shown in **Figure 41**. Each component cells were sealed with Cerambond and apply an Ag current collector. The seven component cells were combined together to form a composite cell with an active area around 6.6 cm^2. The reason for measuring composite cells is that the L3DP manufactured cells have a small effective thickness, which is too fragile to make large-area un-supported single cells. Therefore, the single combined single cells were measured.

Figure 41. The photo of the combined single-cell prepared by one-step L3DP method. The total area is around 6.6 cm^2.

The single combined cell was tested for achieving long-term electrolysis performance. **Figure 42** indicates that the large-area combined cell was operated for 200 h. The current density increased from 240 mA/cm^2 to 350 mA/cm^2, indicating the excellent stability of this cell. There was a short period when the current density was low, which was confirmed to result from the shortage of steam in the water bubbler. When enough water was supplied, the electrolysis current density recovered immediately. This observation did not affect the stability test. On the contrary, it further proved t combined single cell is stable. Therefore, we demonstrated the large-area single with an active area >5 cm^2 and long-term stability of 200 h.

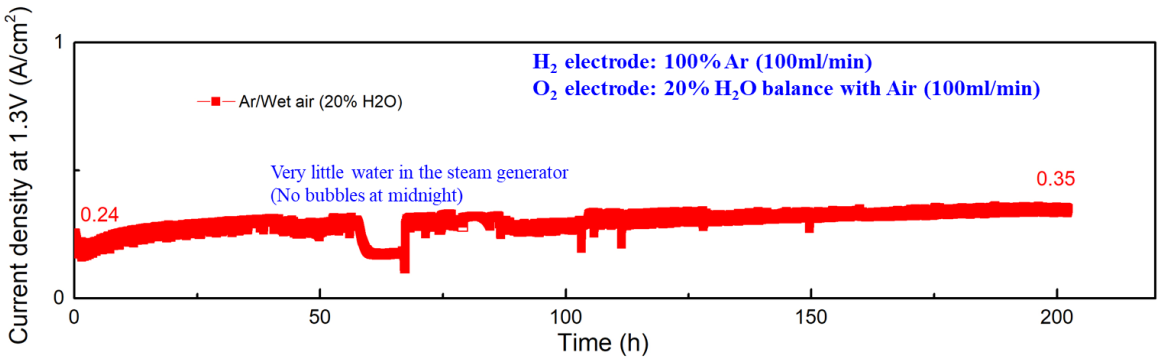

Figure 42. Long-term stability test of a large-area (~6.6 cm^2) combined single cells prepared by a one-step L3DP method followed by infiltration.

Milestone 3.4 Based on ST-3.4 Back-of-the-Envelope Calculation

Milestone 3.4 is based on the ST-3.4 Back-of-the-Envelope Calculation. The quick back-of-the-envelope will show that L3DP technology has the potential to offer the lower price for manufacturing solid oxide electrolyzer stack than the conventional technologies. Based on the following detailed results and discussion, we estimate that this milestone has been finished about 100%.

1) Comparison of materials cost. The fabrication schematic of PCES by Laser 3D printing (L3DP) is shown in **Figure 43a**. The anode, electrolyte, and cathode layer thickness of the cell fabricated by the L3DP method are 250, 10 and 20μm, respectively. The schematic of the traditional electrolyte-electrode assembly (EEA)[1,2] cell is shown in **Figure 43b**. The thickness of the anode functional layer, anode/electrolyte interlayer, the electrolyte layer, cathode/electrolyte interlayer, cathode functional layer is 700, 10, 10, 10, 50 μm, respectively.

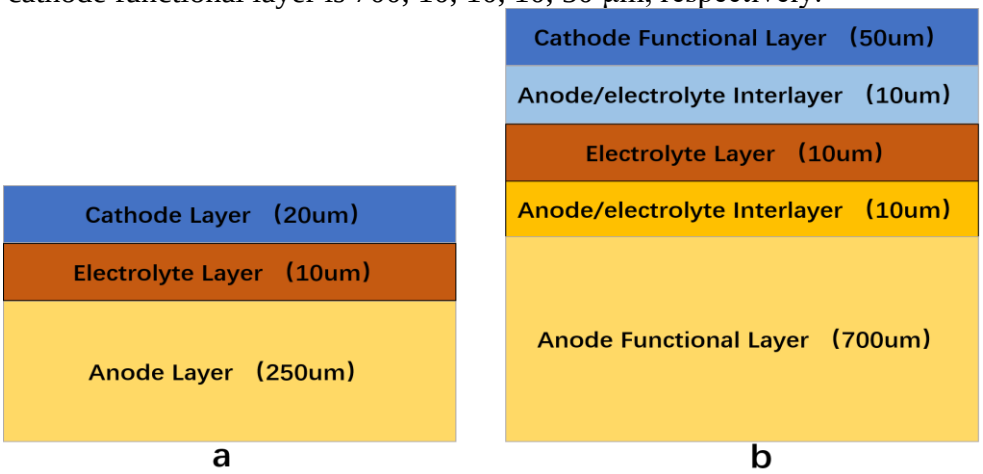

Figure 43. Schematic of a single cell: (a) L3DP method and (b) Traditional EEA cell.

Assuming the anode/electrolyte interlayer materials composition are the same as the anode layer and cathode/electrolyte interlayer materials composition are the same as the cathode layer, the anode layer and the cathode layer of L3DP PCES are 33% and 35.7% thicker than EEA cell, respectively. The materials cost of the L3DP method PCEC is around 34% than EEA cell by rough estimation.

According to the DOE research result of stack manufacturing cost[3], the materials cost of

interconnect is around 1.12 times of cells (based on 10000 units). Assuming the PCES stacks manufactured by L3DP use the same interconnect material as EEA cell stacks, the materials cost of PCES stacks by L3DP is around 31.2% lower than the traditional EEA cell.

2) Production time of a single cell. The PCEC fabrication processes by L3DP and EEA methods are shown in **Figure 44**. The fabrication times for single cells by the L3DP method and EEA method are around 6.3 hours and the 22 hours (tape casting time<1min, screen printing <1 min). L3DP method is around 71% higher efficiency than the EEA method. Corresponding labor working hours is significantly reduced. This means that the labor cost of L3DP is around 71% lower than the EEA method. The DOE research result demonstrated that the materials cost contributing to around 32% of the total stack costs and the labor cost contributing to around 30% of the total stack costs (based on 10000 units). Based on the above estimates, the total PCES stack costs by the L3DP method is around 31.3% lower than the traditional EEA cell.

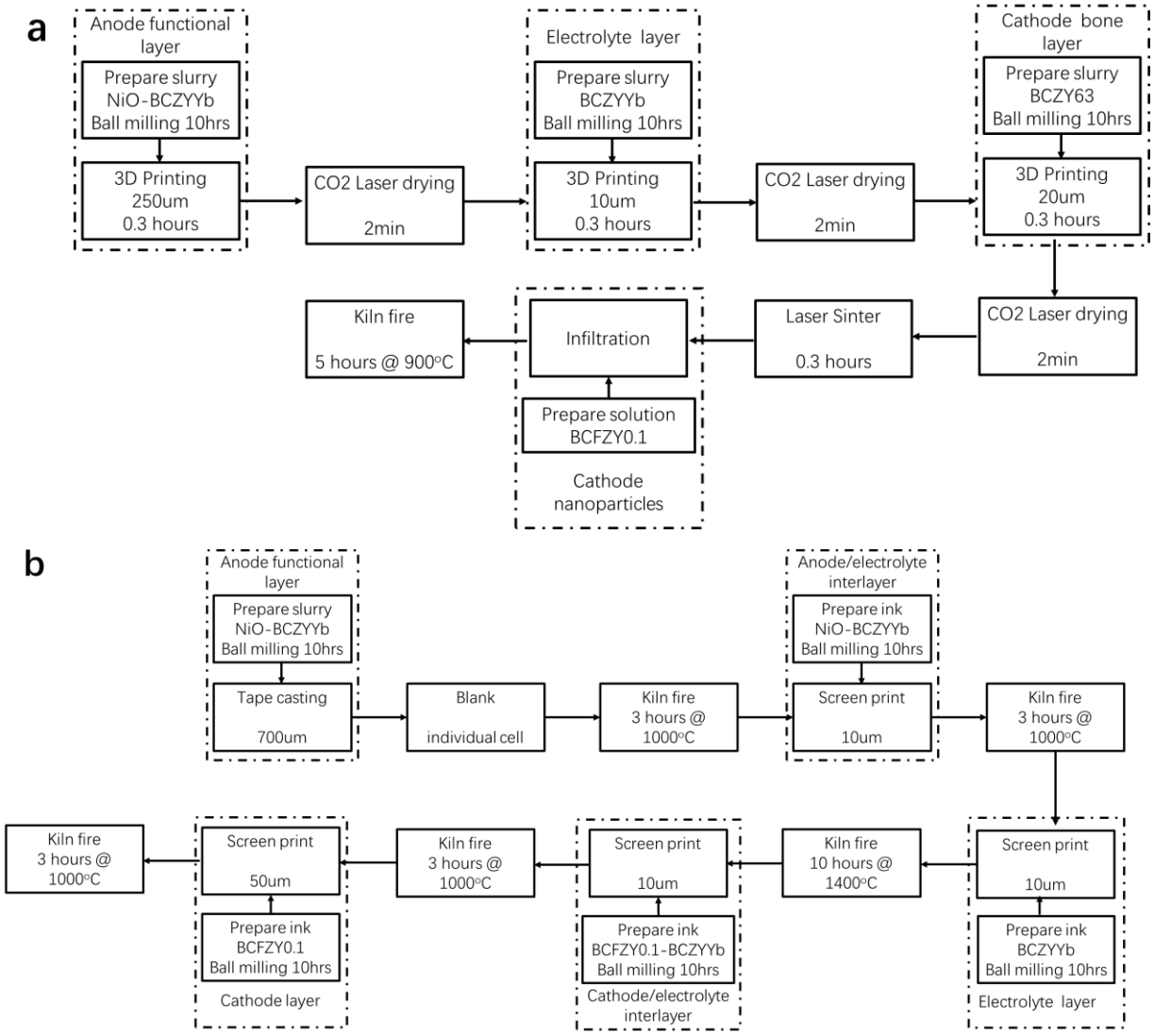

Figure 44. PCEC fabrication process flow. (a) L3DP Process; (b) EEA process

3) Comparison of Energy and power costs. The energy and power costs of the L3DP method in the lab-scale were estimated. 8.82 kWh for raw material mixing process, 20 cells have been printed per batch mixing powder. The electricity consumption of each cell in the raw material

mixing process is 0.44 kWh. Each cell in laser sintering processing is around 2.52 kWh. The total electricity consumption of each cell is 2.96 kWh. The traditional electrolyte-electrode assembly (EEA) cell schematic fabrication in the lab scale is shown in **Figure 45a.** The raw material mixing process is the same ass RLRS. Therefore, the electricity consumption of this process is also 0.44 kWh. The temperature control programs of the electrolyte | anode co-sintering process and the anode | electrolyte | cathode co-sintering process are shown in **Figure 45b,** and **Figure 45c**. The power of furnace working on 1400^{o}C is around 1.33KW. According to temperature control programs, the electricity consumption of these two processes can be roughly estimated to be around 28.04 kWh and 8.98 kWh. Assuming each sintering in the furnace allows the fabrication of 5 cells(10*10cm), the electricity consumption of each cell in the sintering process is 7.4 kWh. The total electricity consumption of each cell is 7.84 kWh. Based on the above estimation, the energy and power costs of the L3DP method is around 62.2% lower than the traditional EEA method.

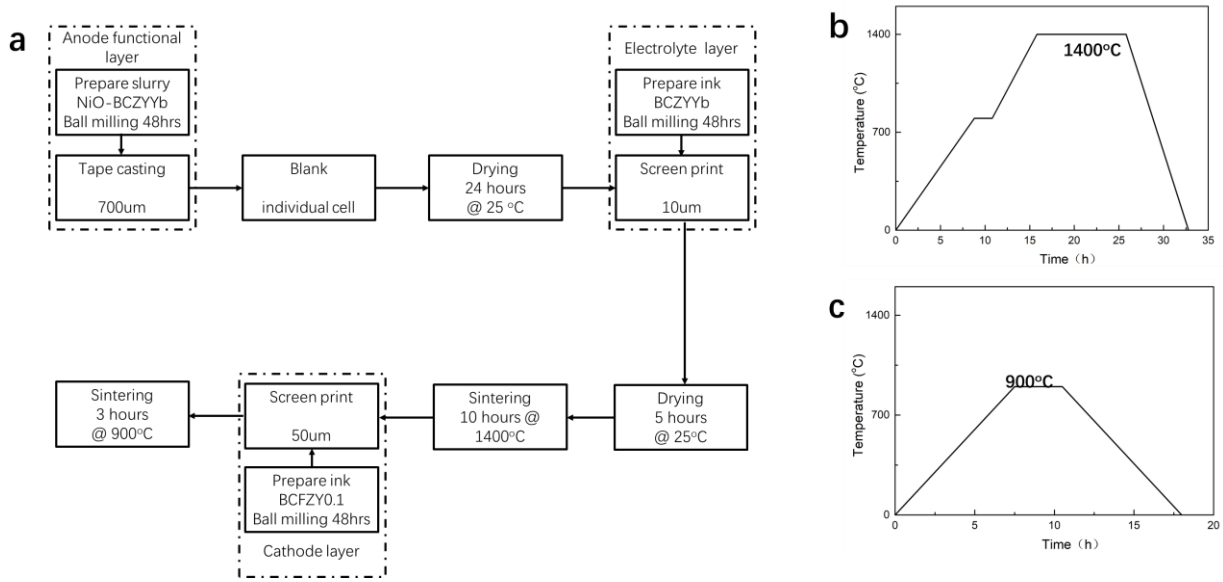

Figure 45. EEA fabrication process in the lab scale (a), temperature control programs of electrolyte/anode co-sintering process(b), and anode/electrolyte/cathode co-sintering process (c).

Go-Not-Go Decision Deliverable Based on All Tasks in Budget Period 1

1) The PCES single cells comprised of 40wt%BCZYYb + 60wt%NiO | BCZYYb | BCFZY0.1 or 40wt%BCZYYb + 60wt%NiO | BCZYYb | BCZY63 + BCFZY0.1 with an active area of >5cm^2 were successfully prepared by L3DP method (two-step and one-step RLRS).

2) The highest electrolysis current density of 1.36A/cm^2 was obtained at 600^{o}C and 1.3V based on 40wt%BCZYYb + 60wt%NiO | BCZYYb | BCFZY0.1 single cells (two-step RLRS) with an area of 0.2 cm^2, which showed a long-term stable operation of ~163 h. Instead of the degradation, the current density steadily increased from 1.161 to 1.794 A/cm^2.

3) The single cells based on 40wt%BCZYYb + 60wt%NiO | BCZYYb | BCFZY0.1(two-step RLRS) with an active area of ~1.35 cm^2 an electrolysis current density of ~530mA/cm^2 at 600^{o}C and 1.3V.

4) The single-cell based on 40wt%BCZYYb + 60wt%NiO | BCZYYb | BCZY63+BCFZY0.1 with an active area of ~0.52 cm^2 was manufactured by one-step RLRS, which showed the

electrolysis current density of ~450 mA/cm^2 at 600 ^{o}C and 1.3V. Instead of degradation, the current density increased from 400 mA/cm^2 to 446 mA/cm^2 within 55 h.

5) The single-cell based on 40wt%BCZYYb+60wt%NiO | BCZYYb | BCZY63+BCFZY0.1 with an active area of ~0.9 cm^2 was manufactured by one-step RLRS, which showed the electrolysis current density of >620 mA/cm^2 at 600 ^{o}C. The stability test is undergoing now. Instead of degradation, the current density increased from 400 mA/cm^2 to 623 mA/cm^2 within 19 h.

6) Assuming the PCES stacks manufactured by L3DP use the same interconnect material as EEA cell stacks, the materials cost of PCES stacks by L3DP is around 31.2% lower than the traditional EEA cell.

7) Based on the above estimation, the energy and power costs of the L3DP method is around 62.2% lower than the traditional EEA methodSingle-celle cell of 40wt% BCZYYb + 60wt% NiO | AFL | BCZYYb+1wt%NiO | BCZYYb + BCFZY0.1 was fabricated by tape casting method, demonstrating stable electrolysis at 600 ^{o}C for more than 1000 h with a constant current density of 1.05 A/cm^2 while applying a voltage of 1.3 V.

10) We completed all the milestones and the go-not-go point for budget period 1.

Budget Period 2: Protonic Ceramic Electrolyzer Stacks by Laser 3D Printing

Task-4 Five-Cell PCES by L3DP

Milestone 4.1 Based on ST-4.1 Laser Machining Microchannels

Milestone 4.1 is based on ST-4.1 Laser Machining Microchannels. The interconnects with designed microchannels should be obtained, showing negligible mass transport resistance and no deterioration of current collecting performance. We must develop the in-situ laser machining technique to manufacture desired microchannels in thin interconnect layers. To finish this task, optimizing the laser processing parameters and the paste properties should be done. The completion of Milestone 4.1 reached **100%**.

Hence, the Ps-laser is applied to do 3D machining and surface modification. With Ps-laser, we can cut microchannels and ceramic devices in any geometry we want on each layer and fabricate the whole part layer by layer. The advantages of this method are non-touching, controllable, stable, high efficiency and low loss. The Ps-laser system is shown in **Figure 46**. A CCD camera was fixed on top of the objective lens for in-situ monitoring of the fabrication process. The laser beam is moved by the three-axial translation stage under the computer control in a predesignated toolpath with a speed of up to 1 m/s. The ps-laser specifications are summarized in Table 3. The parameters such as repetition rate, pulse energy and repeat times are well investigated for green precursors BZY20 system under the 4 W ps-laser system. The machining mechanism of the picosecond laser the vaporization, dissociation, and ablation.

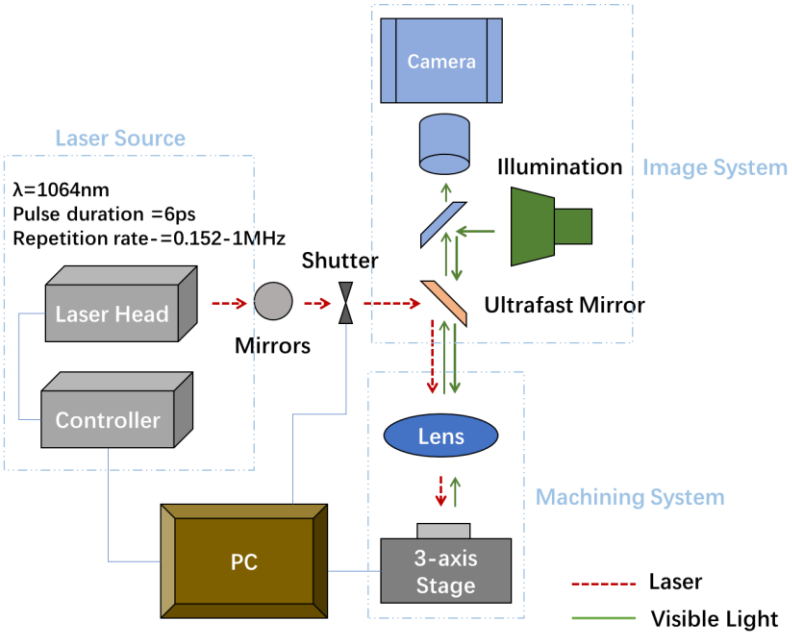

Figure 46. Schematic of the picosecond laser system. The picosecond laser (Olive-1064-10, Attodyne, Inc. Toronto, Canada) with a wavelength of 1064 nm will do the 3D micro-machining. The laser beam was focused using a 5× lens. The spot size was ~18 μm at the focal point. The repetition rate of the laser was set at 10 kHz. The energy per pulse was 150 μJ at 100% output.

Table 3. Picosecond laser specifications.

Model No.	APL4000-1064
Wavelength	1064 nm
Average Max. Power	4 W
Max. Pulse Energy	150 μJ at 10 kHz
Pulse Duration	6 ± 2 ps
Repetition Rate	0.152 Hz – 1 MHz
Beam Divergence	< 3.0 mrad
Beam Diameter	0.5 mm ± 0.3 mm
Mode Quality	TEM_{00}, $M^2 < 1.3$

According to the effect of the repeat times (**Figure 47a** and **c**), the more times we repeat, the deeper the gap was formed. Z-axis feeding after several times cutting can assist the laser spot at the focus point and enhance the effectivity of the process (**Figure 47b**). Comparing **Figure 47a** and **c**, we can easily tell that the higher repetition rate can bring more pulse interaction at one location. However, the pulse energy will decrease and the cutting area with a wider opening which will cause the surface roughness higher and difficult for the coating process. Based on the current results, the slower the cutting speed (**Figure 47a** and **c**) with z-axis feeding, the better the cutting conditions.

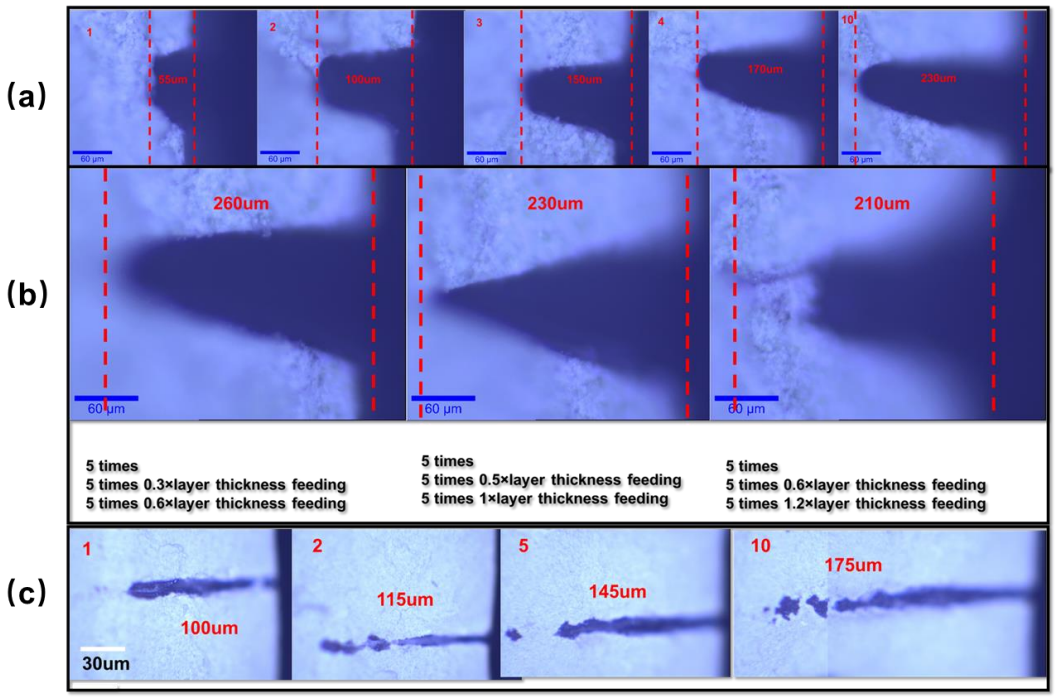

Figure 47. (a) Cross-section view of part cut by Ps-laser with 100 Hz repetition rate, 50mm/s cutting speed, repeat times with 1, 2, 3, 4 and 10 on each layer without z-axil feeding; (b) Cross-section view of part cut by Ps-laser with 100Hz repetition rate, 50mm/s cutting speed, repeat times with 5 on each layer with different feeding distance on z-axil; (c) Cross-section view of part cut by Ps-laser with 100kHz repetition rate, 50mm/s cutting speed, repeat times with 1, 2, 5 and 10 on each layer without z-axil feeding.

The Ps laser cutting on the hard surface was also studied. Fused silica, with 200 µm thickness, was selected as the material for our machining. Applied 10 kHz repetition rate with 90% power out of 100 W, Ps laser can cut through the substrate after 3-time scanning. Moreover, microchannels can be machined by Ps laser into any patterns, such as the sin-shape patten with ~64.5 width and ~200 µm depth (**Figure 48**).

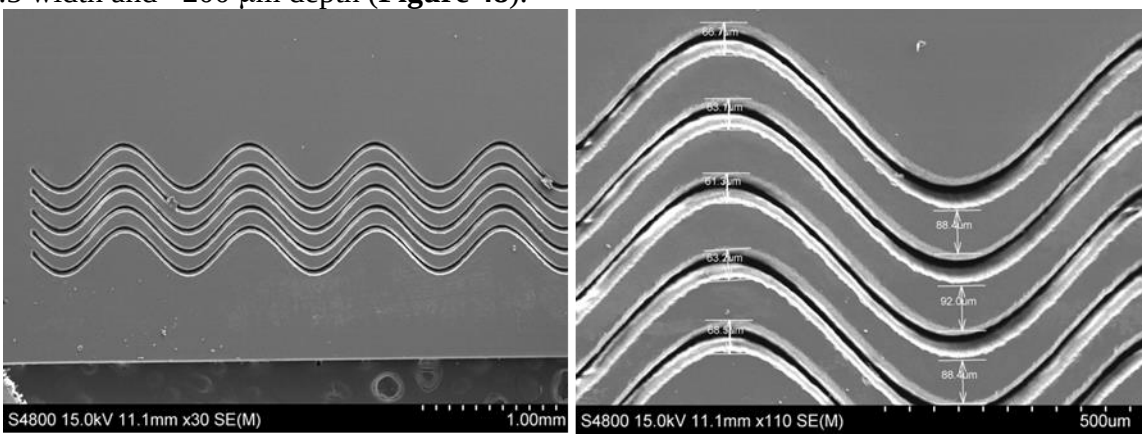

Figure 48. Surface morphology of the Ps laser machined microchannels. The channels obtain sin-shape and are parallel to each other. Accuracy of the width of the microchannels can be controlled by several micrometers.

We studied the cutting microchannel of the sintered BCZYYb pellets using a Ps-laser in the current quarter. We fabricated denes BCZYYb+1wt%NiO electrolyte pellet by the SSRS method and fixed it on the 2D moving stage. **Figure 49** summarizes the characterization results of the machined electrolyte surface by Ps-laser. The original BCZYYb electrolyte surface is dense and shiny (**Figure 49a**), while the machined electrolyte surfaces show high bright and dark contrast corresponding to high and low places. The 3D AFM topography (**Figure 49c** and the 2D roughness result (**Figure 49d**) of the machined electrolyte surface (**Figure 49c**) showed V-shaped channels with a depth of ~10 µm and open width of ~25 µm. Therefore, we can use Ps-laser to machine microchannels with the desired dimension on a sintered electrolyte surface.

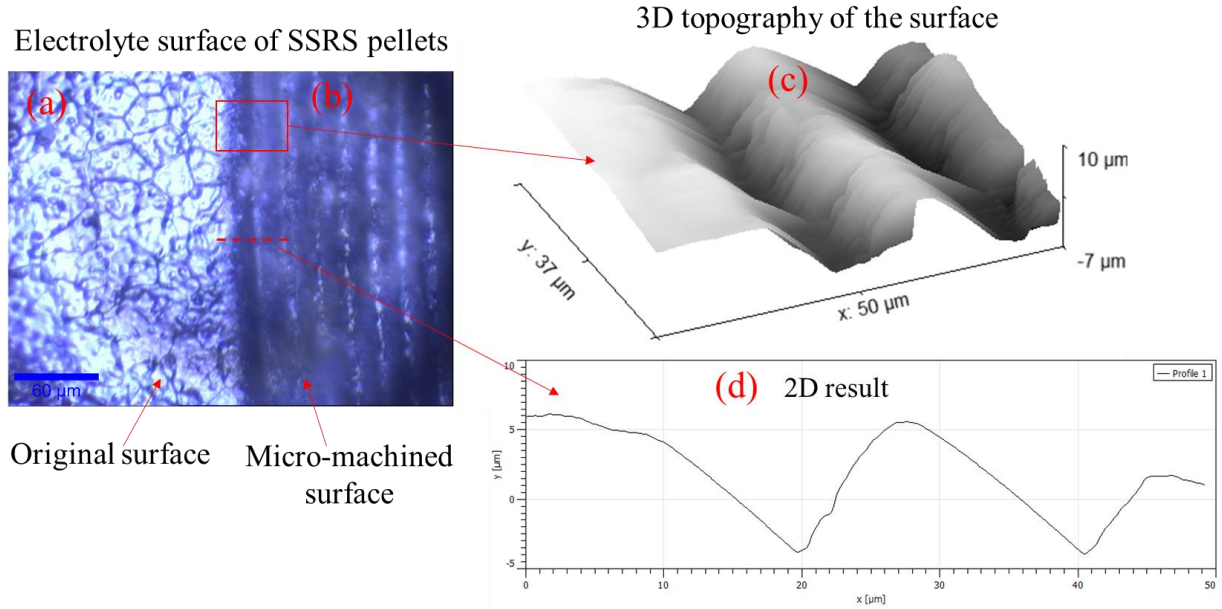

Figure 49. (a) Optical photo of original electrolyte surface, (b) optical photo of machined electrolyte surface, (c) 3D AFM topography of machined electrolyte, and (d) 2D AFM roughness result of machined electrolyte surface.

Although most of these laser-cutting results did not directly focus on the interconnect yet, the laser-cutting understanding and laser operation parameters obtained from green anodes, sintered cathode, and sintered electrolyte can also work for interconnect-cutting. The most crucial concern for microchannel cutting is to achieve microchannels with small width and large aspect ratios since multiple cutting always can make large channels. **Figuree 50** provides the SEM images of a typical laser-cut green anode layer. The smallest microchannel the picosecond laser can cut showed a width of around 50 µm and an aspect ratio of around 6, which can satisfy the requirement for cutting interconnect microchannels.

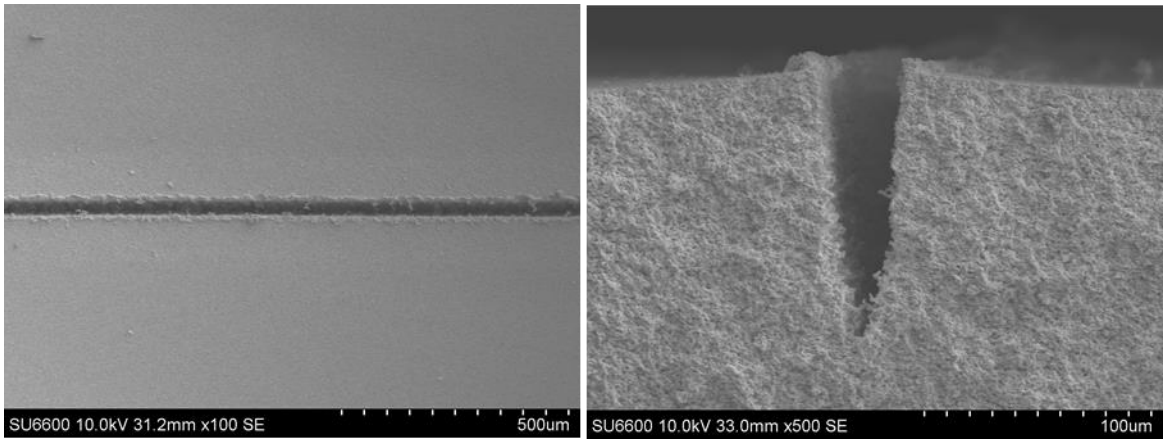

Figure 50. SEM images of a typical anode microchannel prepared by picosecond laser cutting (a) surface and (b) cross-section.

Milestone 4.2 Based on ST-4.2 Manufacturing of PCES by L3DP

Milestone-4.2 is based on ST-4.2 Manufacturing of PCES by L3DP. Develop the programs to control L3DP to manufacture designed PCES. We design and test the programs for controlling the 3D printing stage, micro extruder, CO_2 drying/sintering laser, and picosecond machining laser for manufacturing PCES. It manufactures PCES by L3DP. It also improves the OER and HER kinetics by infiltrating electrocatalyst nanoparticles into the H_2/O_2 electrodes. We have reached 95% of this milestone.

1) Design of Multilayer PCES Stacks

A concept model of PCES was built by solideworks, which is shown in **Figure 51**. **Figure 51a** provides an overview of the 3D model of this stack with 5 cells. The transparent part is the shell of stack. **Figure 51b** and **Figure 51c** are the cutaway view from A and B direction as shown in **Figure 51a**. The components of stack are demonstrated on this figure with various colors. The anode microchannels of five cells are connected from bottom to top and form an "S" shaped gas channel in series with four 180 degree turns to cover each cell. The cathode microchannels are designed in parallel to the A direction.

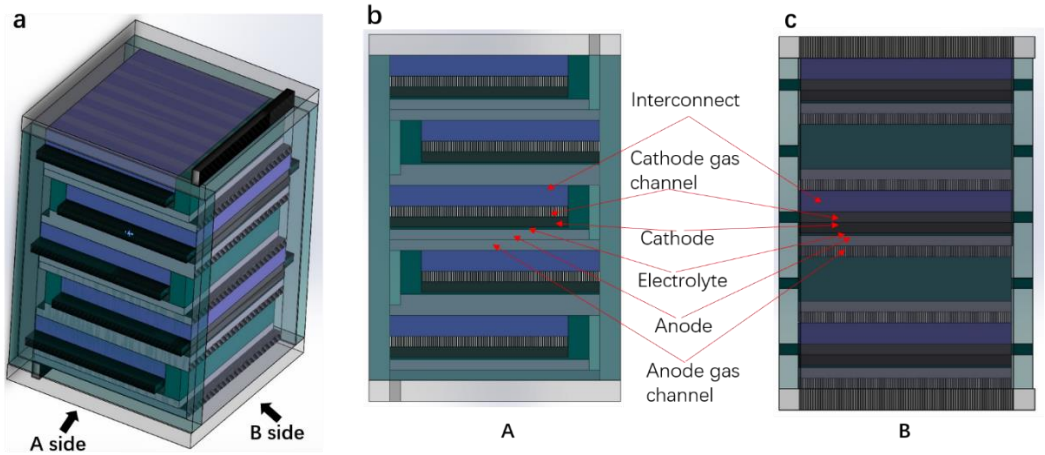

Figure 51. A conceptual design of the PCES.

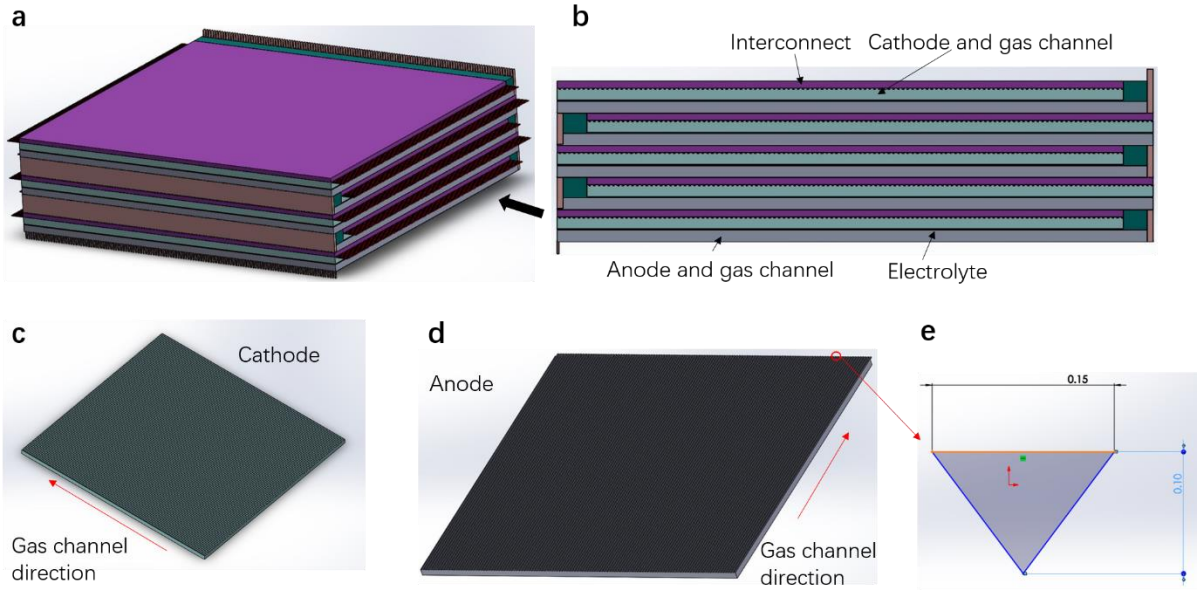

Figure 52. The stack model built in COMSOL. (a) overview; (b) Side view; (c) Cathode with gas microchannel; (d) Anode with gas microchannel; (e) Cross section of gas microchannel.

COMSOL was selected as stack performance simulation software, which is a new simulation model based on the solidworks model. **Figure 52** provides the stack model built using COMSOL Multiphysics software. The dimension of the stack is shown in **Table 4**.

Table 4. stack and component dimension.

anode	50*50*0.5 mm^3
electrolyte	50*50*0.1 mm^3
cathode	45*50*0.5 mm^3
Interconnect	45*50*0.3 mm^3
stack	55*55*17 mm^3

The triangle gas microchannel was designed (**Figure 52e**) because the Ps-laser can easily cut triangle microchannel. The designed triangle microchannels have a dimension of 100 μm height and 150 μm base. According to the anode and cathode size, 125 and 112 gas microchannels are evenly distributed on the anode and cathode surface, respectively.

Anode gas flow simulation. In order to simulate the anode gas flow, the "S" shape of gas microchannel inside the fuel cell was extracted separately from the stack model as shown in **Figure 53**. The gas cavity connected with each layer of anode gas microchannel is a rectangular chamber.

Figure 53. The "S" shape anode gas microchannels.

The calculated Reynolds Number indicates that the gas flow in the anode microchannels is laminar flow. So the laminar flow module in the COMSOL was used. The gas was fed into the anode microchannels from the bottom of the fuel cell and then merged together at relatively larger rectangular chamber between each cells. The gas ultimately flows out of the fuel cell stack at the top. The pressure drop of anode microchannel is analyzed with the input parameters in **Table 5**, and the result is shown in **Figure 54**.

Table 5. Parameter and operation condition of anode press drop.

Gas	Nitrogen
Temperature	793.15 K
Inlet flow rate	100-1000 ml/min
Outlet pressure	1 atm
Fluid type	Laminar flow

The gas was fed into the microchannels from the inlet at the bottom. The different colors of microchannels of **Figure 54a** and **Figure 54b** at various locations which represent the pressure at that location. According to the scale bar, the pressure drop of the anode with 100 ml/min (**Fig. 54a**) gas inlet flow rate is observed to be 1%. Even though the inlet flow rate is increased by 10 times to 1000 ml/min (**Figure 54b**), the pressure drop is only 6%. It is means that the microchannel fabricated by Ps-laser will not cause a huge pressure drop of gas.

The gas velocity through each microchannel was also been simulated. The velocity distribution of the microchannels demonstrates typical laminar flow characteristics. The velocity distribution of each microchannel doesn't show the obvious difference, even though the microchannel location is in the middle and side of the anode (**Figure 54c** and **Figure 54d**). The velocity drops at the large chambers in between layers due to the gas expansion.

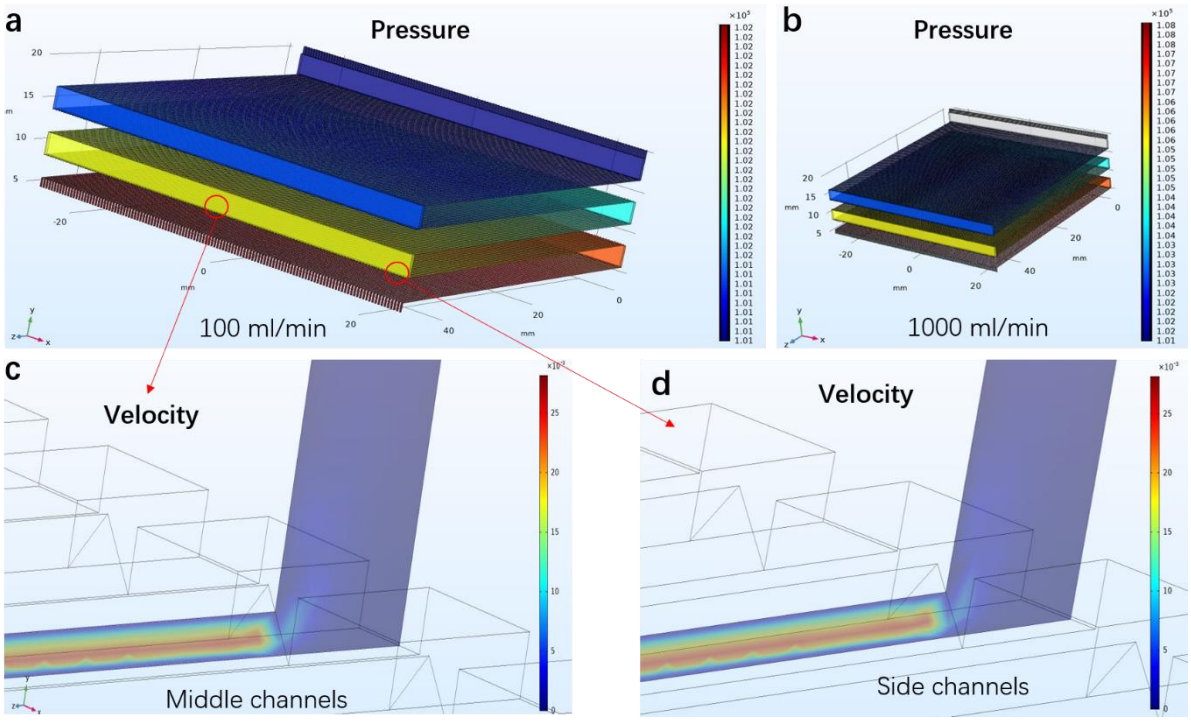

Figure 54. Pressure drop and velocity simulation of anode microchannels.

Gas diffusion simulation. The effect of porosity on fuel gas diffusion in porous anode was investigated by COMSOL. A 2D cross-section area of the anode consists of two microchannels is simulated. In COMSOL, the transport of diluted species in porous media interface was used to simulate the diffusion process of H_2 into the porous anode material. Assuming the H_2 concentration is stationary. By tracking the H_2 concentration in the anode material, the diffusion speed can be observed for different porosities of the material. The simulation condition is shown in **Table 6**.

Table 6. Parameter of simulation condition on fuel gas diffusion in porous anode

Temperature	873.15 K
Hydrogen concentration	0.05 mol/ m^3
Pressure	1 atm
Anode Porosity	20%-60%
Tortuosity	3
Permeability	$4.16X10^{-15}$ m^2
Diffusion coefficient	0.12 cm^2/s

The time-dependent simulated result is shown in **Figure 55**. It is demonstrated hydrogen concentration profile at 0.01s in various anode porosity (20-60%). The solid black line is the 0.04 mol/m^3 contour of concentration. The furtherer the 0.04 mol/m^3 line away from the gas channel/anode interface, the faster the diffusion.

As porosity increases, the overall diffusion speed increases, while from 20% to 40% porosity, the increase of diffusion speed is higher than that of over 40%. Implying that when porosity is higher than 40%, it is not a major limiting factor for difthe fusivity of the anode.

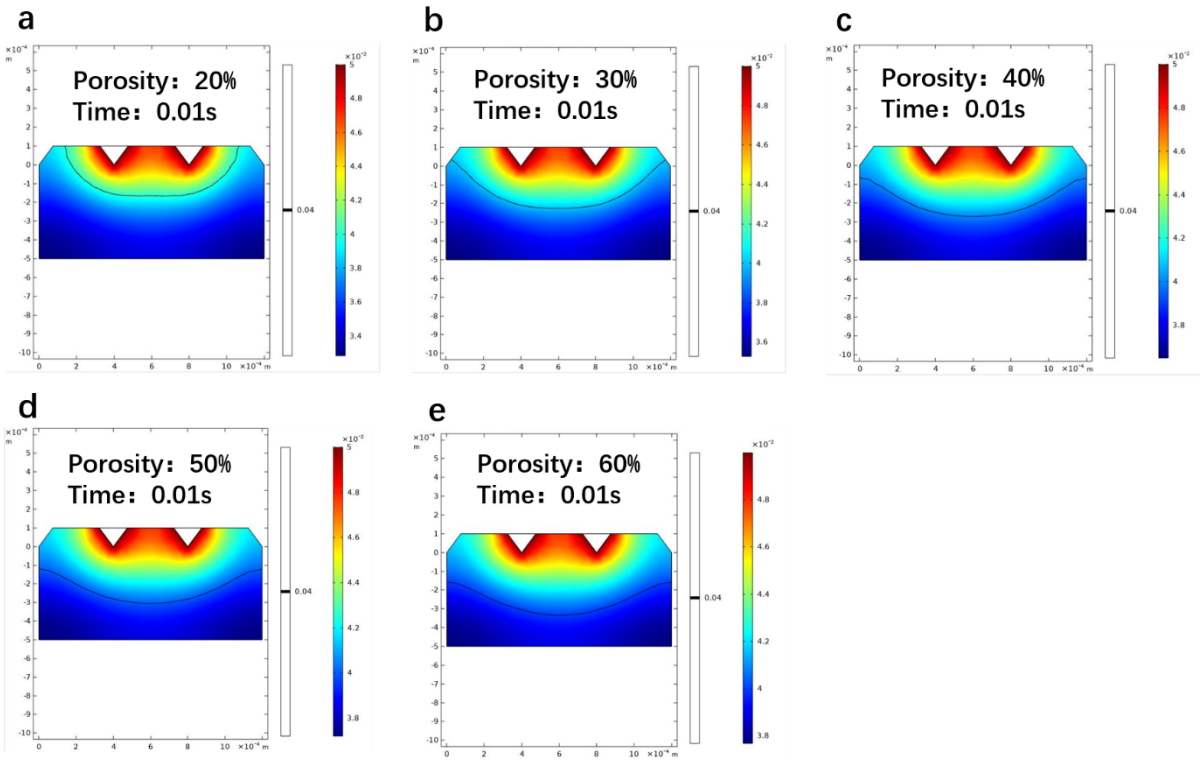

Figure 55. Hydrogen concentration profile at 0.01s in various anode porosity. (a) Porosity 20%; (b) Porosity 30%; (c) Porosity 40%; (d) Porosity 50%; (e) Porosity 60%.

A concept model of PCES was designed by solideworks for 3D printing. And a functional simulation model with real size was built by COMSOL Multiphysics for Computational simulation of the stack operation. The "S" shape anode gas microchannel inside the fuel cell was extracted separately for pressure drop and velocity analyst. The pressure drop of the anode gas is observed to be 1% and the velocity distribution of each microchannel doesn't show obvious difference. The effect of porosity on fuel gas diffusion in porous anode was also investigated in this quarter. Hydrogen diffuses very fast in porous anode and transferred to the anode and electrolyte interface in less than 0.01 s. As anode porosity increases, the overall diffusion speed is increased.

2) Segmented-in-series Stack

Our previous work successfully fabricated anode-supported electrolyte half cells with a width of around 10 mm and a length longer than 10 cm by the RLRS technique. We have achieved an excellent peak power density of more than 500 mW/cm^2 at 600^{o}C under the Air/H_2 gradient. The CO_2 laser through the cylindrical lens limited our half-cell's width, and the Galvano laser scanning can achieve large-area cells. Simultaneously, we thought about modifying the large-area layer-by-layer stack design to fully use our currently mature L3DP technique for fully manufacturing stacks. We designed a new segmented-in-series (SIS) stack design. Instead of stacking the cells layer-by-layer, the new design places the cells side-by-side to form a stack in a planar way, as shown in **Figure 56**.

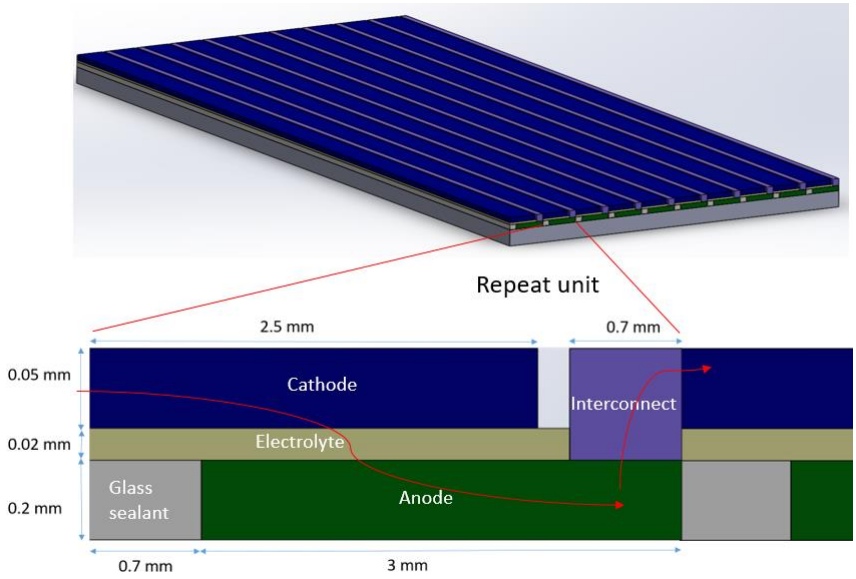

Figure 56. Segmented-in-series stack design.

3) Fabricate Porous BCFZY0.1 O_2 Electrode by CO_2 Laser Scanning

We studied the fabrication of the BCFZY0.1 O_2 electrode for desired crystal structure and microstructure by CO_2 laser scanning, allowing the integration of the L3DP the single cells and stacks. We started from a BCFZY0.1 raw materials paste prepared according to the previous method. After brushing the BCFZY0.1 paste on the co-fired anode supported electrolyte half-cells (furnace sintered), we sintered the green cathode layer using a cylindrical lens adjusted CO_2 laser. We did an initial analysis of the microstructure and crystal structure using SEM and XRD, respectively and summarized the results in **Figure 57**. The laser-sintered cathode (**Figure 57a, b, c**) shows a porous microstructure, much like the one sintered in the furnace. The grain size of the sintered BCFZY0.1 is around 100-300nm, the expected for a high-performance cathode. **Figure 57d** (the XRD pattern of the laser-sintered BCFZY0.1) indicates that the rapid laser could form the desired perovskite phase for BCFZY0.1.

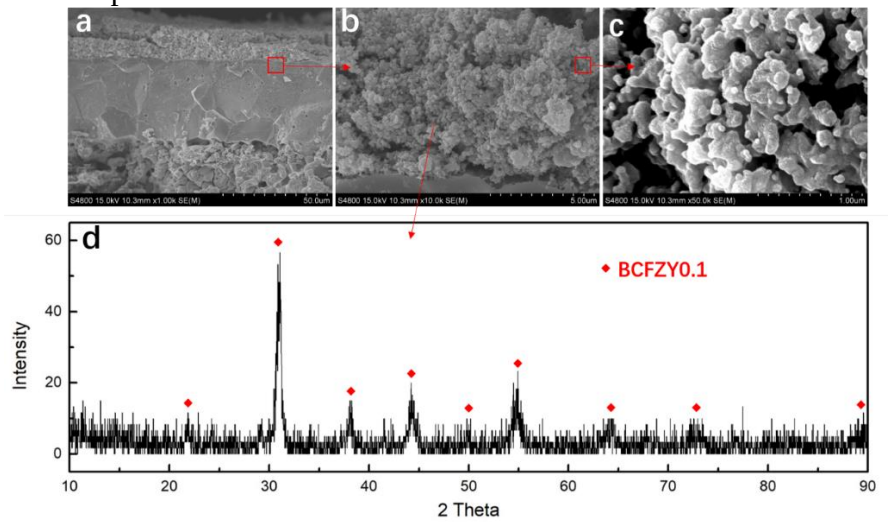

Figure 57. The microstructure and crystal structure of laser-sintered BCFZY0.1 cathode

4) Manufacturing of Large-Area Half Cells by RLRS

We fabricated large-area half cells using the rapid laser reactive sintering (RLRS) method using our 250 W CO_2 laser. This work aims to get large-area single cells for achieving high single-cell performance and integrating segmented-in-series stack. We performed RLRS of the green half cells by shining the laser beam through a cylindrical lens to transform a point laser into a line laser. The defocus distance was 75 mm, and the scanning speed was 0.1 mm/s. **Figure 58** provides the photos of some rectangular half cells prepared by RLRS. The samples are between 5mm to 10mm in width and 90 mm in length. As we can see from the caliper, the thickness is 310 μm, which is our desired half-cell thickness. These results further indicate that the RLRS technique can improve the reproducibility for manufacturing half-cells.

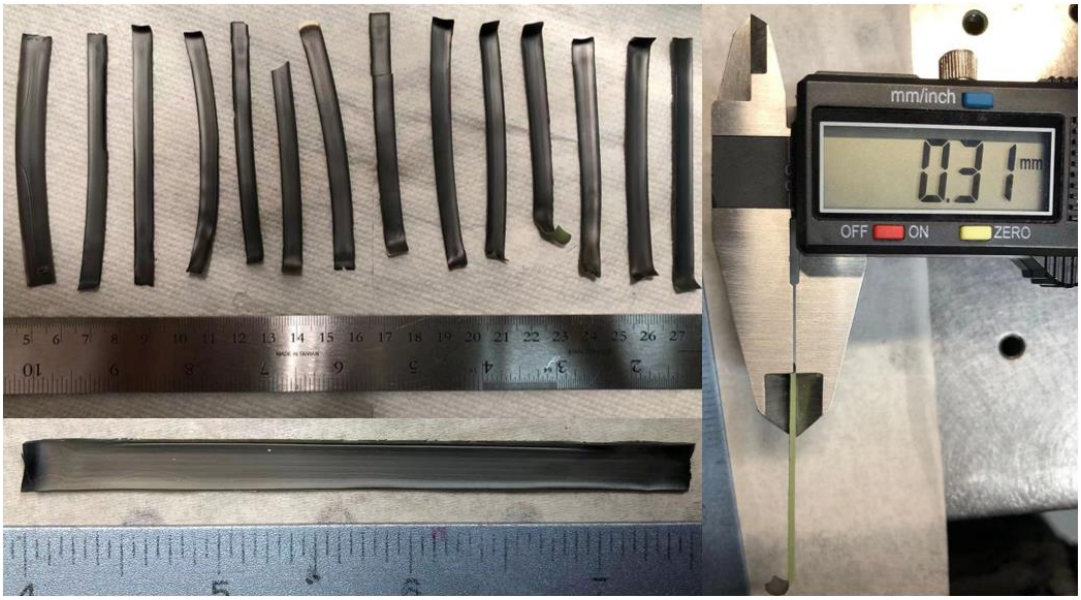

Figure 58. Photos of half-cells prepared by RLRS using 250W CO_2 laser

5) PCES single cells made from RLRS prepared half cells and brushed cathode

The 40wt% BCZYYb + 60wt% NiO | BCZYYb +1wt% NiO half cells with larger areas were co-sintered by the CO_2 laser (RLRS). The width of the cells was limited to around 0.8-1.0 cm by the laser beam. The length of rectangular half cells reached10 cm, which can be much longer while utilizing longer substrates. The BCFZY0.1 cathode was brushed on the electrolyte surface of the half-cell and annealed in a furnace at 900 ^{o}C for 2 h. **Figure 59** provides a photo of the PCES single cells made from RLRS prepared half-cells and brushed cathode. The areas of the single cells of 40wt% BCZYYb + 60wt% NiO | BCZYYb +1wt% NiO (RLRS-prepared) | BCFZY0.1 (Brushed) are around 1-5 cm^2, showing no noticeable cracks by naked eyes.

.

Figure 59. Photo of the PCES single cells of NiO-BCZYYb | BCZYYb | BCFZY0.1 made from RLRS prepared half cells and brushed cathode.

Cell 1: 40wt% BCZYYb + 60wt% NiO | BCZYYb +1wt% NiO (RLRS-prepared) | BCFZY0.1 (Brushed) (1.03 cm^2)

We developed a new round shape testing set with a diameter of 4.2 cm to the performance of large-area cells. Cell 1 with an active cell area of 1.03 cm^2 was set up using this round shape set (**Fig. 60a**) and tested for fuel cell performance. **Fig. 60b** provides the I-V and I-P curves of the cell at 500ºC-700ºC under air/H_2. The peak power densities for cell 1 are 723 mW/cm^2, 532 mW/cm^2, 385 mW/cm^2, 255 mW/cm^2 and 146 mW/cm^2, at 700ºC, 650ºC, 600ºC, 550ºC and 500ºC, respectively. **Fig. 60c** provides the EIS Nyquist plots of cell 1 under an open-circuit condition. The electrolyte and the electrode both show relatively small ASRs, consisting of the observed high fuel cell power density. Cell 1 is the first demonstration of the monolithic cells with an effective area larger than 1.0 cm^2 made from RLRS prepared half-cells and brushed cathode. **Fig. 61** provides the SEM images of the cross-section of cell 1 after testing of fuel cell performance. **Fig. 61a** shows that cell 1 has the desired three-layer structure. The adherence between cathode and electrolyte and the adherence between anode and electrolyte are both pretty good. The thickness of the dense electrolyte layer is around 17 μm. By combining the electrolyte ASR value shown in **Fig. 60c**, we calculated the electrolyte conductivity of 0.47×10^{-2} $\Omega^{-1}\bullet cm^{-1}$ at 600 ºC, indicating that RLRS could ensure a good electrolyte layer. **Figure 61b** and **Figure 61c** indicate that both the cathode and anode have desired porous microstructure.

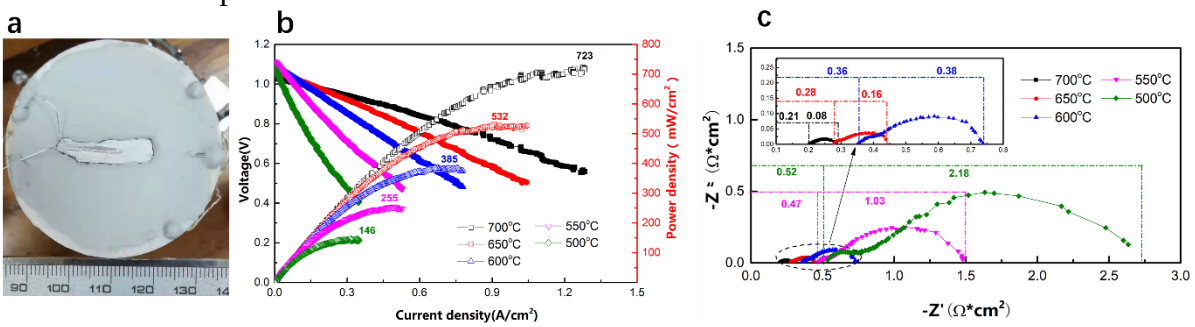

Figure 60. The photo (a), performance (b), and EIS characterization (c) of cell 1.

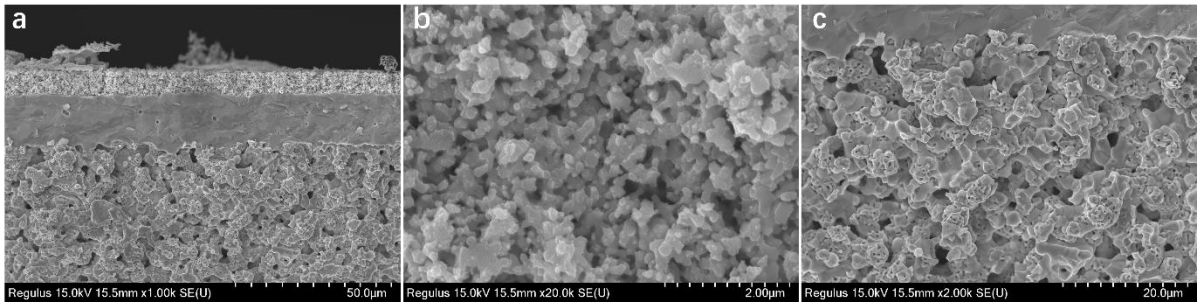

Figure 61. The SEM images of cross-sections of cell 1 after testing. (a) there-layer cross-section, (b) cathode microstructure, and (c) anode microstructure (connected to electrolyte).

Cell 2 40wt% BCZYYb + 60wt% NiO | BCZYYb +1wt% NiO (RLRS-prepared) | BCFZY0.1 (Brushed) (1.43 cm^2)

Cell 2 is the same as cell 1 except for the larger active area (1.43 cm^2 vs. 1.03 cm^2). We tested cell 2 for fuel cell performance using the same round-shape testing set (**Figure 62a**). **Figure 62b** provides the I-V and I-P curves for cell 2 at 500°C-700°C under an air/H_2 gradient. The peak power densities at 700 °C, 650 °C, and 600°C are 705 mW/cm^2, 635 mW/cm^2, and 430 mW/cm^2, respectively. The performance is a little bit better than that for cell 1. Specifically, the peak power density at 600 °C for cell 2 is 19% higher than for cell 1. **Figure 62c** further indicates that cell 2 demonstrated a smaller ASR than that of cell 1. **Figure 63** provides the SEM images of cell 2 after fuel cell performance testing. The cathode and anode microstructures are close to cell 1. However, the grain boundary of the electrolyte layer for cell 2 is not very clear. The conductivity at 600 °C calculated from electrolyte ASR and electrolyte thickness is 0.62×10^{-2} Ω^{-1} •cm^{-1}, which is a little bit higher than that for cell 1 (0.47×10^{-2} Ω^{-1}•cm^{-1}). The better electrolyte microstructure may be the reason for higher fuel cell performance.

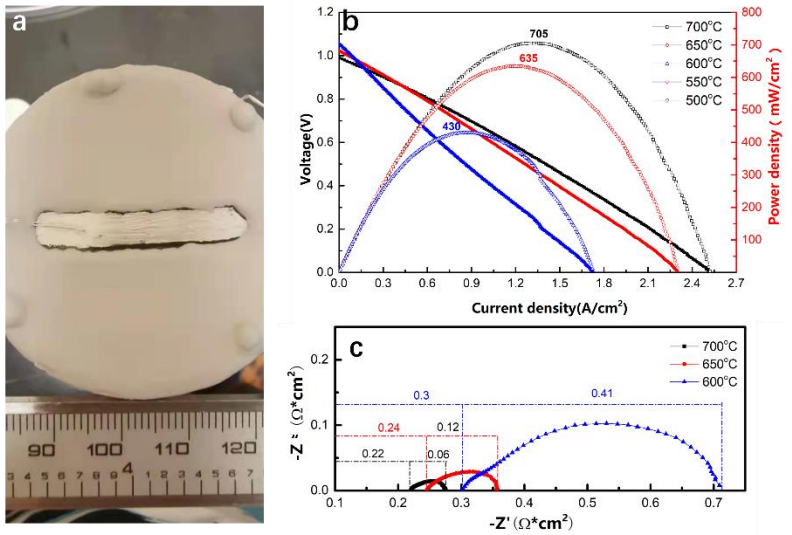

Figure 62. The photo (a), performance (b), and EIS characterization (c) of cell 2 (1.43 cm^2).

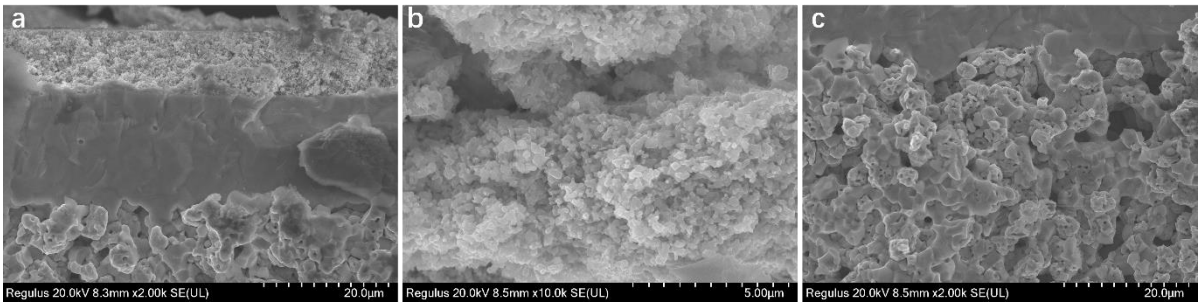

Figure 63. The SEM images of cross-sections of cell 2 after testing. (a) there-layer cross-section, (b) cathode microstructure, and (c) anode microstructure (connected to electrolyte).

f) PCES single cells made from complete laser processing

We fabricated half cells by the rapid laser reactive sintering (RLRS) method by co-firing anode-supported electrolyte two layers using the CO_2 laser. Then cathode scaffold layer was printed on the top of the electrolyte surface of the sintered half cells. Another laser sintering was applied to bond the cathode scaffold to the electrolyte to form the sandwiched single cells. The further infiltration of BCFZY0.1 precursor solution introduced the active cathode nanoparticles. We defined these single cells as complete laser-processed cells. **Figure 64** summarizes photos of sintered half cells, single cells with green cathode scaffold layer, and the single cells. The single cells were also sealed to an alumina tube and tested for fuel cells and electrolysis performance.

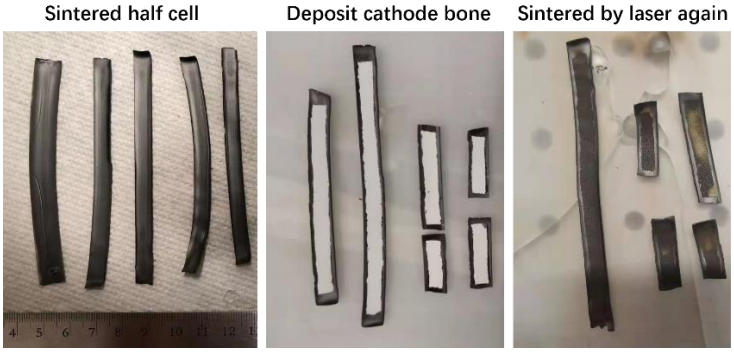

Figure 64. The photos of the half cells, single cells with green cathode scaffold, and sintered single cells

Cell 3: 40wt% BCZYYb + 60wt% NiO | BCZYYb +1wt% NiO | BCZY63+BCFZY0.1 (0.32 cm^2) by complete laser processing

Cell 3 40wt% BCZYYb + 60wt% NiO | BCZYYb +1wt% NiO | BCZY63 + BCFZY0.1 (0.32 cm^2) is a single cell fabricated by complete laser processing as described above. **Figure 65a** indicates the peak power density of cell 3 at 700 ^oC, 650 ^oC, and 600^oC are 620 mW/cm^2, 505 mW/cm^2 and 383 mW/cm^2, respectively, which is a little bit higher than than the previous 3-layer co-sintering cells. **Table 7** provides the OCVs of cell 3 at different temperatures. The high OCVs are probably one reason for the higher performance.

Table 7. The OCV of cell 3 at PCFC mode

Temperature	450 ^oC	500 ^oC	550 ^oC	600 ^oC	650 ^oC	700 ^oC
OCV	1.174	1.16	1.13	1.102	1.072	1.046

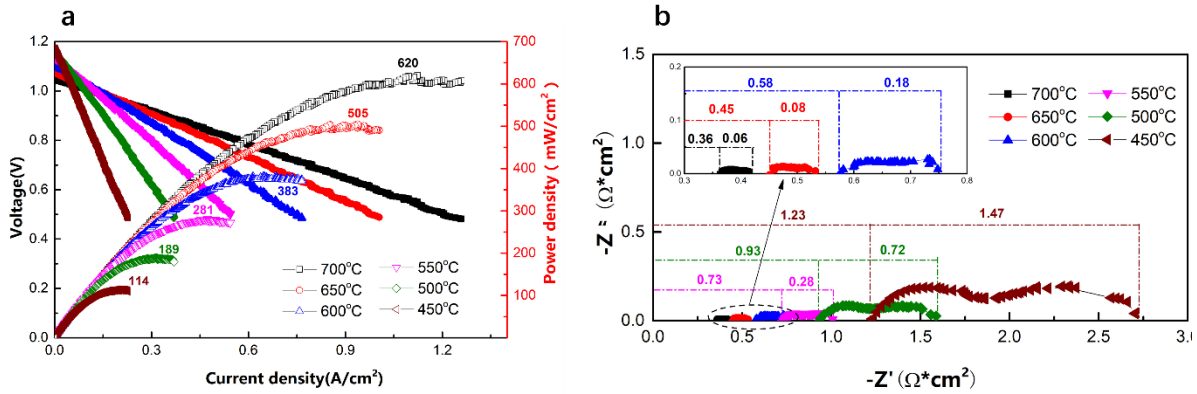

Figure 65. The performance (a) and EIS characterization (b) of cell 3 when operating in fuel cell mode.

After PCFC performance testing, wet air (30% H_2O) and 5% H_2 (balance with Ar) were fed into O_2 electrode(200ml/min) and H_2 electrode (50ml/min), respectively. Cell 3 was switched to PCEC for electrolysis performance testing. This cell demonstrated a decent electrolysis performance (**Figure 66**). The current density at 600 ºC is around 0.45 A/cm^2 while applying a voltage of 1.3V, still lower than the expected one according to the fuel cell's performance. There are two reasons: the first is that the polarization resistance is around 3-4 times bigger than that in PCFC mode; the second is that the OCV of the cell at 600ºC is 0.95V, there is a low potential gradient to obtained higher current density.

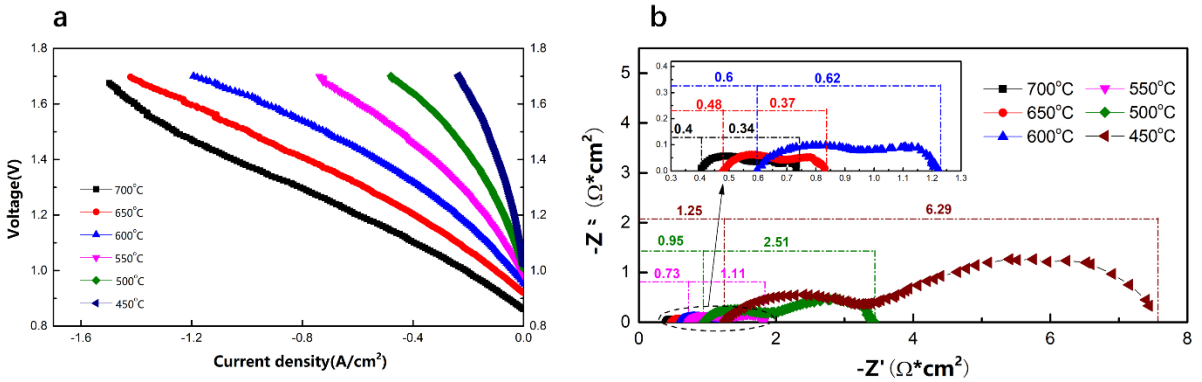

Figure 66. The performance (a) and EIS characterization (b) of cell 3 when operating in the electrolysis mode.

Cell 4: 40wt% BCZYYb + 60wt% NiO | BCZYYb +1wt% NiO | BCZY63+BCFZY0.1 (0.35 cm^2) by complete laser processing

Cell 4 is single-cell prepared by complete laser processing, which has a similar configuration and active area. **Figure 67** provides the I-V and I-P curves at 550 ºC-700 ºC under an air/H_2 gradient while operating in fuel cell mode. This cell demonstrated a better performance than cell 3. The peak power densities for cell 4 at 700 ºC, 650 ºC, 600 ºC, and 550 ºC are 851 mW/cm^2, 635 mW/cm^2, 500 mW/cm^2, and 430 mW/cm^2, respectively. The OCVs at 700 ºC, 650 ºC, and 600 ºC are 1.028V, 1.057V, and 1.056V, respectively. The results proved that single cells made by complete laser processing could achieve much higher performance. The EIS characterization results (**Figure 67b**) indicate that the electrolyte and electrode resistances are relatively low. The morphology of cell 4 (**Figure 68**) shows that all three layers of cell 4 formed the desired microstructure. The grain boundary in the electrolyte is not clear. The conductivity at 600 ºC is around $0.6\times10^{-2}\ \Omega^{-1}\bullet cm^{-1}$.

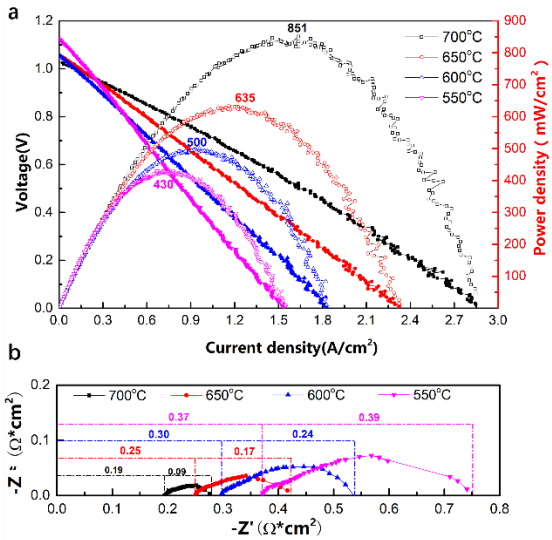

Figure 67. The performance (a) and EIS characterization (b) of cell 4 while operating in fuel cell mode.

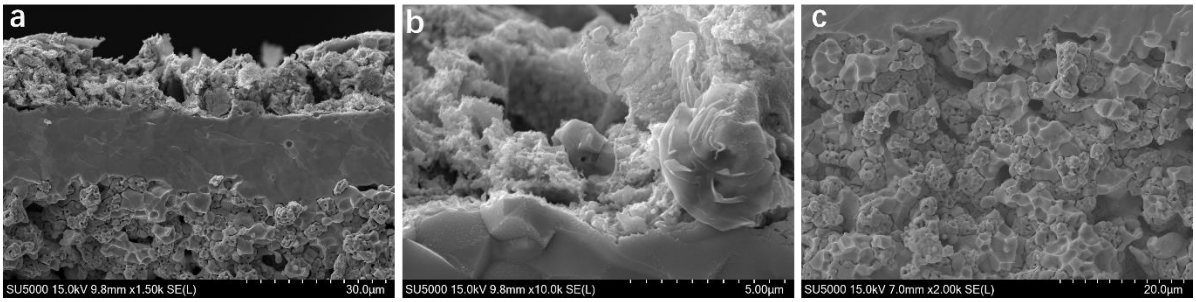

Figure 68. The SEM images of cross-sections of cell 4 after testing. (a) there-layer cross-section, (b) cathode microstructure, and (c) anode microstructure (connected to electrolyte).

Cell 5: 40wt% BCZYYb + 60wt% NiO | BCZYYb +1wt% NiO | BCZY63+BCFZY0.1 (0.37 cm^2) by complete laser processing

Cell 5 is similar to cell 3 and cell 4. This cell demonstrated higher OCV than cell 4, and better performance was obtained, as shown in **Figure 69**. The max power density of this cell at 700 ^{o}C, 650 ^{o}C, 600 ^{o}C, and 550 ^{o}C are 1014 mW/cm^2, 825 mW/cm^2, 709 mW/cm^2, and 502 mW/cm^2, respectively. The OCVs at 700 ^{o}C, 650 ^{o}C, 600 ^{o}C, and 550 ^{o}C are 1.04 V, 1.071V, 1.108V, and 1.147 V, respectively. The morphology of cell 5 is shown in **Figure 70**. The conductivity at 600 ^{o}C is $0.7\times10^{-2}\ \Omega^{-1}cm^{-1}$.

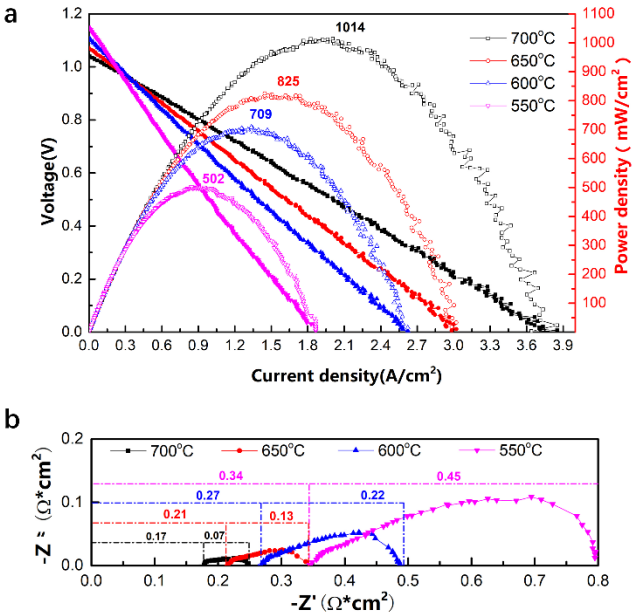

Figure 69. The performance (a) and EIS characterization (b) of cell 5 while operating in fuel cell mode.

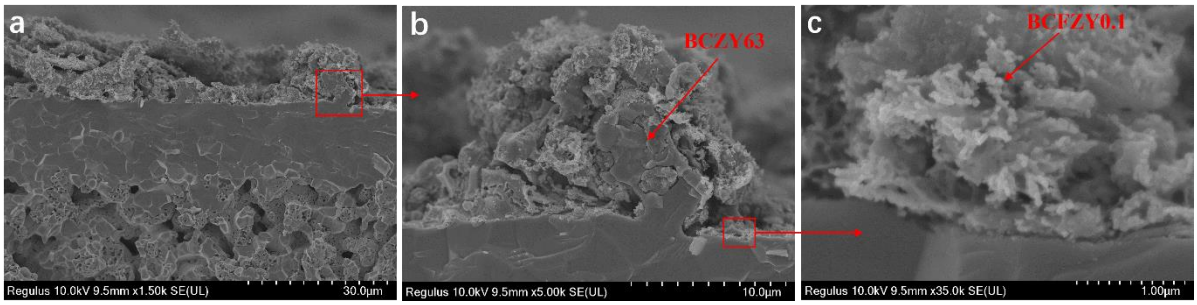

Figure 70. The SEM images of cross-sections of cell 5 after testing. (a) there-layer cross-section, (b) cathode microstructure, and (c) anode microstructure (connected to electrolyte).

g) PCES single cells made from RLRS-prepared half cells and brushed cathode

The 40wt% BCZYYb + 60wt% NiO | BCZYYb +1wt% NiO half cells with larger areas were co-sintered by the CO_2 laser (RLRS). The width of the cells was limited to around 0.8-1 cm by the laser beam. The rectangular half cells reached10 cm, which can be much longer while utilizing longer substrates. The BCFZY0.1 cathode was brushed on the electrolyte surface of the half-cell and annealed in a furnace at 900 ^oC for 2 h. The areas of the single cells of 40wt% BCZYYb + 60wt% NiO | BCZYYb +1wt% NiO (RLRS-prepared) | BCFZY0.1 (Brushed) are around 1-5 cm^2. **Cell 6: 40wt% BCZYYb + 60wt% NiO | BCZYYb +1wt% NiO (RLRS-prepared) | BCFZY0.1 (Brushed) (1.54 cm^2)**

Cell 6 was fabricated using a laser co-sintered NiO-BCZYYb/BCZYYb half cell and BCFZY0.1 cathode (furnace sintered) with a 1.54 cm^2 effective area. The picture of the cell is shown in **Figure 71a**, and the cell performance and EIS analysis are shown in **Figures 71b** and **71c**. The cell performance was tested from 550 ^oC to 700 ^oC with a step size of 50^oC under an H_2/air gradient. The peak power densities of 796 mW/cm^2, 688 mW/cm^2, 590 mW/cm^2 and 460 mW/cm^2 were obtained at 700 ^oC, 650 ^oC, 600 ^oC and 550 ^oC, respectively. The peak power density at 550 ^oC is even higher than the value (~410 mW/cm^2) obtained for the state-of-the-art small

button cells fabricated by the SSRS method. But the cell OCVs were not very high (0.98, 1.00, 1.03, and 1.05V at 700, 650, 600, and 550 °C, respectively), indicating the existence of a small leak and the possibility for further improvement of the performance.

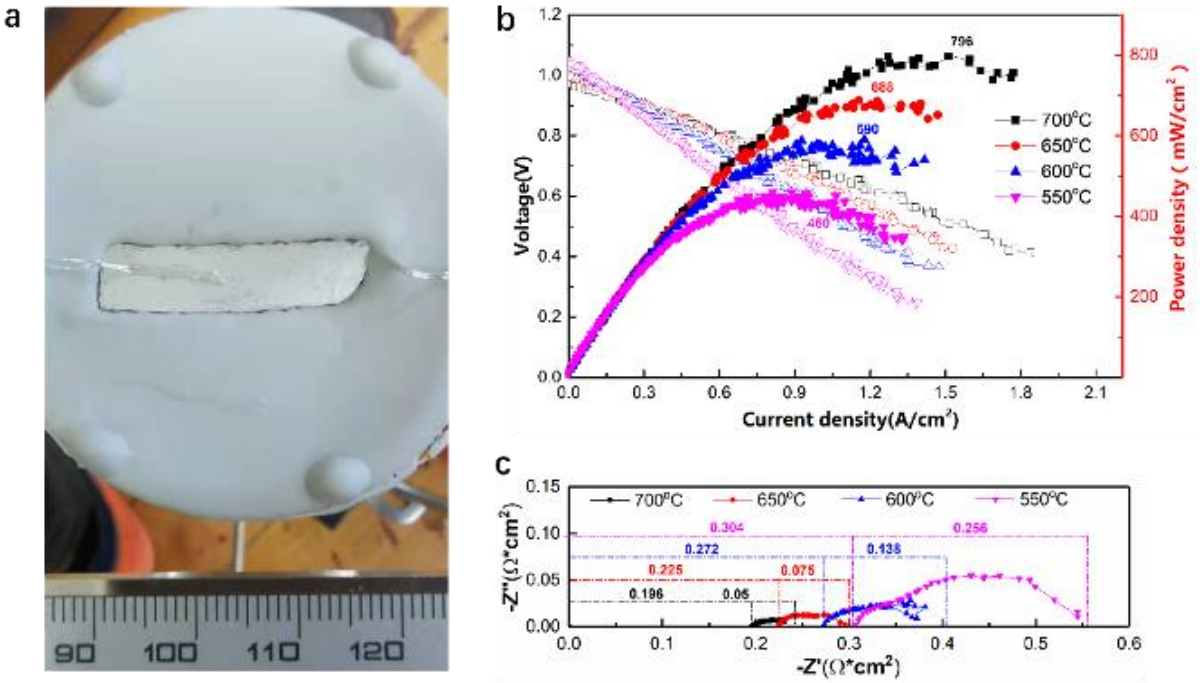

Figure 71. Testing and characterization results of cell 6. (a) Photo of cell 6 after testing, (b) I-V and I-P curves of cell 6 at 550-700°C under H_2/air gradient, and (c) EIS Nyquist plots of cell 6 at open circuit condition at 550-700°C under H_2/air gradient.

The morphology of cell 6 after testing is shown in **Figure 72**. **Figure 72a** indicates that the porous cathode and anode still adhere to the dense electrolyte thin layer very well. The electrolyte thickness is around 15μm. **Figure 72b** proves that the electrolyte was fully densified by RLRS. **Figure 72c** indicates that the cathode still kept the highly porous microstructure. Based on the electrolyte thickness and the ionic ASR (**Figure 71c**), we calculated the electrolyte conductivity at 600 °C was 0.55×10^{-2} $\Omega^{-1}cm^{-1}$, which is a decent number for BCZYYb electrolyte. Both the electrolyte conductivity and thickness have room to be further improved for achieving higher performance.

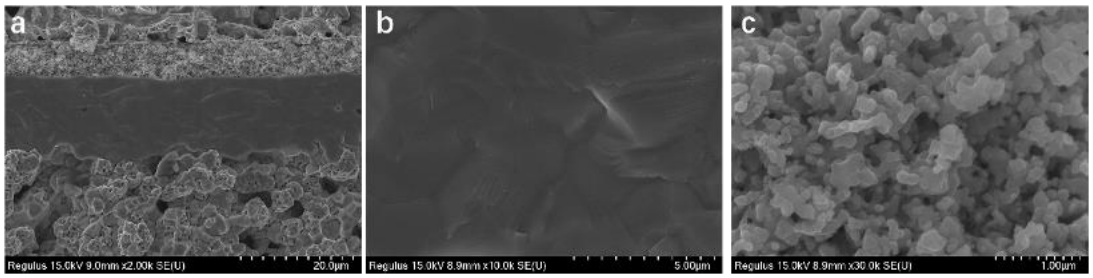

Figure 72. SEM characterization results of cell 6 after testing. (a) SEM image of the sandwiched cross-section of the cell, (b) high-magnification SEM image of electrolyte, and (c) high-magnification SEM image of the cathode.

h) PCES single cell made by two-step laser sintering with infiltrated active cathode

Multi-step laser sintering was investigated for manufacturing PCES single cells. Two cells with excellent performance were reported in the last quarter. Typically, we co-sintered BCZYYb+NiO/BCZYYb half cell by laser in the first step, then a thin layer of BCZY63 scaffold was deposited on the sintered BCZYYb electrolyte surface. And laser was applied on the samples again after tens of minutes of drying. The ideal sandwich structure with porous anode layer, dense electrolyte layer, and cathode scaffold layer was obtained, which is shown in **Figure 73a**. The scaffold layer formed a robust interface with the electrolyte (**Figure 73b**). The BCZY63 grains at the interface are fully dense and integrated with electrolytes without significant boundary. In contrast, the grains far from the interface are porous with lots of 0.5-1 μm pores (**Figure 73c**). Because there is 30wt% starch in the green scaffold layer, which burned in the second time laser sintering process and left big pores that directly made part of the laser irradiation exposed to the electrolyte, this part of laser energy was absorbed by electrolytes and made another heat source for scaffold sintering. That is why the grains near the interface have higher densification. Then BCFZY0.1 cathode precursor solution was infiltrated into the laser-sintered scaffold. Finally, the sample was treated in a furnace at 900^{o}C for 5hrs. The BCFZY0.1 nanoparticles (**Figure 73f**) were found in the inner face of the scaffold everywhere (**Figures 73d** and 7**3e**).

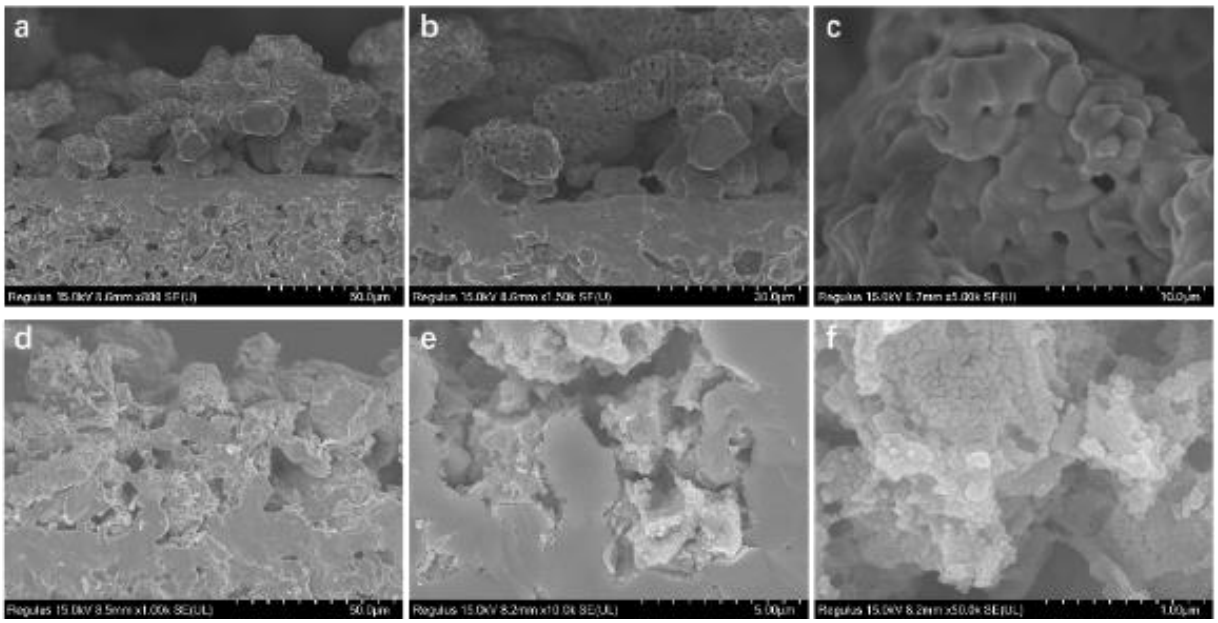

Figure 73. SEM characterization results of multi-step sintered PCES single cells. (a) SEM image of the cross-section of sandwiched single cells, (b) high magnification SEM with detailed information of the interface between cathode scaffold and electrolyte, (c) high magnification SEM image of the cathode scaffold, (d) SEM image of infiltrated cathode on electrolyte, (e) high magnification SEM image of the cathode to show active BCFZY phase in the pores, and (f) high magnification SEM image of the active BCFZY grains.

Cell 7 (0.42 cm^2 effective area) was fabricated with a two-step laser co-sintering method and infiltrated the cathode. This cell demonstrated the best performance of the laser sintering cell, shown in **Figure 74**. The peak power densities of this cell at 700 ^{o}C, 650 ^{o}C, 600 ^{o}C, 550 ^{o}C, and 500 ^{o}C are 1111 mW/cm^2, 975 mW/cm^2, 797 mW/cm^2, 613 mW/cm^2, and 410 mW/cm^2,

respectively. Corresponding OCVs are 1.039 V, 1.072 V, 1.101 V, 1.126 V, and 1.144 V, respectively. High OCVs indicate that the ceramic samples can be sintered multiple times by laser without cracks. The morphology of the cell is shown in **Figure 74b**. Based on the ionic ASR and electrolyte thickness, the conductivity at 600 °C was calculated to be around 0.71×10^{-2} $\Omega^{-1}cm^{-1}$.

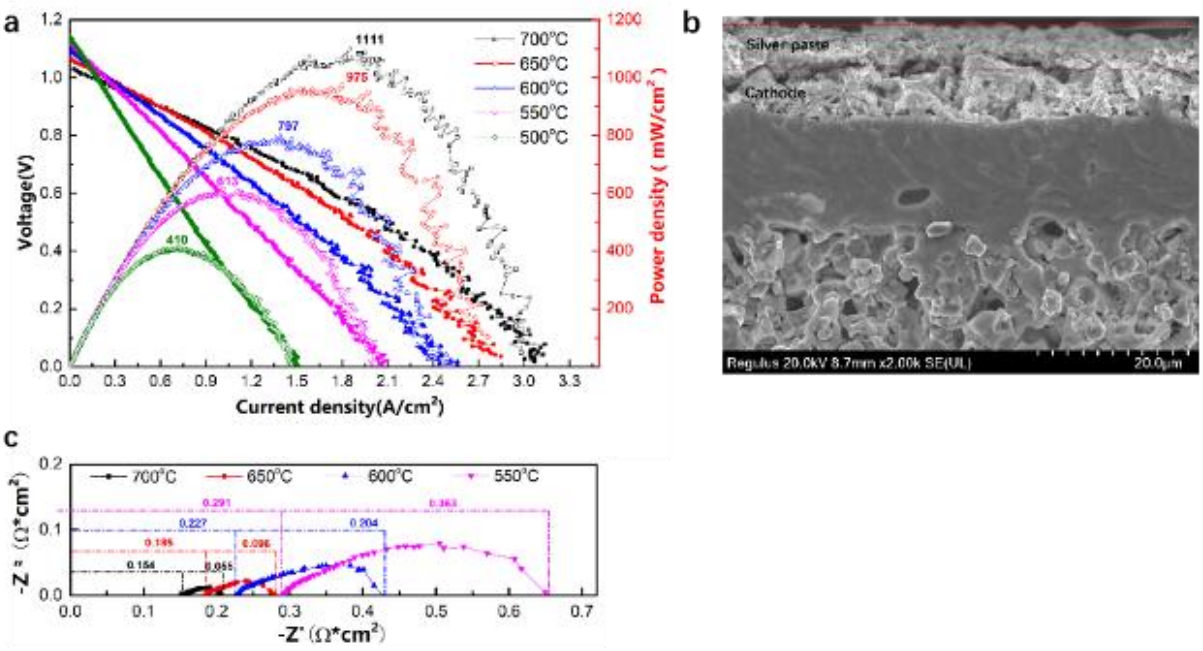

Figure 74. Testing and characterization results of cell 7. a) I-V and I-P curves at 500-700 °C under H_2/air gradient, (b) SEM image of cell cross-section, and (c) EIS Nyquist plots of cell 1 at open circuit condition at 550-700 °C under an H_2/air gradient.

We have obtained the fuel cell stability of this type of cell. Cell 8, with an effective area of 0.29 cm^2, was tested at 550 °C at a constant current density of 275 mA/cm^2 (**Figure 75a**). The terminal voltage was very stable within 100 h, slightly decreasing from 0.665 V to 0.634 V. The ohmic resistance is stabilized at around 0.36-0.39 Ωcm^2, and polarization resistance is slightly decreased from 1.11 to 0.96 Ωcm^2 (**Figure 75b**), which may have caused the cell power density to increase in such a process. But because the OCV of cell 8 decreased from 1.067 to 1.01V, the peak power density decreased from 0.183 W/cm^{-2} to 0.174 W/cm^{-2} (degradation: 4.9% per 100 h).

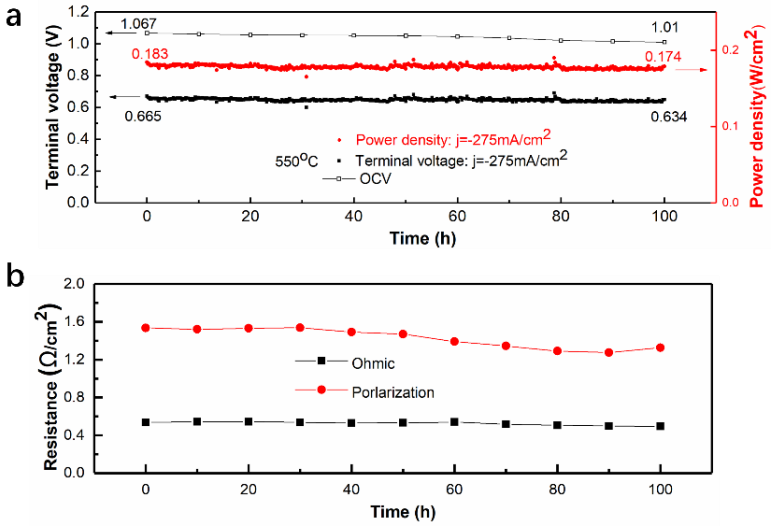

Figure 75. Long-term electrolysis testing of cell 8. (a) Terminal voltage, OCV, power density versus operating time at 550°C under a constant current density of 275 mA/cm^2, (b) the ohmic and polarization resistance versus operating time under the same conditions.

i) PCES single cells made by complete laser processing without any post-treatment

We not only tried to fabricate PCES single cells using a multi-step laser sintering method to fabricate half cells and cathode scaffold followed by the infiltration of active cathode phase but also tried to fabricate single cells with all components being processed by laser. We prepared half-cells using the rapid laser reactive sintering procedure. Then we deposited cathode BCFZY0.1 (rather than scaffold) on the laser-sintered half cell and laser-sintered the cathode layer. We don't have a cathode scaffold, infiltration of the active phase, and the followed anneal. The two-time laser sintering resulted in the final single cells. Cell 9 is an all-laser sintered cell with a 0.37cm^2 effective area. The performance is shown in **Figure 76**. The peak power density of this cell at 700°C, 650°C, 600°C, and 550°C are 502 mW/cm^2, 290 mW/cm^2, 215 mW/cm^2, and 160 mW/cm^2, respectively. It is not high as other laser-sintered cells. The polarization is much bigger than those cells (**Figure 76b**). The morphology of the laser-sintered cathode is shown in **Figure 76c**. The porous cathode with BCFZY0.1 nanoparticles looks similar to the furnace-sintered cathode. But it doesn't form a robust interface with the electrolyte (**Figure 76d**). Only a few particles are bonded with the electrolyte directly. The parameter of the laser for cathode sintering needs to be optimized continually.

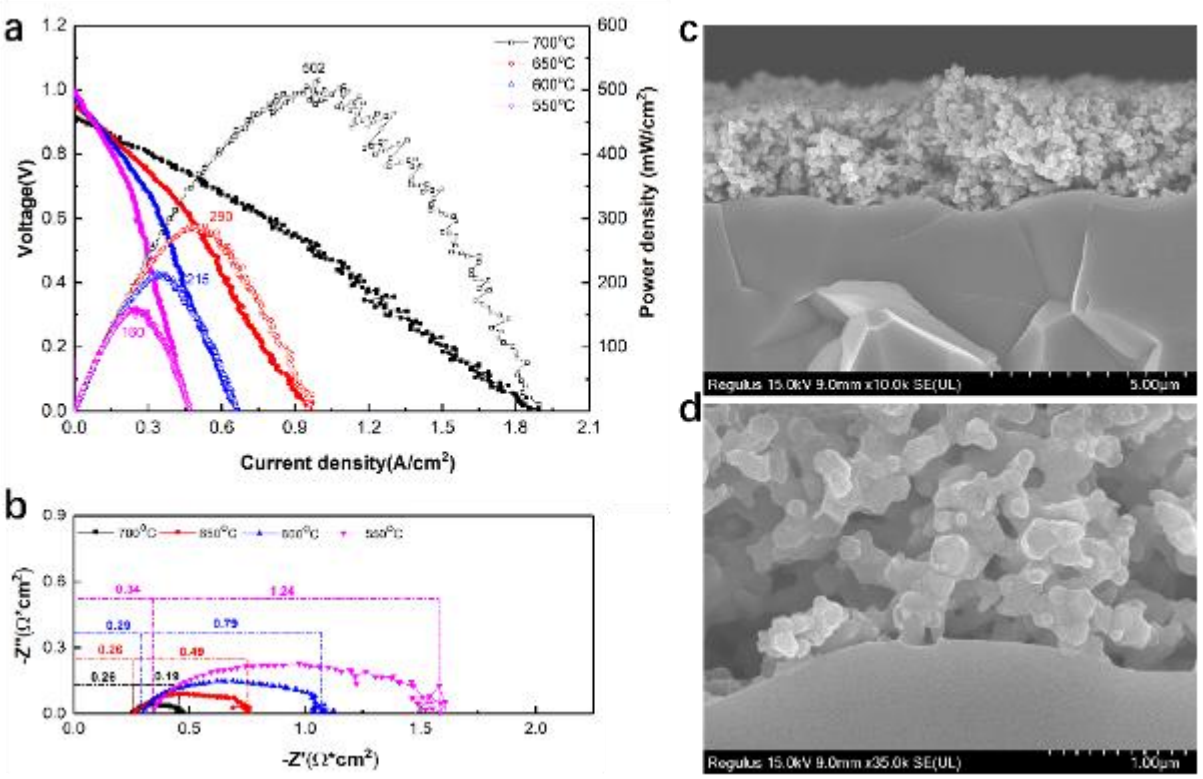

Figure 76. Performance and characterization of cell 9. (a) I-V and I-P curves at 550-700 °C under an H_2/air gradient, (b) EIS Nyquist plots at 550-700°C and open circuit condition under an H_2/air, (c) SEM image of cathode and electrolyte cross-section, and (d) high-magnification SEM image of the cathode.

Cell 10 is an all-laser sintered cell with a 0.42 cm^2 effective area. The performance is shown in **Figure 77**. The m power density of this cell at 700 °C, 650 °C, 600 °C, 550 °C, 500 °C, 450 °C and 400 °C are 1010 mW/cm^2, 754 mW/cm^2, 594 mW/cm^2, 451 mW/cm^2, 315 mW/cm^2, 197 mW/cm^2, and 103 mW/cm^2, respectively. It is comparable with those cell cathodes sintered by furnaces. The correspondingly low polarization resistances were also achieved. The polarization ASR as low as 0.054 Ωcm^2 was obtained at 700 °C. The morphology of cell 10 after testing is shown in **Figures 77c-e**. The porous cathode with BCFZY0.1 nanoparticles looks similar to the furnace-sintered cathode. The particle size is around 100-400 nm. The cathode bonded very well with the sintered electrolyte (**Figure 77d**).

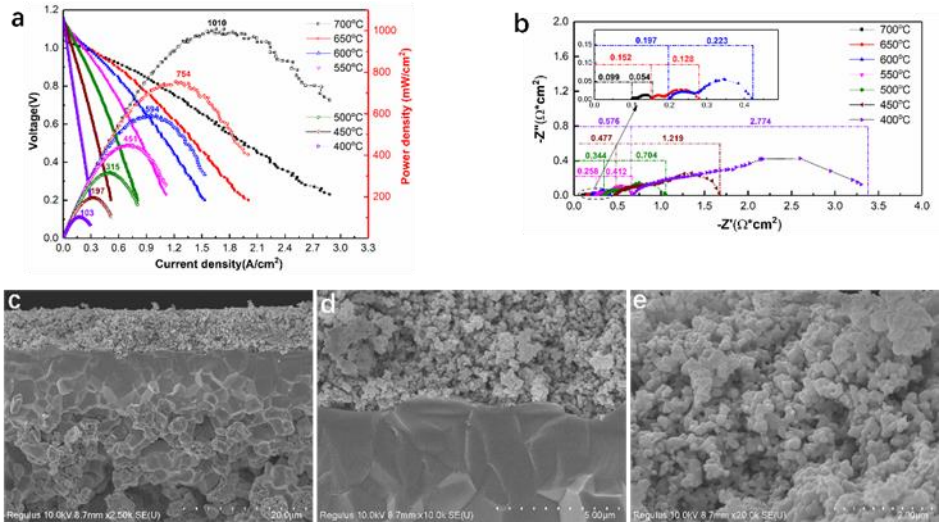

Figure 77. Performance and morphology of cell 10.

The cathode sintering condition was further optimized for the complete laser processing of PCES single cells. A big area laser sintered anode/electrolyte/cathode cell 11 with an effective area of 1.11 cm^2 was obtained. The performance is shown in **Figure 78**. The max power density of this cell at 700 ºC, 650 ºC, 600 ºC, 550 ºC, and 500 ºC are 949 mW/cm^2, 788 mW/cm^2, 633 mW/cm^2, 472 mW/cm^2, and 303 mW/cm^2, respectively. It is comparable with cell 10, even though its area increased almost 2 times. The polarization resistance of cell 11 is also similar to cell 10 (0.062 Ωcm^2 at 700º C). The morphology of the laser-sintered cathode is shown in **Figure 78c-e**. A robust electrolyte/cathode interface was formed (**Figure 78d**).

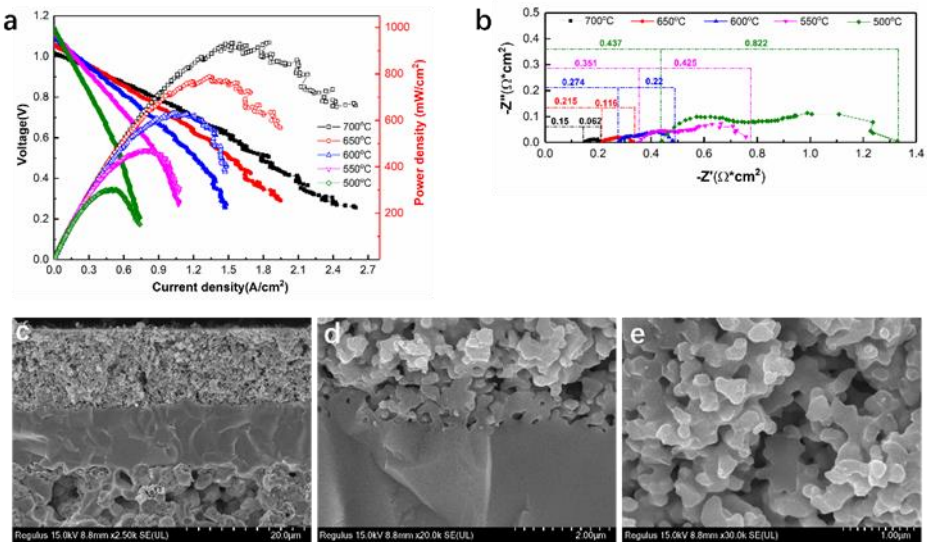

Figure 78. Performance and morphology of cell 11.

Cell 11 was also tested the stability at 600 ºC, and the performance is demonstrated in **Figure 79**. 500 mA/cm^2 current density was applied for long-term stability testing. The terminal voltage is almost stable at 0.76 V (degradation rate: 1.7% per 100 h). The cell was shut down at 92 h

because of the shortage of pure hydrogen gas in the Christmas holiday (without gas delivery). The OCV was stabilized at 1.083-1.093V, corresponding ohmic resistance was stabilized at 0.286-0.297 Ωcm^2. The polarization resistance was increased from 0.303 to 0.369 Ωcm^2 in the first 20hrs and then stabilized at 0.369-0.378 Ωcm^2 in the next 72 h.

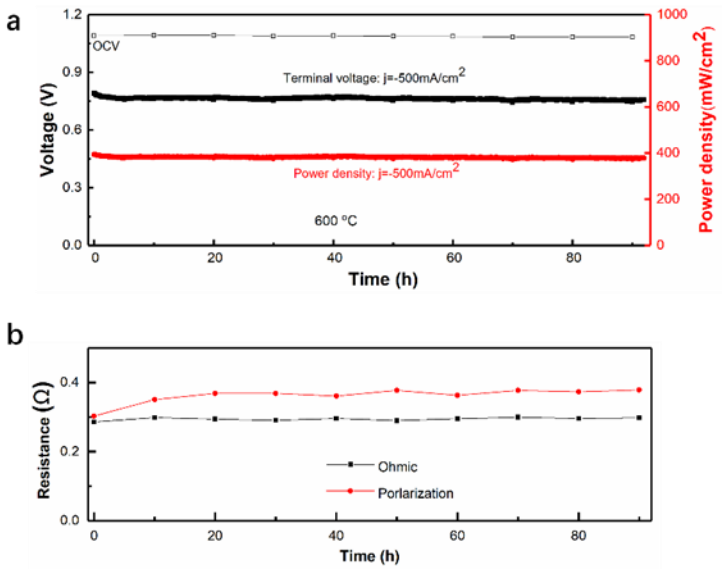

Figure 79. The stability of cell 2 at 600 ^oC under Air/H^2. a) Terminal voltage and power density versus the operation time, b) Ohmic resistance and polarization resistance versus the operation time.

We have been focusing on increasing the effective area of PCES single cells and the manufacturing repeatability when using the RLRS technique. **Figure 81a** summarizes the photos of nine half cells manufactured by two-step Galvo laser scanning processes. All the half cells are straight and flat. The effective area of a single piece of half cells can be as large as $10cm^2$. The area is limited to the substrate dimension rather than the manufacturing capability. It is possible to make half cells with an area near 20 cm^2.

We manufactured the single cells by introducing cathode layers using three methods: 1) furnace annealing, 2) laser-firing scaffold followed by infiltration, and 3) direct laser firing. **Figures 81b, 81c**, and **81c** provide the SEM images of the cross-section of the single cells, indicating excellent bonding between cathode and electrolyte and excellent cathode porous structure. Therefore, we can conclude that the repeatable PCES single cells can be successfully manufactured using the L3DP technique.

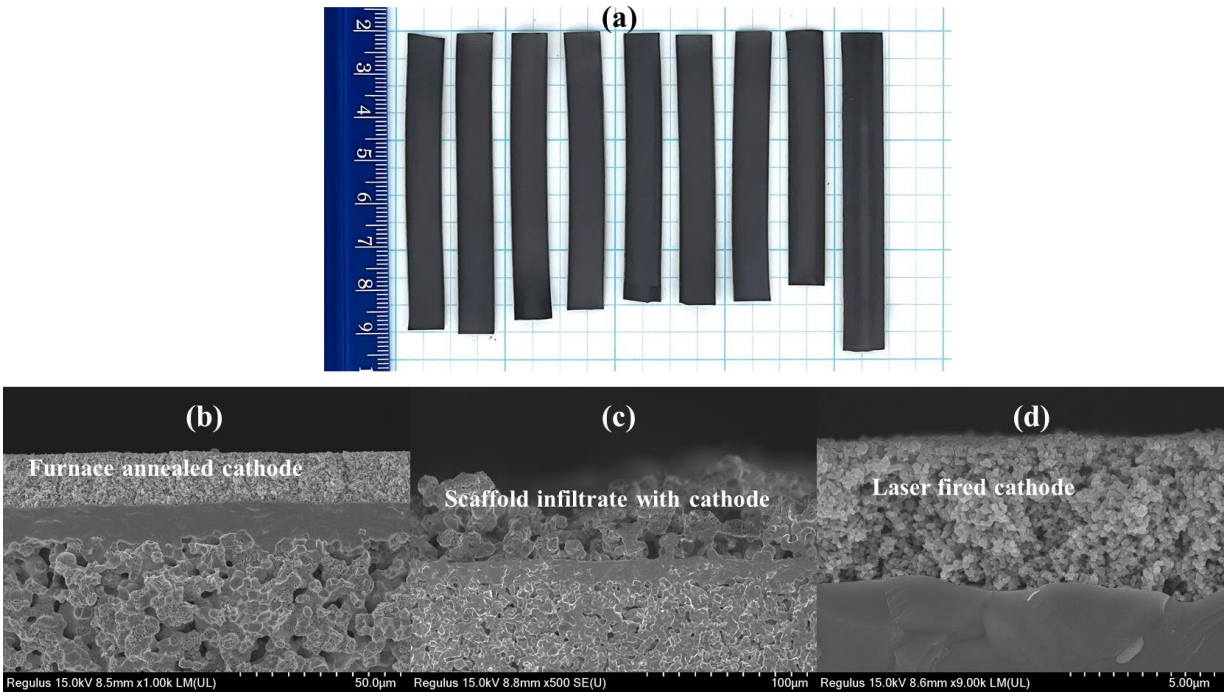

Figure 81. Summary of PCES cells fabricated by L3DP. Photo of half cells fabricated Galvo laser scanning a) and SEM images of the cross-sections of single cells with furnace annealed cathode (b), laser fired scaffold and infiltrated cathode, and (c) direct laser fired cathode.

Milestone 4.3 Based on ST-4.3 Performance and Stability Test

Milestone-4.3 is based on ST-4.3 Peformance and Stability Test. PCES manufactured by the proposed L3DP technology should have more than 5 cells with a total area >100 cm^2. The current density at 1.3 V should be higher than 1 $A/cm^{2,}$ and the degradation rate should be lower than <1% per 1000 h at 600 ^oC. We fabricate PCES by L3DP and test the water electrolysis at 350^{o}C-650^{o}C under different voltages. The PCES evaluation includes the current density, hydrogen production rate, Faraday efficiency of the stack, and long-term stability under constant voltage at 600^{o}C. The thermal cycle stability is tested by rapidly changing temperatures between 300-600^{o}C. After the performance and stability test, the stack is characterized in detail for component layers and their interfaces by SEM, TEM, XRD, XPS, and Raman microscopy. Based on the following results, we claim we have reached 95% completion of this milestone.

3-Cell Segmented in Series (SIS) Stacks

Single-cell fabrication: The BCZYYb+NiO anode precursor paste was 3D printed onto a substrate (fused silica) with a thickness of 0.5 mm and dried at room temperature. Then the BCZYYb electrolyte precursor slurry was spray-coated on the anode by spray coating and dried at room temperature. Finally, the CO_2 laser with a cylindrical lens was applied to the anode/electrolyte half-cell green film for sintering. Laser operation with 0.1mm/s scan speed, 150-180W power density, and 30mm defocus distance. The BCFZY0.1 cathode precursor paste was screen-printed on the sinter BCZYYb half-cell surface, then sintered at 900 ^oC for 5 h by a furnace. As described in **Figure 82,** the three cells were arranged side by side, and silver wire was connected with the anode and cathode to form an SIS stack.

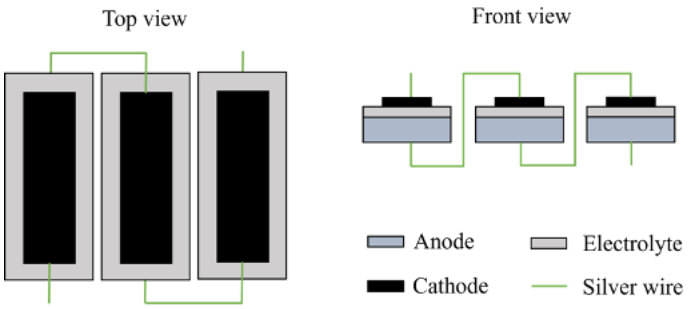

Figure 82. Schematic of the protonic ceramic segment-in-series stack

Performance testing of 3-cell SIS stacks

The picture of Stack 1 is shown in **Figure 83a**, which was sealed on the alumina tube testing set by ceramic bond. Because of the limitation of the tube's inner diameter (around 4.5cm), the cell could not select a very large size to control the effective area of each cell to the same size. The effective area of the three cells in stack 1 is 0.89, 1.00, and 1.06cm^2, respectively. The performance of Stack 1 is shown in **Figure 83b**. The stack bundle produces 2.95, 3.07, 3.14 V OCV and reaches 1334, 1009, 820 mW maximum power at 650, 600, 550 ^{o}C, respectively. The average OCV produced by each stack cell is slightly lower than the individual single cells (~1.00 V) in Figure 1. The peak power density of the stack with normalized to the total electrode area reaches 499 mW/cm^2, 378 mW/cm^2, 307 mW/cm^2 at 650 ^{o}C, 600 ^{o}C and 550 ^{o}C, respectively. The electrolyte thickness of each cell in the stack is around 15 μm (**Figure 83c**) which is the same as cell 1. The ASR of the stack is shown in **Figure 83d**, which is bigger than that of cell 1 at each temperature. We attribute to the silver gauze (or silver wire) that contact resistance between each cell can not be eliminated for the ohmic resistance to increase. And polarization part attributes to the stress applied by silver gauze to the cathode in the cells bundle process, which causes the cathode delamination issue. The delamination issue is becoming increasingly obvious in the test sequence of temperatures from 550 to 600 ^{o}C. That is why the ohmic resistance of 600 ^{o}C is bigger than that of 550 ^{o}C. That is the reason the stack demonstrated lower conductive (~0.4×10^{-2} Ω^{-1}cm^{-1}at 600 ^{o}C) and lower power density than that of cell 1.

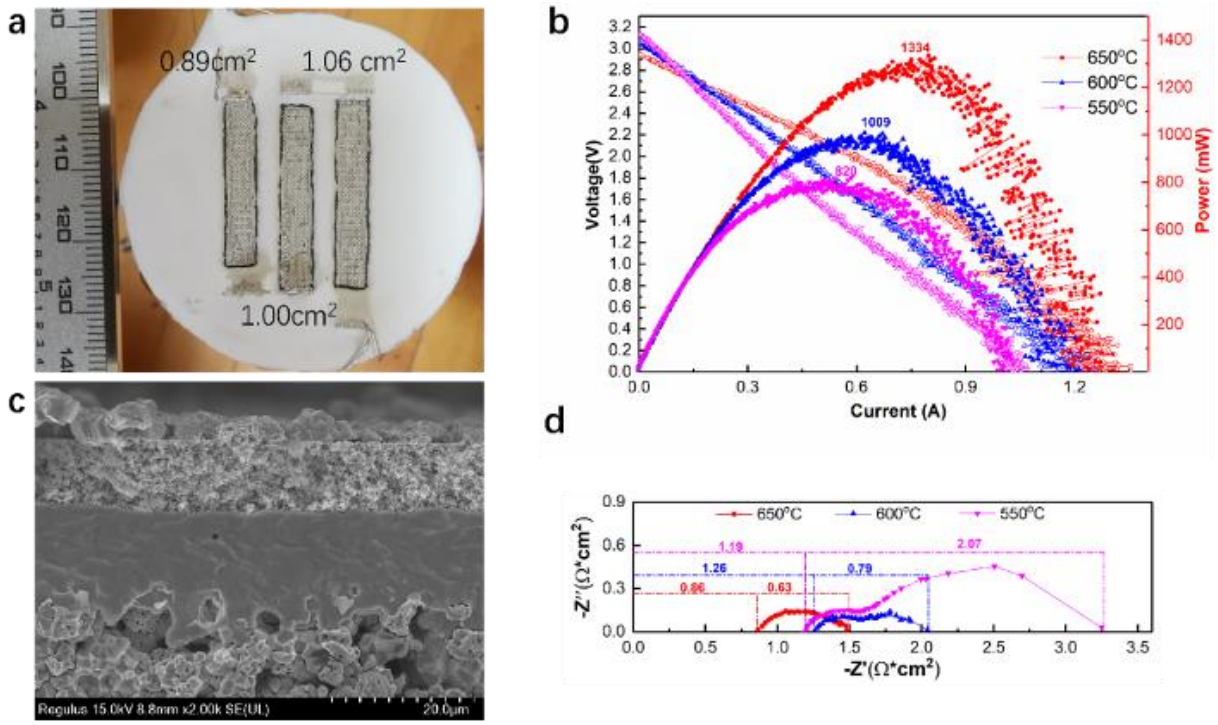

Figure 83. Performance and characterization of stack 1. (a) Photo of the stack, (b) I-V and I-P curves at 550-650°C under H_2/air gradient, (c) SEM image of the cross-section of a single cell consisted of the stack, and (d) EIS Nyquist plot at 550-650°C and open circuit condition under H_2/air gradient.

A new protonic ceramic stack (stack 2) was constructed in-segments series with three of the laser-sintered cell. The stack picture is shown in **Figure 84a**, which was sealed on the alumina tube testing set by ceramic bond. Because of the limitation of the tube inner diameter (around 4.5 cm), to control the effective area of each cell to the same size, the cell could not select an enormous size. The effective area of the three cells in the stack is 0.986 (cell 1), 1.016 (cell 2), and 1.004 (cell 3) cm^2, respectively. The performance of the stack is shown in **Figure 84b**. The stack bundle produces 3.203, 3.312, 3.395 V OCV and reaches 2627, 2304, 1703mW maximum power at 650, 600, 550 °C, respectively. The average OCV produced by each stack cell is comparable to individual single cells. The maximum power density of the stack normalized to the total electrode area reaches 888 mW/cm^2, 779 mW/cm^2, and 576 mW/cm^2 at 650 °C, 600 °C and 550 °C, respectively. The EIS of the stack is shown in **Figure 84c**. The ohmic resistance (0.651 Ω) at 650 °C is almost the same as that (0.646 Ω) at 600 °C. The testing sequence of the temperature of this stack was from 550 to 650 °C, and the contact resistance between each cell or silver wire was increased in the temperature ramp process from 600-650 °C. That is why the ohmic resistance of 600 °C is bigger than that of 550 °C. The electrolyte thickness of each cell in the stack is around 12um (**Figure 84d**). Based on the electrolyte thicknesses and the EIS results, the electrolyte conductivity at 600°C was calculated to be ~0.56×10^{-2} $\Omega^{-1}cm^{-1}$.

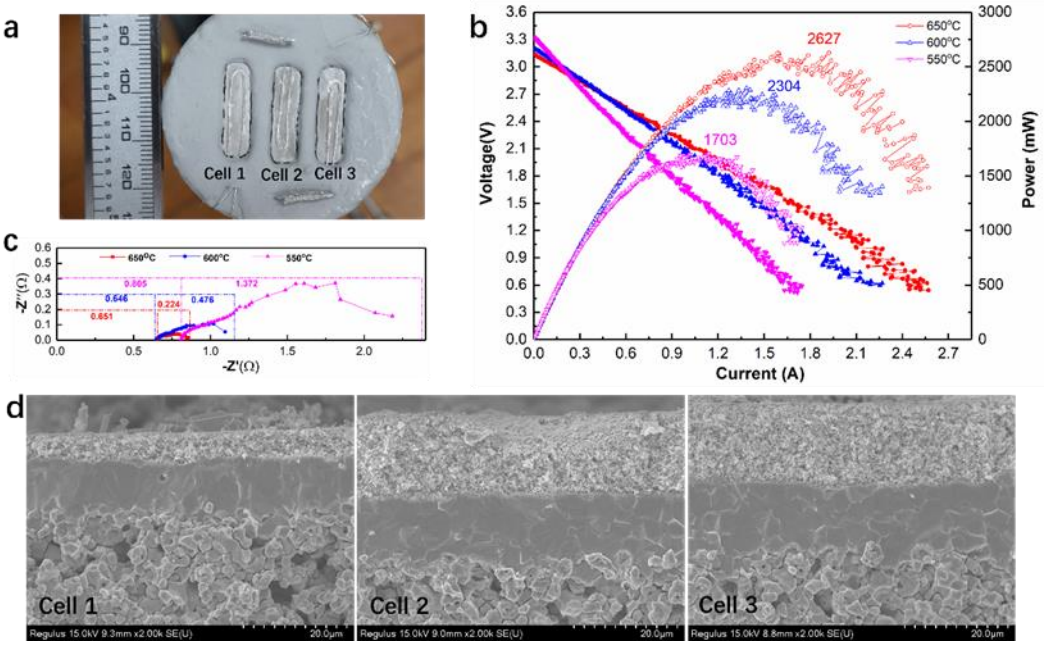

Figure 84. Performance and morphology of the 3-cell SIS stack (stack 2) under Air/H_2. a) Photo of the SIS stack before testing, b) I-V and I-P curves of the stack, c) EIS Nyquist plot of the stack, and d) SEM images of the cross-sections of the three cells.

The stack was reduced to 550 ^oC and operated at a constant current density for long-term stability, shown in **Figure 85**. The stack's operation voltage and power under H_2/air while keeping a constant current density of 200 mA cm^{-2} were recorded in the first 200 h (**Figure 85a**). The operation voltage did not show apparent degradation, and the corresponding power of the stack was around 510 mW. Then the stack was operated for another 60 h under an increased current density of 300 mA cm^{-2}. The operation voltage slightly decreased during the 60 h. The corresponding power of the stack was kept around 630 mW. Both the ohmic and polarization resistance did not show an apparent increase during the whole 260 h (**Figure 85b**), indicating that the stack has good stability.

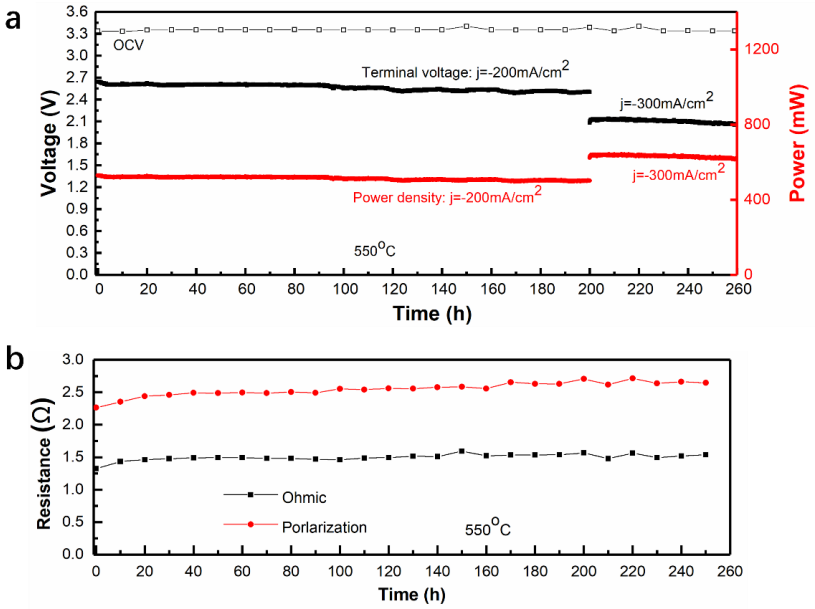

Figure 85. The stability of the 3-cell SIS stack (stack 2) at 550 ºC under Air/H_2. a) terminal voltage and operation power versus operation time, b) the ohmic resistance and polarization resistance versus operation time.

A new SIS PCES stack (stack 3) of seven laser-sintered cells was constructed and sealed on a new test set by ceramic bond. Due to the limitation of the alumina tube diameter (around 3 cm), the length of each cell is around 2.8 cm. The stack picture is shown in **Figure 86c**. The effective areas of the seven cells in the stack are 1.263 (cell 1), 1.296(cell 2), 1.313 (cell 3), 1.378 (cell 4), 1.345 (cell 5), 1.299 (cell 6), and 1.39 (cell 7) cm^2, respectively. The performance of the stack is shown in **Figure 86a**. The stack produces OCVs of 7.072, 7.389, 7.401, 7.629 V OCV and maximum powers of 7157, 5728, 3887, and 2071 mW at 650, 600, 550, and 500 ºC, respectively. The average OCV produced by each cell is comparable to individual single cells. The maximum power density of the stack with normalized to the total electrode area reaches 810 mW/cm^2, 648 mW/cm^2, 440 mW/cm^2, 234 mW/cm^2 at 650 ºC, 600 ºC, 550 ºC and 500 ºC, respectively. The ohmic and electrode resistances of the stack are shown in **Figure 86b**. The average electrolyte ASRs are around 0.125, 0.17, 0.22, and 0.262 $\Omega \cdot cm^2$ at 650 ºC, 600 ºC, 550 ºC, and 500 ºC, respectively. And corresponding electrode ASRs are 0.102, 0.222, 0.4and 53, 0.834 $\Omega \cdot cm^2$, comparable to single cells. **Figure 86d** shows the photo of the stack after testing. Although cell1 and cell7 show tiny cracks, all other cells are perfect, indicating the good stability of the stack.

The SEM images of the cross-sections of each stack cell are shown in **Figure 87**. All the cells show a well-bonded three-layer structure. The electrolyte layers are fully densified and almost grain boundary-free. The thickness of the electrolyte layer in the individual single cells is around 7-15 μm, and the total electrolyte thickness of the stack is around 74um. Combined with the EIS result, the proton conductivity of 600ºC is ~6.21×10^{-3} $\Omega^{-1}cm^{-1}$.

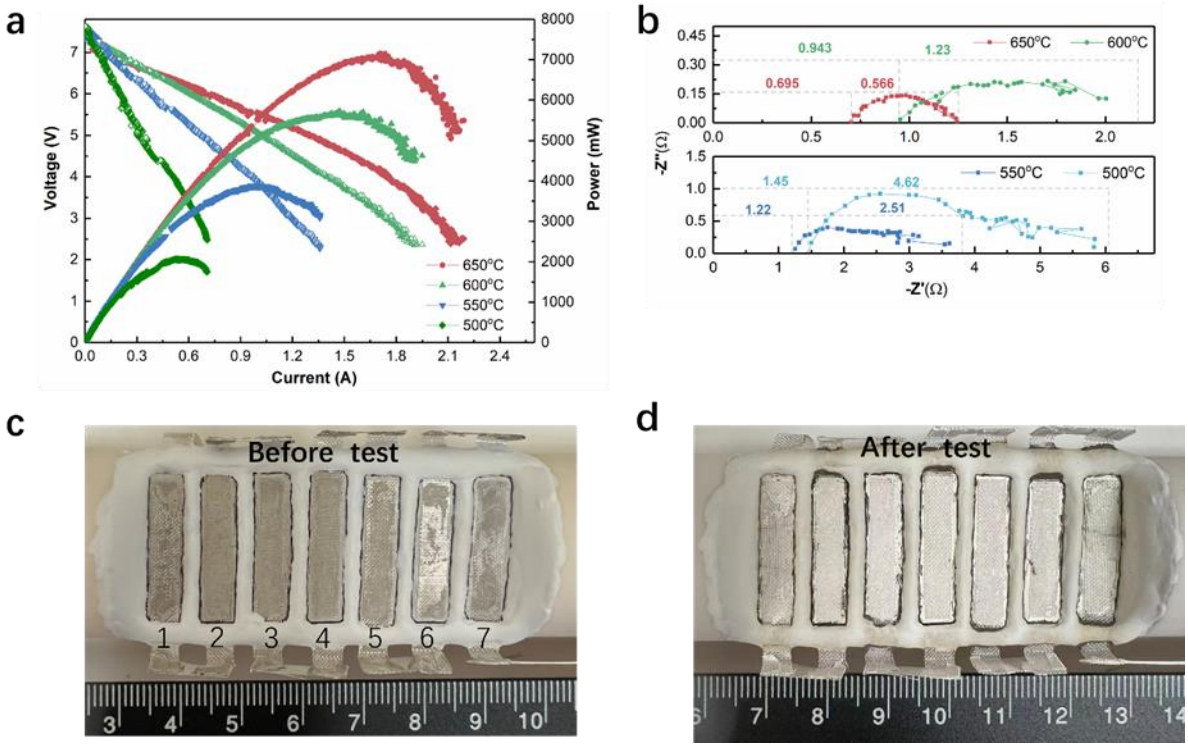

Figure 86. Performance and photos of stack 3. a) current vs. voltage and current vs. power, b) electrochemical impedance spectroscopy characterization, c) stack photo before testing and d) stack photo after testing.

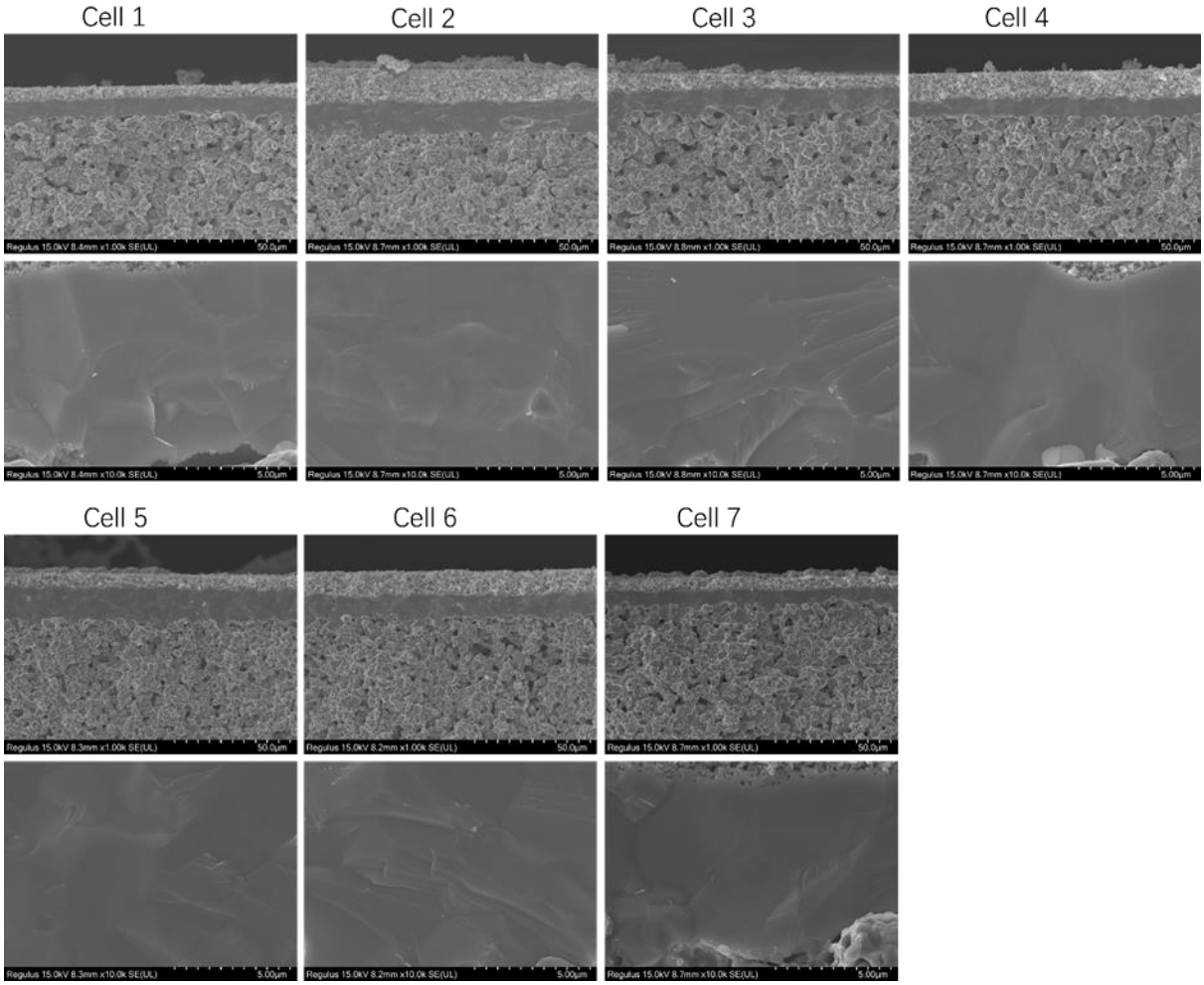

Figure 87. SEM images of the cross-sections of each cell of stack 3.

Another stack (stack 4) consisting of 3 big area cells was fabricated and tested this quarter. The length of each cell is around 5cm, and the effective areas are 3.04, 2.8, and 2.86 cm^2, respectively. The performance and pictures of the stack are shown in **Figure 88a**. The stack's maximum powers are 6931, 5910, 4196, and 2365mW at 650, 600, 550, and 500 ^oC, while the corresponding OCVs are 2.964, 3.107, 3.206, and 3.28V. The maximum power density of the stack normalized to the total electrode area reaches 825 mW/cm^2, 704 mW/cm^2, 500 mW/cm^2, 281 mW/cm^2 at 650 ^oC, 600 ^oC, 550 ^oC, and 500 ^oC, respectively, which are a little bit higher than the 7 cells stack. The ohmic and electrode resistances of the stack are shown in **Figure 88b**. The average electrolyte ASRs are around 0.133, 0.179, 0.249, and 0.308 $\Omega \cdot cm^2$ at 650 ^oC, 600 ^oC, 550 ^oC, and 500 ^oC, respectively. And corresponding electrode ASRs are 0.051, 0.111, 0.329, 1.003 $\Omega \cdot cm^2$. The stack demonstrated a similar performance as the previous stack.

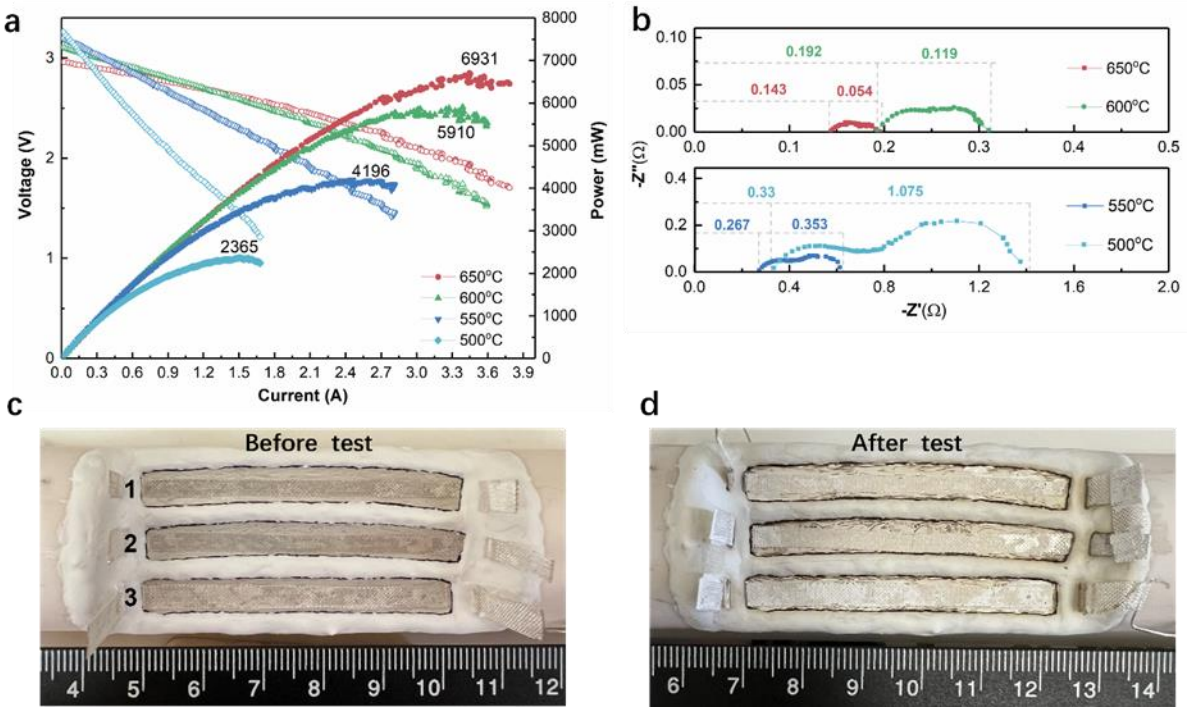

Figure 88. Performance and photos of stack 4. a) current vs. voltage and current vs. power, b) electrochemical impedance spectroscopy characterization, c) stack photo before testing, and d) stack photo after testing.

The stack was stabilized at 600 °C and operated at a constant current density for long-term stability. **Figure 89** indicates that the stack's operation voltage and power density under H_2/air with 500 mA cm^{-2} current density are demonstrated, and the operation voltage is slightly decreased in the 200hrs. The corresponding power of the stack is decreased from 3300-2800 mW. Both ohmic and polarization resistance increase from 0.213 to 0.418 Ω and 0.205 to 0.437 Ω, respectively. However, the OCV of the stack is permanently stabilized at around 3.15V. It means the laser-sintered method for cell fabrication has promising applications. The stack cells looked great after testing. No obvious cracks were found in each cell.

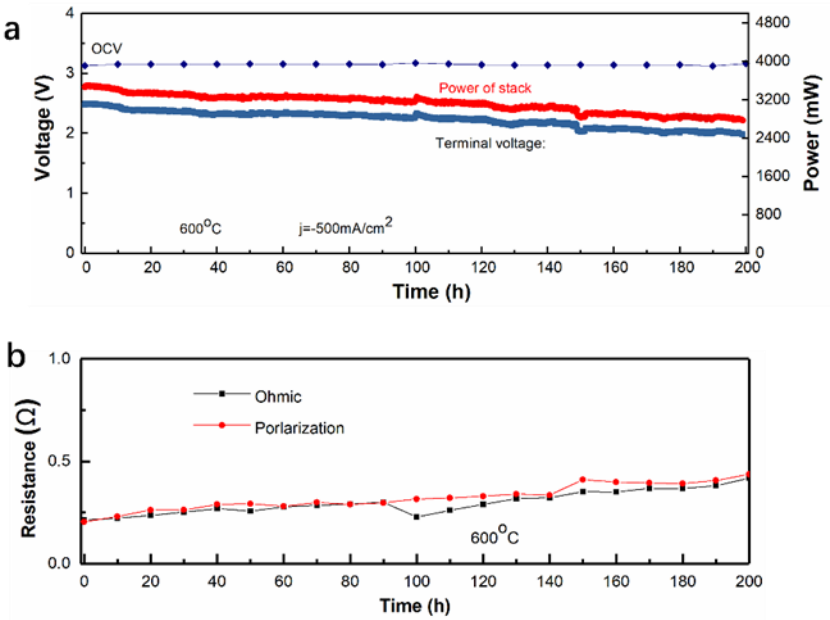

Figure 89. Stability of the stack 4. a) power and OCV versus operation time and b) Ohmic and polarization resistances versus operation time.

The cross-section sem image of each cell of stack 4 is shown in **Figure 90**. The grain boundary-free electrolyte layer was obtained in each cell. The electrolyte thickness is around 7-12 μm, and the total electrolyte thickness of the stack is around 30 μm. Based on the EIS result of **Figure 88b**, we calculated the conductivity at 600 °C is ~6×10^{-3} $\Omega^{-1}cm^{-1}$.

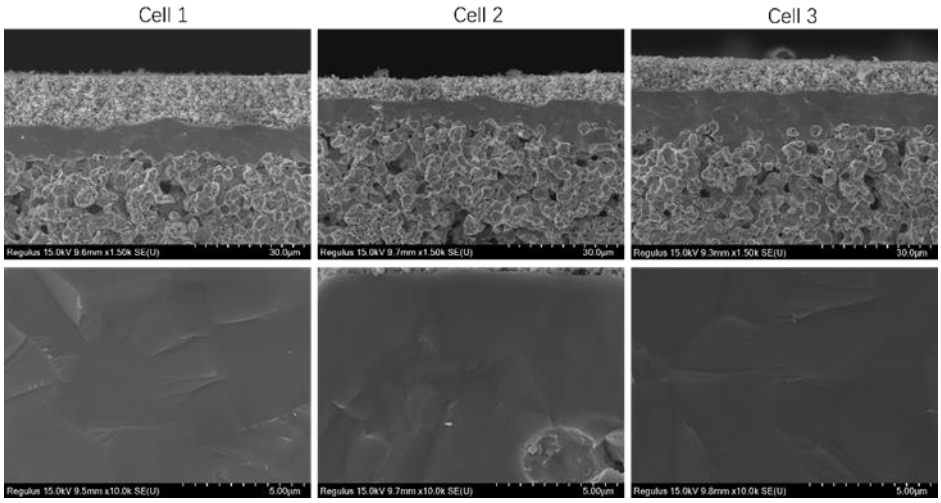

Figure 90. SEM images of the cross-sections of each cell of stack 4.

We achieved significant progress. Two new stacks were obtained and measured with our new test set. One is 7 cells stack with a 9.23 cm^2 total effective area. The other one is 3 cells stack with an 8.7 cm^2 total effective area. Both stacks demonstrate excellent performance, the maximum power of the stacks reached to 7157 mW and 6931 mQ at 650 °C. The corresponding peak power densities are 810 mW/cm^2 and 825 mW/cm^2, respectively. It is comparable to the single cell. Stack 2 operated stably with 500 mA/cm^2 current density at 600 °C over 200 h, indicating that L3DP is one of the promising fabrication methods

We tried to fabricate large-area cells during the last month of the project within the capability of our current in-house laser 3D printer. We could fabricate half and single-cells with an area of around 14 cm^2 (**Figure 90a**). The length of the cells could be longer, while the width of cells needs to be enhanced using higher laser power. The homogenous, fully dense electrolyte can easily be controlled with a thickness of less than 10 μm (**Figure 90b**). The cathode layer can be quickly introduced by spray-coating followed by annealing or laser sintering. Therefore, the feasibility of manufacturing large-area cells and stacks was proved.

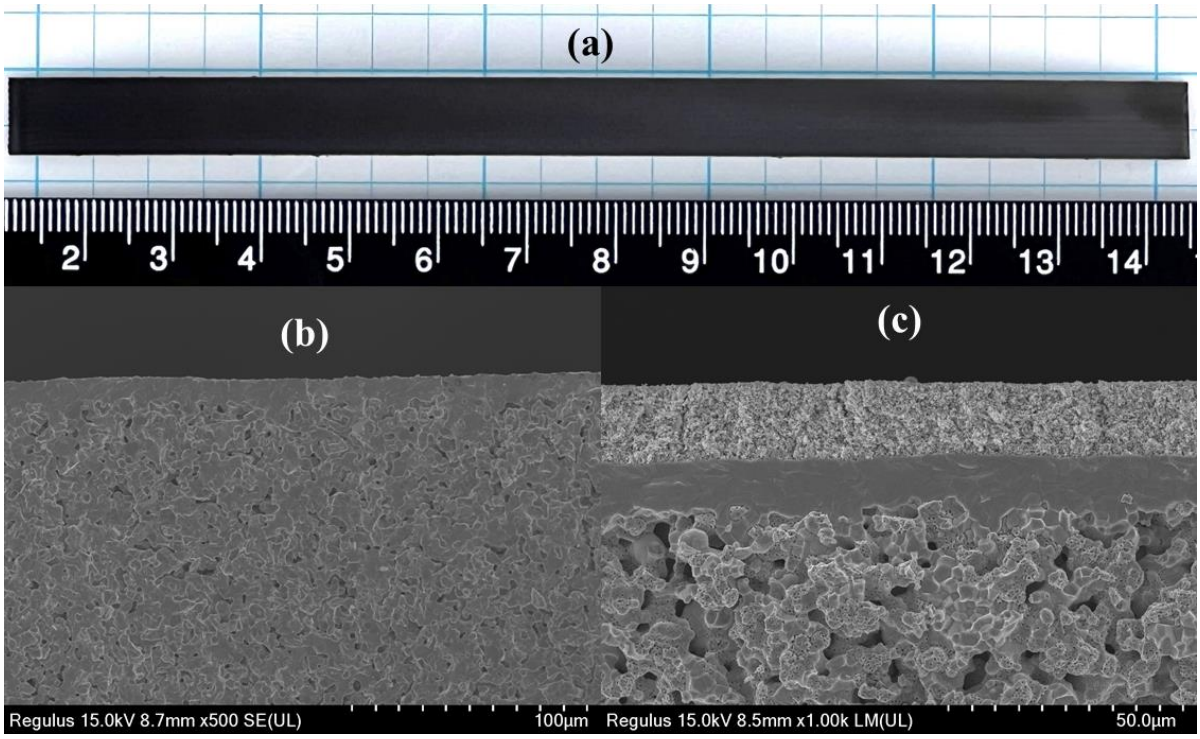

Figure 90. Large-area half-cells and single-cells prepared by laser 3D printing method. (a) photo of a half-cell, (b) SEM image of the cross-section of a half-cell, and (c) SEM image of the cross-section of a single-cell.

Task-5 Initial TEA and Market Transformation Plan

Milestone Based on ST-5.1 Initial TEA

This task estimates PCES investment by analyzing the materials cost, paste preparation cost, 3D printing cost, heat efficiency, and laser processing cost. The scale effect on the electrolyzer cost based on the effective working area should be estimated and compared with other manufacturing technologies. The electrolyzer performance, stability, and operating cost were also analyzed the hydrogen production cost using the H2A tool.

Milestone-5.1. Establish the models for estimating the electrolyzer manufacturing cost by L3DP technology for predicting H_2 cost by H2A. Identify the critical parameters for further decreasing H_2 cost to meet DOE's target of \$2/kg H_2.

We have reached **100%** completion of this milestone in the previous quarter.

1) Mass of hydrogen generated per day of L3DP fabricated cell

According to Faraday's Law, the relationship between the amount of reaction and the current is shown in the following formula:

$$m=\frac{I\bullet t\bullet M_H\bullet FE}{n\bullet F} \quad (1)$$

Where m is the mass of hydrogen generated; I is the current (amps), t is the time (seconds); MH is the molar mass of hydrogen; FE is the Faradaic efficiency of the electrolysis cell, n is the number of electrons transferred by the reaction, F is the Faraday constant.

So, the hydrogen production per day is:

$$m=\frac{I\times 24\times 3600s\times 2g/mol\times FE}{2\times 96485C/mol}=0.895476\times I\bullet FE \text{ (sg/C)} \quad (2)$$

It means that the higher the current density and Faraday efficiency, the more hydrogen produced on a protonic ceramic electrolysis stack with a fixed effective area.

According to previous report results, the Laser 3D printing (L3DP) PCEC show very high electrochemical performance, the maximum current density reaches 2.27 A/cm^2 with 1.3v applied voltage at 600 ^{o}C. The target of the current density in this program is 1 A/cm^2. Chuancheng Duan et al. have reported that the BCZYYb electrolysis cell demonstrated extremely high Faradaic efficiency at 98.6%.

Based on the 1 A/cm^2 current density and 98.6%Faradaic efficiency, the mass of hydrogen generated per day was estimated according to formula (2)

$$m=\frac{I\times 24\times 3600s\times 2g/mol\times FE}{2\times 96485C/mol}=\frac{\frac{1A}{cm2}\times 24\times 3600s\times\frac{2g}{mol}\times 98.6\%}{2\times 96485C/mol}=0.882939g/\ cm^2$$

2) Usage of industry electrical per kg H_2

Based on this result, the Usage of industry electrical per kg H2 could be estimated as follow:

$$U=1000\frac{i\bullet V\bullet T}{m} \quad (3)$$

Where **m** is the mass of hydrogen generated (g/cm^2); **i** is the current density (A/cm^2), **T** is the time (hours) per day; **V** is the applied voltage at the electrolysis cell.

So, the 2. Usage of industry electrical per kg H_2 is:

$$U=1000\frac{i\bullet V\bullet T}{m}=1000\times\frac{1\ A/cm2\times 24\times 1.3v}{0.882939g/cm2}=35.33653kWh$$

3) Hydrogen cost estimation

T. Ramsden has reported a high-temperature electrolysis base on nuclear reactor technology case of hydrogen production cost estimation by H2A Production Model. The central nuclear energy via case is based on the application of an advanced nuclear plant providing high-efficiency electric power and heat (high-temperature steam) to a central high-temperature electrolysis (HTE) plant. The plant design capacity (kg hydrogen/day) is 816,000 kg hydrogen/day, and the corresponding capital cost is 1,205.7 million (based on 2005), of which the electrolysis stack is 584million. The capital cost is shown in Table 8 below.

Table 8. Capital cost of T. Ramsden case

Capital Costs (million 2005$)		Future
Initial direct	Steam generator/superheater	27.9
	Oxygen recuperator	22.4
	Hydrogen recuperator	24.5
	Sweep heater	7.5
	High-temperature (electric) heater	5.3
	Power recovery system	20.0
	Water supply system	4.0
	Miscellaneous plant equipment	10.0
	Electrolyzer system	584.0
	Total initial direct	*705.6*
Indirect depreciable	Project contingency	141.1
	Other depreciable[a]	141.1
Indirect non-depreciable	Land cost	1.0
	Total indirect	*283.2*
	Total initial (initial direct + indirect)	***988.8***
Expected replacement[b]		216.9
	Total[c]	**1,205.7**

Assume that the electrolysis stack of this nuclear hydrogen plant is fabricated by L3DP technology. Based on the result of mass of hydrogen generated per day of L3DP fabricated cell, the effect area of electrolysis cell with 816,000 kg hydrogen/day capacity can be calculate as follow:

$$A=\frac{816000kg}{0.882939\ g/cm2}=9.24186\times10^{8}\text{cm}^2$$

We have estimated the product costs of a single PCEC at laboratory scale is $2.5327 with 100 cm^2, which in will be lower on an industrial scale. Because the cost only includes materials cost and energy cost of the electrolysis cell, to add labor and other indirect costs, this product cost is multiplied by a coefficient c for rough cost estimation of the electrolysis (C1 unit price/cm^2) of this report as follows. The coefficient is selected as 2 in this report.

$$C_1=c\times\frac{2.5327}{100cm2}=2\times\frac{2.5327\$}{100cm2}=0.050654\$/\text{cm}^2 \qquad (3)$$

So, the capital cost of the electrolysis stack is 46.8 million. the design life of the plant is 40 years, and the life of electrolysis cells in the DOE target is 60000 h. It means that the cells will replace every 6.8 years, so the total cost of the electrolysis stack is 280.8 million. it means that the capital cost will be reduced by 303.2 million if replace the initial electrolyzer stack with our electrolyzer stack fabricated by the L3DP method. The total capital cost is 902.5 million.

The hydrogen cost of T. Ramsden's reported case is $2.93/kg, and the cost results summary is shown in the table below. based on the cost date of this nuclear hydrogen production case, the hydrogen cost with our electrolyzer stack was also calculated. It is 2.75 $/kg hydrogen, which is reduced by 6.5%.

Table 8. Results summary

Cost component	Cost contribution of T. Ramsden case ($/kg hydrogen) [2]	Cost contribution of our electrolyzer stack case ($/kg hydrogen)
Capital cost	0.77	0.58
Fixed O&M	0.22	0.22
Feedstock	1.94	1.94

Other variable	0.01	0.01
Total hydrogen cost	**2.93**	**2.75**

4) L3DP electrolysis cell hydrogen production cost analyst by H2A model V3.2018

The L3DP electrolysis cell hydrogen production cost was analyst by H2A model version 3 refer to the nuclear hydrogen production based on high-temperature steam electrolysis. The input data are shown in Table 9 below.

Table 9. Input data of H2A model

Technical Operating Parameters and Specifications	
Operating Capacity Factor (%)	90.0%
Plant Design Capacity (kg of H2/day)	816,000
Plant Output (kg/day)	734,400
Plant Output (kg/year)	268,056,000
Financial Input Values	
Reference year	2016
Assumed start-up year	2020
Basis year	2016
Length of Construction Period (years)	3
% of Capital Spent in 1st Year of Construction	35%
% of Capital Spent in 2nd Year of Construction	40%
% of Capital Spent in 3rd Year of Construction	25%
% of Capital Spent in 4th Year of Construction	
Start-up Time (years)	1
Plant life (years)	40
Analysis period (years)	40
Depreciation Schedule Length (years)	20
Depreciation Type	MACRS
% Equity Financing	40%
Interest rate on debt, if applicable (%)	3.70%
Debt period (years)	Constant debt
% of Fixed Operating Costs During Start-up (%)	75%
% of Revenues During Start-up (%)	50%
% of Variable Operating Costs During Start-up (%)	75%
Decommissioning costs (% of depreciable capital investment)	10%
Salvage value (% of total capital investment)	10%
Inflation rate (%)	1.9%
After-tax Real IRR (%)	8.0%
State Taxes (%)	6.0%
Federal Taxes (%)	21.0%
Total Tax Rate (%)	25.74%
WORKING CAPITAL (% of the yearly change in operating costs)	15%
Feedstock	
Total Energy Feedstock Cost ($/year)	$639,867,354
Total Energy Utilities Cost ($/year)	$0
Total Energy Byproduct Credit ($/year)	$0
Total Direct Capital Cost	

electrolysis stack	280,795,876	$386,074,452
steam generator/superheater	24,153,560	
oxygen recuperator	19,383,017	
hydrogen recuperator	21,166,598	
sweep heater	6,489,658	
high-temperature (electric) heater	4,598,631	
power recovery system	17,341,568	
water supply system	3,470,463	
miscellaneous plant equipment	8,675,082	
Indirect Depreciable Capital Costs		162151270
Cost of land ($/acre)		55,036.21
Fixed Operating Costs		62,756,514
Variable Operating Costs		4,540,783

This is a roughly hydrogen cost calculation by the H2A model, both the reference year and basis year are 2016. Plant Design Capacity, Direct Capital Cost and labor cost are based on T. Ramsden's result. The cost of the electrolyzer system is the same as the previous calculation, 280.8 million. The indirect depreciable capital costs, land cost and fixed operating costs are calculated automatically by the H2A Model default, and many financial input values parameters are selected for the H2A Model default value. The Feedstock cost includes the electricity and thermal heat costs (based on T. Ramsden's result) of the system. Variable Operating Cost includes demineralized water based on T. Ramsden's result). The cost Calculation summary of the hydrogen product is shown below in Table 10. The total hydrogen cost is $2.88/kg. Hydrogen production cost primarily depends on the electricity and thermal heat price.

Table 10. Specific Item Cost Calculation

Cost component	Cost contribution ($/kg)	Percentage of H_2 Cost
Capital costs	$0.19	6.7%
Decommissioning costs	$0.00	0.0%
Fixed O&M	$0.24	8.3%
Feedstock costs	$2.44	84.4%
Other variable costs (including utilities)	$0.02	0.6%
Total	**$2.88**	

The calculated hydrogen production cost is around 2.74~2.88 $/kg with our L3DP electrolysis cell. The hydrogen cost is reduced by 1~6.5% compared with T. Ramsden's result. But hydrogen production cost primarily depends on the price of electricity and thermal heat, no matter our result or the result of T. Ramsden. The lower energy cost for the electrolyzer stack is another point for reducing hydrogen production.

The hydrogen cost of our L3DP electrolysis cell coupled with the nuclear reactor was calculated in this quarter. It is around 2.75-2.88 $/kg. The cost of the electrolyzer stack fabricated by our L3DP method significantly reduced the capital costs.

Milestone Base on ST-5.2 Market Transformation Plan

The market transformation activities include 1) the Formation of an Industrial Advisory Board for the project that meets annually and has a teleconference every half year; 2) Attendance at the AMRs; 3) Patent submission; 4) Consulting service with Clemson University Research Foundation for commercialization and matches inventors with investors; 5) establishment of industrial

collaboration to get a scale-up plan for manufacturing IT-PCES by L3DP technology. The PIs oversee the performance of T1-5 and the preparation of project reports and technical papers. The PIs also prepare any invention disclosures needed to protect project IP.

Milestone-5.2. Find an industrial partner interested in scaling up this technology to speed up the technology to market. Make a reasonable scale-up plan. During the last month of this project, we tried to reach some potential industrial partners. We also designed the potential laser 3D printer to showcase our technique better. We have found several private companies and national collaborators, which allows us to move the technique to the next level. Clemson is planning to apply for a patent to protect the IP further. We claim the progress of this minestrone is **95%** since our technical results improved significantly.

Figure 91 indicates that the new rapid laser 3D printing process can be at least 150 times faster than the conventional tape casting and furnace firing-based technique.

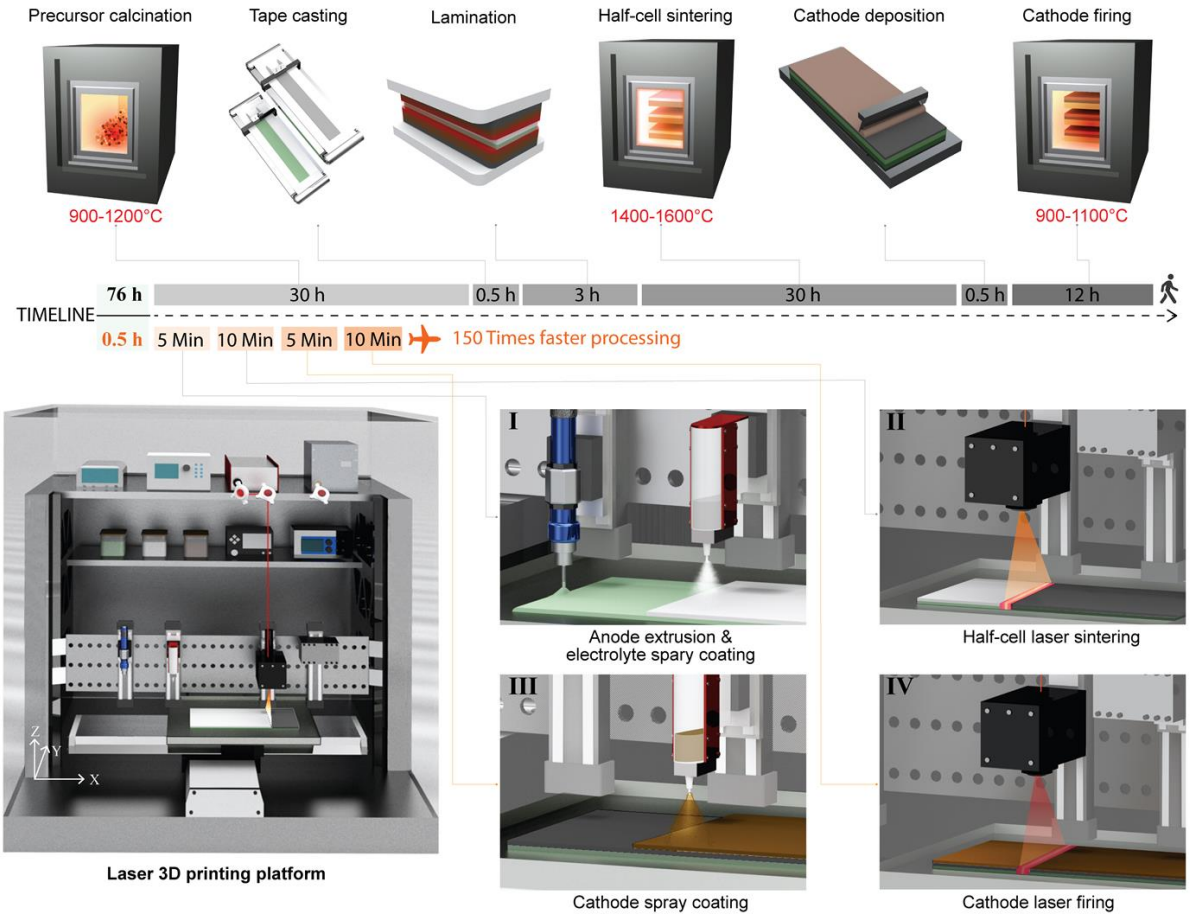

Figure 91. (a) the traditional tape-casting and furnace-firing-based technique and (b) the newly designed rapid laser 3D printing process for manufacturing ceramic-based solid oxide energy devices.

3. Project Spending by Cost Category

Project Spending by Cost Category				
Cost Category	**Approved Budget**	**Federal Share to Date**	**Cost Share to Date**	**Cumulative Total**
Personnel	$856,439	699,495.70	110,509.02	810,004.72
Fringe	$258,291	200,713.53	28,841.62	229,555.15
Travel	$16,000	7,544.34	-	7,544.34
Equipment	$103,705	-	105,551.16	105,551.16
Supplies	$42,035	74,869.05	53,730.57	128,599.62
Other Direct Costs	$107,830	101,500.50	-	101,500.50
Total Direct Costs	$1,384,300	1,084,123.12	298,632.37	1,382,755.49
Indirect Costs	$615,700	515,876.88	101,367.64	617,244.52
Total Costs	**$2,000,000**	**1,600,000.00**	**400,000.01**	**$2,000,000.01**

4. Project Spending and Estimate of Future Spending

Project Spending and Estimate of Future Spending							
Quarter	From	To	Estimated Federal Share of Outlays*	Actual Federal Share of Outlays	Estimated Recipient Share of Outlays*	Actual Recipient Share of Outlays	Cumulative
1Q19	10/1/2018	12/31/2018	10537.9	10537.9	5186.01	5186.01	15723.91
2Q19	1/1/2019	3/31/2019	101,613.02	101,613.02	34,100.28	34,100.28	135,713.30
3Q19	4/1/2019	6/30/2019	206,278.97	206,278.97	20,104.09	20,104.09	226,383.06
4Q19	7/1/2019	9/30/2019	193529.22	193529.22	11,992.98	11992.98	205522.2
1Q20	10/1/2019	12/31/2019	133668.76	133668.76	97969.83	97969.83	231638.59
2Q20	1/1/2020	3/31/2020	106916.74	106916.74	47079.81	47079.81	153996.55
3Q20	4/1/2020	6/30/2020	98408	98408	65316.47	65316.47	163724.47
4Q20	7/1/2020	9/30/2020	109939.04	109939.04	5954.64	5954.64	115893.68
1Q21	10/1/2020	12/31/2020	79795.51	79795.51	7612.28	7612.28	87407.79
2Q21	1/1/2021	3/31/2021	78468.18	78468.18	33925.27	33925.27	112393.45
3Q21	4/1/2021	6/30/2021	121519.86	121519.86	26563.29	26563.29	148083.15
4Q21	7/1/2021	9/30/2021	127072.83	127072.83	17411.57	17411.57	144484.4
1Q22	10/1/2021	12/31/2021	165497.23	165497.23	20222.71	20222.71	185719.94
2Q22	1/1/2022	3/31/2022	76084.77	76084.77	4441.07	4441.07	80525.84
3Q22	4/1/2022	4/30/2022	-9330.03	-9330.03	2119.7	2119.7	-7210.33
Totals			1600000	1600000	400000	400000	2000000

5. Patents, Publication, and Presentations

Patent

1) **J. Tong**, H. Huang, T. Zhou, K. Brinkman, H. Xiao, F. Peng, "High-performance protonic ceramic fuel cells manufactured by laser 3D printing in minutes," US patent, disclosed to Clemson University Research Foundation (**2022**).

2) H. Xiao, J. Tong, F. Peng, K.S. Brinkman, S. Mu, J. Lei, Y. Hong, H. Huang, R. Broida, "Integrated Additive Manufacturing and Laser Processing Systems and Methods for Ceramic, Glass, Silicon Carbide Application," US patent, application number 62/955,780, December 31, **2019**.

Published Papers

3) Y. Meng, H. Zheng, J. Duffy, H. Huang, K. He, J. Tong, K.S. Brinkman, "Enhanced electrolysis performance through hierarchical nanoparticle formation in the $BaCo_{0.4}Fe_{0.4}Zr_{0.1}Y_{0.1}O_{3-\delta}$ cathode materials system," *Journal of Power Sources*, **2022**, submitted, POWER-D-22-05269.

4) H. Huang, T. Zhou, M. Zou, S. Mu, J. Tang, Y. Meng, Z. Zhao, F. Peng, Hai Xiao, K.S.

Brinkman, J. Tong, "Direct laser 3D printed protonic ceramic fuel cells with outstanding area-independent performance" *under preparation*.

5) J. Tang, S. Sarkar, H. Huang, X. Geng, J. Tong, L. Vargas-Gonzalez, N. Ku, D.Li, H. Xiao, F. Peng, Machine-learning-based, online estimation of ceramic's microstructure upon the laser spot brightness during laser sintering, Engineered Science, Engineered Science, 2023, **22**, 855

https://www.espublisher.com/journals/articledetails/855/

6) Z. Zhao, M. Zou, H. Huang, X. Zhai, H. Wofford, J. Tong, "Insight of $BaCe_{0.5}Fe_{0.5}O_{3-\delta}$ twin perovskite oxide composite for solid oxide electrochemical cells," *J. Am. Ceram. Soc.*, **2023**, 106, 186-200.

https://ceramics.onlinelibrary.wiley.com/doi/full/10.1111/jace.18643

7) X. Zhai, F. Ding, Z. Zhao, A. Santomauro, F. Luo, J. Tong, "Predicting the formation of fractionally doped perovskite oxides by a function-confined machine learning method," *Communications Materials*, **2022**, **3**, 42.

https://doi.org/10.1038/s43246-022-00269-9

8) L. Han, J. Zhang, M. Zou, J. Tong, "Toward Superb Perovskite Oxide Electrocatalysts: Engineering of Coupled Nanocomposites," *Small*, **2022**, 2204784.

https://onlinelibrary.wiley.com/doi/full/10.1002/smll.202204784

9) Z. Zhao, M. Zou, H. Huang, H. Wofford, J. Tong, "Stable perovskite-fluorite dual-phase composites synthesized by one-pot solid-state reactive sintering for protonic ceramic fuel cells," *Ceramics International*, **2021**, 47, 32856-3286.

https://doi.org/10.1016/j.ceramint.2021.08.182

10) A. Ishii, H. Huang, Y. Meng, S. Mu, J. Gao, J. Lei, F. Peng, H. Xiao, J. Tong, K.S. Brinkman, "Chemically Inert Hydrocarbon-Based Slurries for Rapid Laser Sintering of Thin Proton-Conducting Ceramics," *Materials Research Bulletin*, **2021**, 143, 111446.

https://doi.org/10.1016/j.materresbull.2021.111446

11) X. Geng, J. Tang, B. Sheridan, S. Sarkar, J. Tong, H. Xiao, D. Li, R.K. Bordia, F. Peng, "Ultra-Fast Laser Fabrication of Alumina Micro-Sample Array and High-Throughput Characterization of Microstructure and Hardness," *Crystal*, **2021**, *11*(8), 890.

https://doi.org/10.3390/cryst11080890

12) J. Tang, X. Geng, D. Li, Y. Shi, J. Tong, H. Xiao, F. Peng, "Machine learning-based microstructure prediction during laser sintering of alumina," *Scientific Report*, **2021**, 11, 10724.

https://doi.org/10.1038/s41598-021-89816-x

13) X. Geng, Y. Hong, J. Lei, J. Ma, J. Chen, H. Xiao, J. Tong, R.K. Bordia, F. Peng, "Ultra-fast, selective, non-melting, laser sintering of alumina with anisotropic and size-suppressed grains," *Journal of the American Ceramic Society*, **2021**, 104, 1997-2006.

https://doi.org/10.1111/jace.17617

14) S. Mu, Z. Zhao, H. Huang, J. Lei, F. Peng, H. Xiao, K.S. Brinkman, J. Tong, "Advanced Manufacturing of Intermediate-Temperature Protonic Ceramic Electrochemical Cells." *The Electrochemical Society Interface*, 29, 67-73 (**2020**).

15) A. Ishii, S. Mu, Y. Meng, H. Huang, J. Lei, Y. Li, F. Peng, H. Xiao, J. Tong, K.S. Brinkman, "Rapid Laser Processing of Thin Sr-Doped $LaCrO_{3-\delta}$ Interconnects for Solid Oxide Fuel Cells." *Energy Technol*, 8, 2000364 (**2020**).

16) S. Mu, H. Huang, A. Ishii, Z. Zhao, M. Zou, P. Kuzbary, F. Peng, K.S. Brinkman, H. Xiao, J. Tong, "Rapid laser reactive sintering of $BaCe_{0.7}Zr_{0.1}Y_{0.1}Yb_{0.1}O_{3-\delta}$ electrolyte for protonic ceramic fuel cells." *Journal of Power Sources Advances*, 4, 100017 (**2020**).

17) J. Lei, Q. Zhang, Z. Zhao, Y. Chen, J. Gao, J. Tong, F. Peng, H. Xiao, "One-Step Fabrication of Nanocrystalline Nanonetwork SnO_2 Gas Sensors by Integrated Multilaser Processing." *Adv. Mater. Technol.*, 5, 2000281 (**2020**).

18) S. Mu, H. Huang, A. Ishii, Y. Hong, A. Santomauro, Z. Zhao, M. Zou, F. Peng, K.S. Brinkman, H. Xiao, J. Tong, "Rapid Laser Reactive Sintering for Sustainable and Clean Preparation of Protonic Ceramics." *ACS Omega*, 5, 20, 11637-11642 (**2020**).

19) S. Mu, Y. Hong, H. Huang, A. Ishii, J. Lei, Y. Song, Y. Li, K.S. Brinkman, F. Peng, H. Xiao, J. Tong, "A Novel Laser 3D Printing Method for the Advanced Manufacturing of Protonic Ceramics." *Membranes*, *10*(5), 98 (**2020).**

20) Z. Zhao, J. Cui, M. Zou, K. He, K.S. Brinkman, J. Tong, "Novel Twin-perovskite Nanocomposite of Ba–Ce–Fe–Co–O as a Promising Triple Conducting Cathode Material for Protonic Ceramic Fuel Cells." *Journal of Power Sources*, 450, 227609 (**2020**).

21) Y. Meng, J. Gao, J. Duffy, J. Tong, K.S. Brinkman, "A high performance reversible protonic ceramic electrochemical cell based on a novel Sm-doped $BaCe_{0.7}Zr_{0.1}Y_{0.2}O_3$ electrolyte." *Journal of Power Sources*, 439, 227093 (**2019**).

Delivered Presentations

22) J. Tong, "Manufacturing of Protonic Ceramic Fuel Cells by Integrated Additive Manufacturing and Laser Processing." *Invited Seminar*, West Virginia University, Morgantown, USA (September 2, **2022**).

23) J. Tong, "Advanced Manufacturing of High-Performance Protonic Ceramic Electrochemical Cells and Stacks." *the 23rd International Conference on Solid State Ionics (SSI-23)*, Boston, MA, USA (July 17-22, **2022**), **Invited Talk**.

24) M. Zou, H. Huang, J. Zhang, J. Tong, "A Novel High-Entropy Perovskite Oxide Electrolyte for Reversible Protonic Ceramic Electrochemical Cells." *the 23rd International Conference on Solid State Ionics (SSI-23)*, Boston, MA, USA (July 17-22, **2022**).

25) X. Geng, J. Tang, D. Li, Y. Shi, R. Bordia, J. Tong, H. Xiao, F. Peng, "Ultra-fast Laser Sintering of Alumina and the Microstructure Prediction Based on Machine Learning." *MS&T21: Materials Science & Technology*, Columbus, OH, USA (October 17-20, **2021**).

26) X. Geng, J. Tang, D. Li, R. Bordia, J. Tong, X. Hai, F. Peng, "Machine-learning-based Microstructure-property Prediction Enabled by High-throughput Ceramic Sample-array Preparation Using Integrated Additive/Subtractive Manufacturing." *MS&T21: Materials Science & Technology, Columbus*, OH, USA (October 17-20, **2021**).

27) M. Zou, H. Huang, S. Mu, Z. Zhao, T. Zhou, A. Santomauro, and J. Tong, "I05-1381 High-Performance Tubular Protonic Ceramic Electrochemical Cells Manufactured by Laser 3D Printing Technique." *240th ECS Digitial Meeting* (October 10-14, **2021**).

28) T. Zhou, H. Huang, M. Zou, X. Geng, F. Peng, H. Xiao, and J. Tong, "I05-1384 Picosecond Laser Cutting-Assisted Rapid Laser Reactive Sintering for the Fabrication of Crack-Free Protonic Ceramic Electrochemical Cells." *240th ECS Digitial Meeting* (October 10-14, **2021**).

29) X. Geng, J. Lei, S. Mu, H. Xiao, F. Peng, J. Tong, R. Bordia, "Fabricating alumina with

heterogeneous microstructure using integrated additive/subtractive manufacturing (IASM)." *MS&T20: Materials Science & Technology*, Virtual, (November 2-6, **2020**).

30) F. Peng, R. Bordia, X. Geng, J. Lei, H. Xiao, J. Tong, "Ultra-fast, selective laser sintering during additive manufacturing of alumina." *MS&T20: Materials Science & Technology*, Virtual, (November 2-6, **2020**).

31) J. Tong, "Laser 3D Printing of Highly Compacted Protonic Ceramic Electrochemical Cells," 5th International Workshop Prospects on Protonic Ceramic Cells, Montpellier, France (October 16-18, **2019**), Invited Talk.

32) J. Tong, S. Mu, H. Huang, Y. Meng, Y. Hong, M. Zou, J. Lei, J. Duffy, Z. Zhao, X. Geng, F. Peng, K. S. Brinkman, and H. Xiao, "Laser 3D Printing of Highly Compacted Protonic Ceramic Electrochemical Cells," 236th ECS Meeting, Atlanta, GA, USA (October 13-17, **2019**), Invited Talk.

33) H. Huang, S. Mu, Y. Meng, M. Zou, Z. Zhao, F. Peng, K. S. Brinkman, H. Xiao, and J. Tong, "Facile One Step Rapid Laser Reactive Processing of Protonic Ceramic Electrochemical Cells," 236th ECS Meeting, Atlanta, GA, USA (October 13-17, **2019**).

34) Z. Zhao and J. Tong, "Dual-Phase Nanocomposite Cathode Materials for Low-Temperature Protonic Ceramic Fuel Cells," 236th ECS Meeting, Atlanta, GA, USA (October 13-17, **2019**).

35) S. Mu, H. Huang, Z. Zhao, M. Zou, Y. Hong, J. Lei, P. Kuzbary, N. Wan, K. S. Brinkman, F. Peng, H. Xiao, and **J. Tong**, "Rapid Reactive Laser Processing of Protonic Ceramics," 236th ECS Meeting, Atlanta, GA, USA (October 13-17, **2019**).

36) M. Zou, Z. Zhao, H. Huang, S. Mu, and J. Tong, "Boosting the Oxygen Electrode Performance of Reversible Protonic Ceramic Electrochemical Cells by Interfacial Engineering," 236th ECS Meeting, Atlanta, GA, USA (October 13-17, **2019**).

37) S. Mu, Z. Zhao, H. Huang, M. Zou, J. Lei, Y. Hong, K. Brinkman, F. Peng, H. Xiao, **J. Tong**, "Rapid Laser Reactive Sintering of Ceramics for 3D Printing of Protonic Ceramic Energy Devices," MS&T2019, Portland, USA (September 29 – October 3, **2019**).

38) J. Tong, "Protonic Ceramic Electrolyzer Cells Manufactured by a Novel Laser 3D Printing Technique," MS&T2019, Portland, USA (September 29 – October 3, **2019**).

39) J. Tong, "Rapid Laser Reactive Sintering for Protonic Ceramic Electrochemical Cells," O-HyLi: Frontiers in Convergent Research in Energy and Informatics, Northwestern University, Evanston, Illinois, USA (Sep. 3-5, **2019**), Invited talk.

40) J. Tong, "Laser 3D Printing of Protonic Ceramic Electrochemical Devices," 22nd International Conference on Solid State Ionics, PyeongChang, South Korea (June 15-21, **2019**).

41) Z. Zhao, S. Mu, M. Zou, J. Tong, "Triple Conducting Perovskite Oxide Nanocomposites as Oxygen Electrodes for Intermediate-Temperature Protonic Ceramic Cells," ECS 235 meeting, Dallas, TX, USA (May 26-31, **2019**).

42) S. Mu, Y. Hong, J. Lei, Y. Song, Z. Zhao, D. Jiang, F. Peng, H. Xiao, J. Tong, "Protonic Ceramic Electrochemical Devices by Integrated 3D Printing and Laser Processing," Electronic Materials and Applications 2019 (EMA2019), Orlando, FL, USA (January 23-25, **2019**).

6. Abbreviations

3D	Three-Dimension

ASR	Area-Specific Resistance
BCFZY0.1	$BaCo_{0.4}Fe_{0.4}Zr_{0.1}Y_{0.1}O_{3-\delta}$
BCZY63	$BaCe_{0.6}Zr_{0.3}Y_{0.1}O_{3-\delta}$
BCZYSm13	$BaCe_{0.7}Zr_{0.1}Y_{0.07}Sm_{0.13}O_{3-\delta}$
BCZYYb	$BaCe_{0.7}Zr_{0.1}Y_{0.1}Yb_{0.1}O_{3-\delta}$
BZY20	$BaZr_{0.8}Y_{0.2}O_{3-\delta}$
EDTA	Ethylenediaminetetraacetic acid
EEA	Electrolyte-Electrode Assembly
GNG	Go-Not-Go
GSL	Galvo-Scanner Laser
H_2	Hydrogen
IT	Intermediate-Temperature
I-V	Current-Voltage
L3DP	Laser 3D Printing
LSCr	$La_{0.7}Sr_{0.3}CrO_{3-\delta}$
O_2	Oxygen
OCV	Open Circuit Voltage
PCES	Protonic Ceramic Electrolyzer Stack
PCFC	Protonic Ceramic Fuel Cell
RLRS	Rapid Laser Reactive Sintering
SEM	Scanning Electron Microscopy
SSRS	Solid State Reactive Sintering
T-1	Task 1
T-2	Task 2
T-3	Task 3
T-4	Task 4
T-5	Task 5
TEA	Techno-Economic Analysis
TRL	Technology Readiness Level
V	Voltage

7. References

[1] R. Scataglini, et al., A DirectManufacturing Cost Model for Solid-Oxide Fuel Cell Stacks. FUEL CELLS 17, 2017, No. 6, 825–842.

[2] R. Scataglini et al., A Total Cost of Ownership Model for Solid Oxide Fuel Cells in Combined Heat and Power and Power-Only Applications. ERNEST ORLANDO LAWRENCE BERKELEY NATIONAL LABORATORY. December 2015.

[3] Battelle Memorial Institute. MANUFACTURING COST ANALYSIS OF 1 KW AND 5 KW SOLID OXIDE FUEL CELL (SOFC) FOR AUXILIARY POWER APPLICATIONS. February 7, 2014.